



THE LATERAL DISTRIBUTION
OF CERENKOV LIGHT
FROM EXTENSIVE AIR SHOWERS

BY
BRUCE R. DAWSON, B.Sc.(Hons)

A thesis
presented for the degree of
DOCTOR OF PHILOSOPHY
at the
UNIVERSITY OF ADELAIDE
(Department of Physics)

August, 1985

To my parents.

3.3.	The Cerenkov Lateral Distribution Experiment	3.6
3.3.1.	The Array	3.6
3.3.2.	Cerenkov Pulse Height Calibration	3.9
3.3.3.	Cerenkov Data Reduction	3.15
3.4.	Analysis of Particle Data	3.16
3.5.	Conclusion	3.17

Chapter Four

The Shape of the Lateral Distribution

4.1.	Introduction	4.1
4.2.	Early Work	4.1
4.3.	The Shape of the Distribution and its Interpretation	4.4
4.4.	Current Work	4.10
4.4.1.	The Lateral Distribution and Shower Development	4.12
4.4.2.	The Shape of the Lateral Distribution	4.17

Chapter Five

Interpretation of Depth of Maximum Data

5.1.	Introduction	5.1
5.2.	Experimental DOM Distributions	5.1
5.3.	A Simulation of Selection Effects	5.4
5.4.	Interpretation of the DOM Distributions	5.14
5.5.	Conclusion	5.16

Chapter Six

Concluding Remarks

References

SUMMARY

Investigations of the cosmic ray flux around the "knee" in the all-particle energy spectrum can provide information on the origin of this steepening. Studies of air shower development in this region are especially informative, although experiments in recent years have produced some conflicting results. Some report an unusually rapid development of showers, which has been interpreted in terms of an increased proportion of heavy nuclei in the flux, compared with the directly measured low energy composition.

This thesis describes measurements of the lateral distribution of Cerenkov light associated with air showers with sea level sizes between $\sim 10^5$ and 10^7 particles. It is shown that the slope of the lateral distribution is sensitive to air shower development and that the shape is in agreement with the results of recent calculations. These calculations are used to assign depths of maximum to the showers observed.

A comprehensive simulation of the selection biases present in the experiment is used in the interpretation of the results on the depth of shower maximum. The data are shown to be consistent with a cosmic ray composition rich in iron in the energy region studied.

This thesis contains neither material which has been accepted for the award of any other degree or diploma, nor, to the best of the author's knowledge and belief, any material previously published or written by any other person, except where due reference is made.

Signed:

B.R. Dawson

Adelaide

August, 1985

ACKNOWLEDGEMENTS

I would like to thank my supervisor, Professor J.R. Prescott, for his guidance and patience throughout my candidature. I would also like to thank Dr. Roger Clay for his limitless enthusiasm and his very important input to the work.

Dr. John Patterson is thanked for his interest in the work, especially in the interpretation of the lateral distributions. Thanks are due to Dr. Ray Protheroe for valuable advice on computer simulations and other topics, and to Dr. Alan Gregory for some interesting and useful discussions. I am also grateful to Jim Kuhlmann who built up the original lateral distribution experiment. The general staff of the Physics Department have always been very helpful, and I would like to thank them, especially Neville Wild, for everything they have done.

I have made some very good friends in the Department. Thanks go to Greg Thornton, David Liebing, Peter Gerhardy, Steve Gibson, Nigel Spooner, Claire Corani, Phil Edwards, Dominic Ciampa and the other postgraduates for making the work fun as well as rewarding. Most importantly though, I want to thank Stephen Elton for always being there.

Finally, I thank Leanna Schier for typing the thesis and Jack Szeszycki for drawing the diagrams.



C H A P T E R O N E

COSMIC RAYS

1.1 Introduction.

The cosmic radiation was discovered over seventy years ago and since that time great advances have been made in the measurement and understanding of this phenomenon. It is now known that the cosmic rays we see consist predominantly of atomic nuclei with energies ranging from $\sim 10^9$ eV to at least 10^{20} eV. At the lowest energies we can observe the particles directly with relatively small area detectors aboard satellites and balloons. However at higher energies (where the flux is lower) indirect methods have been developed. In particular, studies of the cascades of particles initiated by cosmic rays in our atmosphere have been fruitful in providing information in the high energy region.

After seventy years there are still a number of areas in which our knowledge of the cosmic ray flux is deficient. For example, we don't know where cosmic rays come from and we don't know how they are accelerated to such enormous energies. Also, while we know the elemental composition at low energies where direct measurements have been performed, the high energy composition is still a matter for debate. A knowledge of the composition of the flux across the whole energy spectrum would

allow for a clearer understanding of its origin and propagation history. Other ingredients needed for a clearer understanding include a knowledge of the angular isotropy (or anisotropy) of the flux at Earth and information on the structures of the interstellar medium and the galactic magnetic field.

This survey of results from some of the important areas of cosmic ray research will begin with a discussion of the cosmic ray energy spectrum.

1.2 The Energy Spectrum.

The energy spectrum of cosmic rays measured at the Earth is shown in figure 1.1 for energies ranging from 10^{10} to 10^{20} eV. The spectrum here is of the integral type i.e. it shows the intensity of particles above a particular energy (in number $\text{m}^{-2} \text{sr}^{-1} \text{s}^{-1}$) as a function of energy. The spectrum can be approximated by a power law of the form $I(>E) \propto E^{-1.8}$ over the ten decades of energy shown. There are, however, breaks from this simple power law form. There is evidence of a "knee" in the spectrum at around 3×10^{15} eV where the function appears to steepen, and an "ankle" above 10^{19} eV where the spectrum is flatter than expected. The origins of these features are not yet clear. They will be discussed further below.

Direct measurements of the cosmic ray flux are only possible at the lower energies. Here, small satellite or balloon borne detectors can accumulate data in a realistic time. (Such detectors would not be useful at 10^{16} eV where the

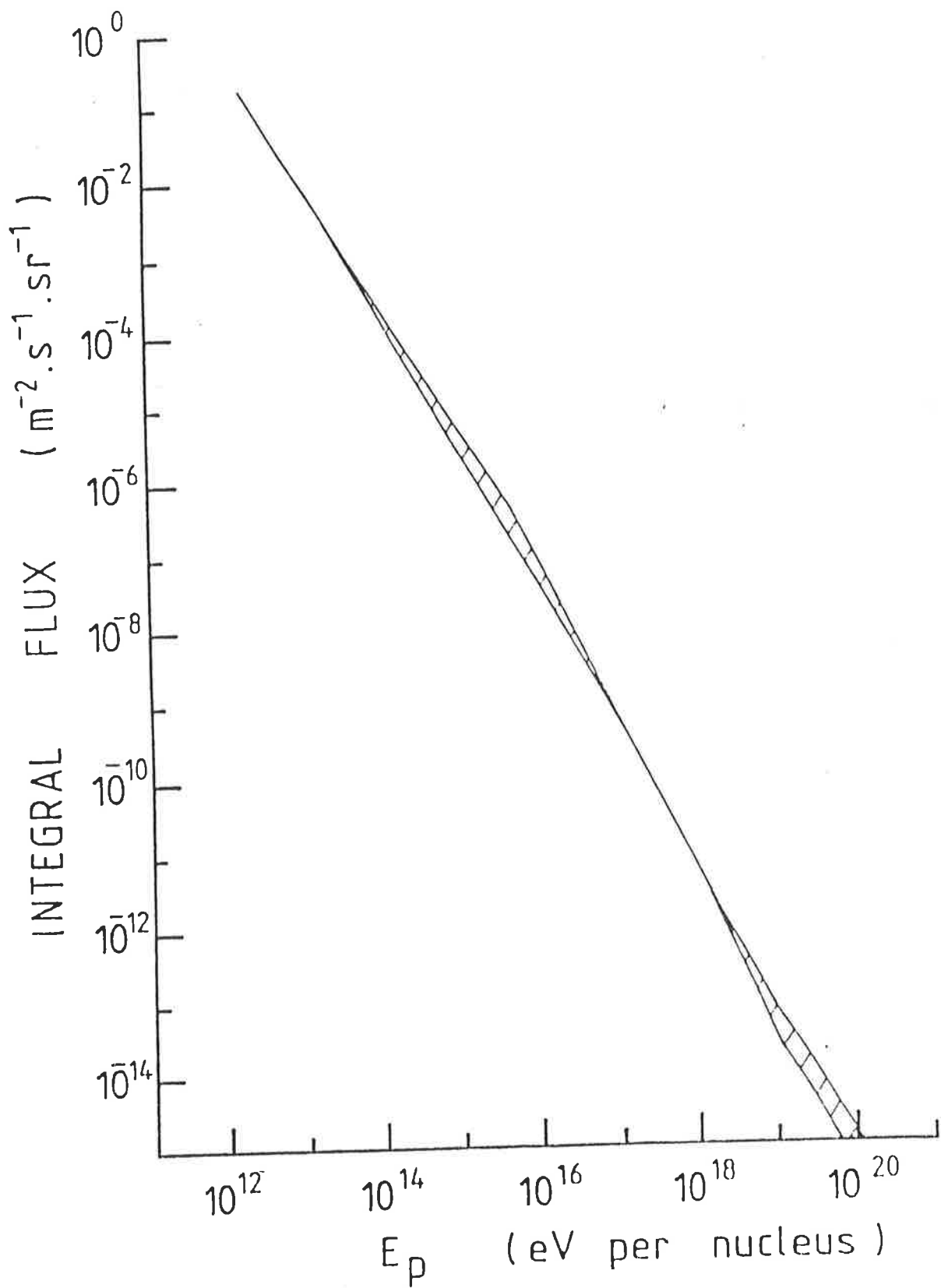


Figure 1.1: The integral flux of cosmic rays at the top of the atmosphere. The cross hatched areas represent experimental uncertainties (after Gaisser and Yodh 1980).

integral rate is 1 event per m^2 per steradian per year). These direct observations have included measurements of energy spectra of individual elemental components of the flux, from protons through to the astrophysically important iron nuclei. Some results are shown in figure 1.2 (where the spectra have been multiplied by a factor of $E^{1.5}$ to emphasize features and differences).

Above 10^{13} eV, where the flux is low, indirect methods have been used to determine the all particle energy spectrum. The all particle spectrum is the sum of the spectra of different nuclei which are indistinguishable using these methods. At the lower end of this energy range the techniques include the study at ground level of the highly penetrating muons produced by the interaction of cosmic ray primaries with atmospheric nuclei. The energy spectrum of these secondary particles can be related to the spectrum of cosmic rays. Above $\sim 10^{14}$ eV, primary particles may initiate cascades of particles which are energetic enough to reach ground level. These cascades are known as air showers and are described in more detail in Chapter Two. By building large area, ground based detectors it is possible to investigate features of the flux of the relatively rare high energy cosmic ray particles.

The knee and the ankle in the energy spectrum have been interpreted in a number of ways. It has been suggested that the knee is a consequence of a rigidity dependent leakage of cosmic rays from the Galaxy (or our local confinement region). In this, an extension of the leaky box model of

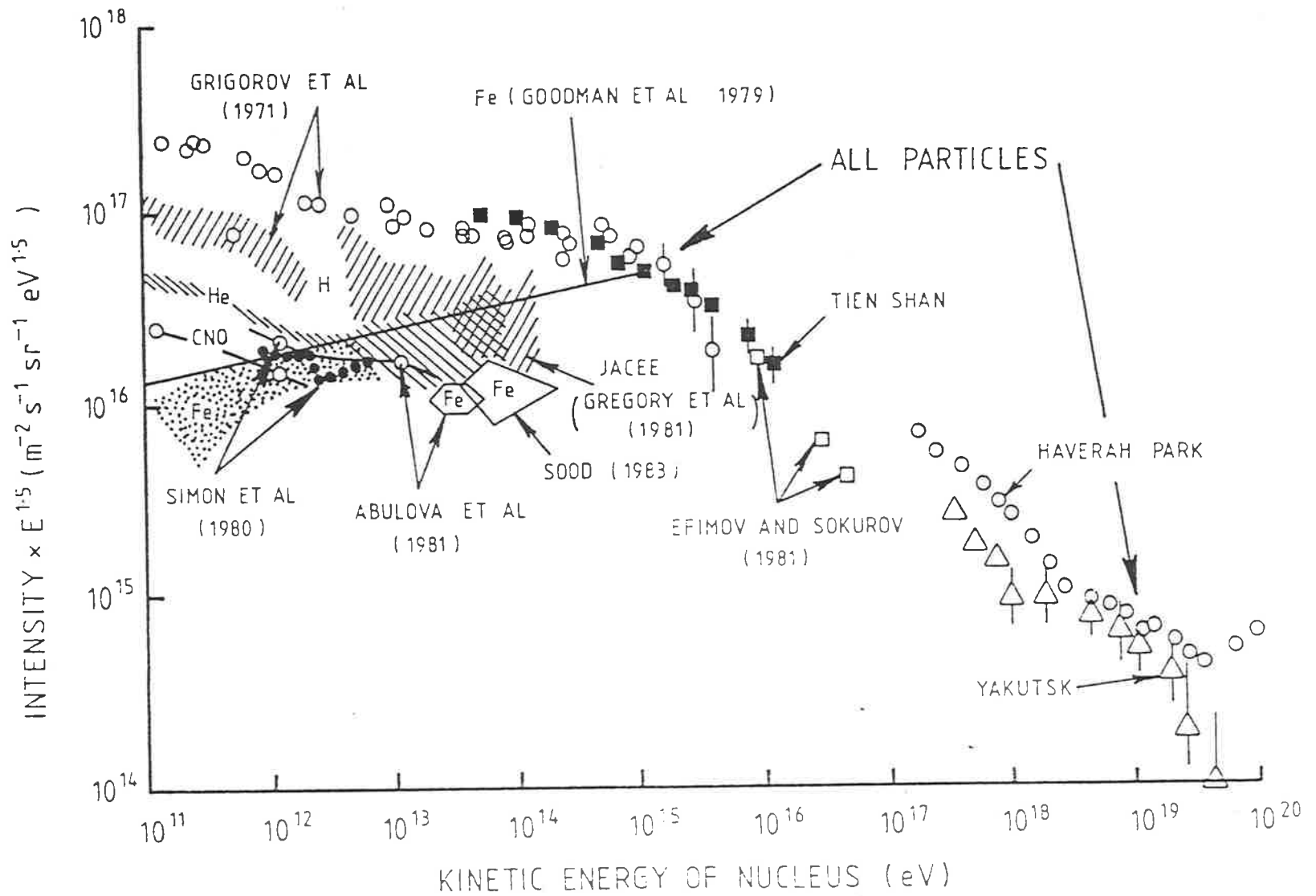


Figure 1.2: The energy spectrum of primary cosmic rays showing the major components. (essentially after Hillas 1981)

Cowsik et al (1967), a population of nuclei with the same energy per nucleus will be lost from the confinement region depending on their charge. (Rigidity can be approximated to E/Z at these energies). Thus, if the cut off in rigidity was at $10^{14}V/nuc$ the proton spectrum would begin to steepen at $10^{14}eV$, the helium spectrum at $2 \times 10^{14}eV$ and the iron spectrum at $5.6 \times 10^{15}eV$. A model such as this may well explain the structure of the knee (which at this stage is not precisely known) and has important consequences regarding the composition of the cosmic ray flux in this energy region. (see section 1.3.2)

The apparent flattening of the energy spectrum above $10^{19}eV$ (the "ankle") is a puzzling phenomenon. According to Greisen (1966) we might have expected the spectrum in this region to steepen rather than flatten. It was postulated that these high energy nuclei would lose energy through interactions with the 3K microwave background. The most important loss mechanism is expected to be pion photoproduction, with electron pair production being a less significant, but important interaction. In fact a steepening of the spectrum is observed by only one experiment, at Yakutsk (Atrashkevich et al 1983), while the data from Volcano Ranch, Haverah Park (see Linsley 1983) and Sydney (Horton et al 1983) show the flattening. The reasons for the disagreement have not been resolved. The possible absence of the Griesen cut off has placed restrictions on the extragalactic origin of the highest energy cosmic rays (see section 1.4)

1.3 The Composition of Cosmic Rays.

The study of cosmic rays has contributed in many ways to our understanding of high energy phenomena in our Galaxy. The cosmic rays constitute about one third of the energy density of the interstellar medium (ISM) and they form a relativistic gas on a galactic scale whose pressure is important in the consideration of the dynamics of galactic magnetic fields. Also, these nuclei are the only direct and measurable sample of matter from outside the solar system. The elemental and isotopic abundances in the flux convey information not only on the nucleosynthesis of matter at the sources but also on the acceleration and propagation of the particles through the interstellar medium and magnetic fields.

1.3.1 Low Energy Composition.

As mentioned earlier, the direct measurement of the cosmic ray flux is only possible at the lower energies, using satellite and balloon borne apparatus. The experiments have become so sophisticated that isotopes of the same element can now be distinguished. (This is especially so for low Z elements, where the percentage difference in masses of the isotopes is largest). Measurements of the energy spectra of individual elements shown in figure 1.2 include those of Simon et al (1980), Koch-Miramond (1981), Israel et al (1981), Dwyer and Meyer (1981) and Webber (1982). It can be seen that protons form the great bulk of the flux at these energies. An interesting feature of these data is the differences in the

spectral indices of the light and heavy nuclei at low energies. These differences may be due to propagation and solar modulation effects and may also reflect acceleration processes in the source. In any case it appears that the indices for all nuclear groups approach -1.7 at energies greater than 100 GeV/nuc (Webber 1982).

Figure 1.3 shows a compilation of the low energy ($\lesssim 10 \text{ GeV}$) abundances of species with nuclear charge number, $Z \leq 28$. A comparison of the measurements with the relative abundances of solar system matter (also shown) shows that there is a large excess in the cosmic ray flux of normally rare elements such as Li, Be, B, F and many nuclei between Si and Fe. These excesses in the cosmic ray beam are made up of so called "secondary" nuclei which are produced by the "primary" cosmic rays via spallation during their propagation through interstellar space. These nuclei tell us about the propagation conditions experienced by the cosmic rays - specifically the amount of matter traversed by the primary nuclei since their production. In fact the ratios of abundances of the secondary nuclei to their parent primary nuclei can provide information on the amount of matter traversed as a function of cosmic ray energy. Common ratios used include B/C and $Z=21-25/Fe$. (The contribution to the fluxes of B and $Z = 21-25$ by a cosmic ray source is thought to be negligible.) The ratios are found to decrease with energy (Müller 1982) above $\sim 1 \text{ GeV/nuc}$ which is interpreted as an indication of a decrease in matter path length with increasing energy. This result may imply a

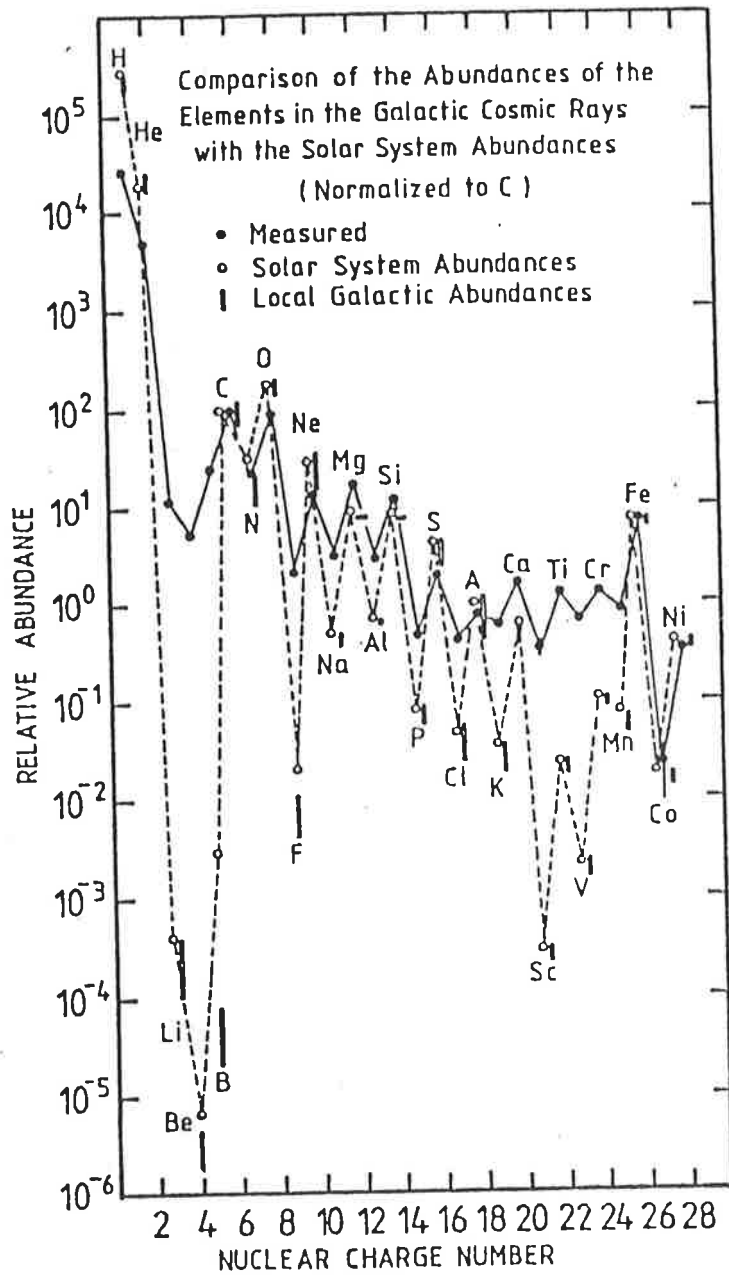


Figure 1.3: The relative abundance of low energy cosmic rays ($Z < 28$) (after Muller 1982).

rigidity dependent escape mechanism from a cosmic ray confinement region around us, or it may relate to conditions around the source. One estimate of the relationship between the matter path length (or "escape length", λ_e) and the energy per nucleon of the nucleus is given by Stephens (1981),

$$\lambda_e = 6 \text{ gcm}^{-2} (E/\text{GeV})^{-0.5} \quad \text{Eq. 1.1}$$

in the range 1 to 100 GeV/nucleon.

The "age" of the cosmic ray flux can be calculated using the abundances of unstable nuclear isotopes in the beam. Using the $^{10}\text{Be}/^9\text{Be}$ ratio (^{10}B is unstable with a half life of 1.5×10^6 years), Garcia-Munoz et al (1981) have derived an age of 14 (+13,-5) million years for cosmic rays with an energy of 100MeV/nucleon. This result together with the value of the amount of matter traversed by the cosmic rays implies a mean number density in the confinement region of 0.2 - 0.3 atoms cm^{-3} . This density is significantly lower than the values of a few atoms cm^{-3} determined for the interstellar medium in the galactic disk by astronomical techniques. Various means of confining cosmic rays in regions of lower than average density have been considered (see Cesarsky 1980).

A cosmic ray source (CRS) composition can be derived from the data when corrections for spallation effects are made. When this is done the composition agrees well with the observed solar system (SS) composition. Where differences occur, they are often strongly correlated with the first ionization

potential of the atoms (Mewaldt 1981). The mechanism for this correlation is not yet well established, although it is thought that some sort of chemical process may be acting on the products of stellar nucleosynthesis causing different elements to be accelerated with different efficiencies. It is for this reason that a study of the elemental abundances is unlikely to provide detailed information on the nucleosynthesis of matter found in cosmic rays. However, the relative abundances of isotopes of a given element will not be affected by such a chemical process. Thus studies have been undertaken of isotopes of some cosmic ray elements - those elements which are known to have a significant source component. Knowledge of the nucleosynthesis products provides constraints on cosmic ray source models. The relative isotopic abundances have been calculated ("at the source") for a number of elements, and are found to be different from those observed in the solar system (Wiedenbeck and Greiner 1981). This has been interpreted as meaning that cosmic ray sources have followed a different nucleosynthesis path to that of the Sun. For a summary of current interpretations see Wiedenbeck (1982).

1.3.2. High Energy Composition

In the preceding section a survey was presented of the data available on the low energy composition of cosmic rays and the implications for source and propagation models. The data sets were for the most part complete, and were characterised by good statistics and precision. In contrast, in the energy

region above 10^{13} eV/nucleus where the flux is lower, the available data sets are low on statistics and poor in precision. In this section some of these data and their interpretations will be presented. This is an energy regime where most, but not all, of the observations of the flux are indirect.

One of the important direct measurements has been reported by Sood (1983) who has measured the flux of Fe nuclei at $\sim 5 \times 10^{13}$ eV by observing the Cerenkov light emitted by the primary particle in the upper atmosphere. Protheroe (1984) has taken these data, together with other direct measurements of the spectra of hydrogen, helium and oxygen up to $\sim 10^{13}$ eV/nucleus and has predicted the source spectra for all four species. To do this he employed the previously mentioned leaky-box model of the Galaxy (or confinement region) (Cowsik et al 1967) where the mean escape length of a nucleus from the region depends only on its rigidity. He found that on the basis of this model the spectra at the source of all four species were consistent with power laws with index -2.0. The implications of this result for acceleration and propagation mechanisms at these and higher energies are discussed in section 1.5.

We will now turn our attention to indirect measurements of the flux. In all cases, observations are made of phenomena associated with the interaction of a cosmic ray (hereafter known as the "primary") with the atmosphere. These include observations of highly penetrating muons produced high in the

atmosphere and studies of various components of extensive air showers.

In order to interpret these indirect observations it is often necessary to resort to models of high energy particle interactions and air shower development. The colliding beam experiment at CERN has recently observed interactions with laboratory energies approaching 1.5×10^{14} eV, but this is still too low to predict with certainty the interactions of the highest energy cosmic rays. However the collider result has shown that the class of model used most widely for high energy cosmic ray calculations, based on the Feynman scaling model (Feynman 1969) is only mildly violated at these energies (Alpgard et al 1981). Nevertheless, the situation could be very different at higher energies. Our lack of knowledge of some aspects of these interactions injects a great deal of uncertainty into conclusions drawn from indirect observations. It is unfortunate that these uncertainties become most important in composition studies. (The reader is directed to Chapter Two for a discussion of extensive air showers and some aspects of the particle physics used to model them.)

An important experiment in the energy region 10^{13} - 10^{15} eV, and one which illustrates the use of models for the interpretation of data, was reported by Goodman et al (1982). In this experiment, the arrival time distribution of energetic hadrons in air shower cores was measured. All arrival times were measured with respect to the arrival times

of the shower fronts. Goodman et al had shown that the fraction of hadrons delayed by a particular time with respect to the shower front was sensitive to the composition of cosmic rays initiating the showers. In fact, given the experimental triggering conditions, the large fraction of delayed hadrons observed indicated a beam of predominantly heavy nuclei. The reasoning behind this is as follows. The delayed hadrons are thought to be slow nucleons which tend to be distributed away from the shower core. Given that showers initiated by Fe nuclei (for example) develop more quickly in the atmosphere than proton showers of the same energy, they will have a broader lateral distribution of particles at the observation level, and will be able to satisfy the experiment triggering conditions at larger core distances where the density of slow nucleons is greatest. The results of the experiment were that $0.55 \pm 0.05\%$ of the showers recorded contained hadrons with delays greater than 15ns. To interpret this result, Goodman et al attempted to reproduce the result using Monte Carlo simulations of air showers and the detector. The air shower simulations used a scaling model for particle interactions. The experimental results were reproduced using two different models of cosmic ray composition where the spectral indices etc were treated as free parameters. The models used, and the values of the parameters which reproduced the data are set out below.

Model I: A model where the p, α , CNO and medium heavy nuclei

have the same spectral index, γ_L , and the heavy nuclei a different one, γ_H . This model may fit a situation where iron, for example, is preferentially accelerated at high energies. The data were reproduced with $\gamma_L = -2.68$ and $\gamma_H = -2.39$.

Model II: Here it is assumed that all nuclear species have the same spectral index, γ , at energies below 10^{14} eV and that the spectra of different nuclear groups steepen above a critical value of rigidity, R_c . The model is an interpretation of the leaky box model, and it is assumed that the spectrum of a particular group becomes steeper by 0.5 above the critical rigidity. For this model to be consistent with the data, $\gamma = -2.55$ and $R_c = 10^{14}$ V/c.

Goodman et al point out that the experimental results cannot be explained in terms of a continuation of the low energy composition up to these energies. In fact both of the successful models discussed here predict a dominance of iron group nuclei in the flux between $10^{14} - 10^{15}$ eV. Goodman et al comment that besides explaining the delayed hadron data, Model II also naturally explains the steepening of the all particle energy spectrum at 10^{16} eV (the knee).

Another experiment sensitive to composition in this energy range ($10^{13} - 10^{16}$ eV) is the study of high energy groups of muons ("multiple muons") deep underground. These muons have energies $\gtrsim 10^{12}$ eV and are produced during the initial

interactions of cosmic rays high in the atmosphere. The multiplicity distribution of these high energy muons is sensitive to the primary composition (Elbert 1978). Results of experiments conducted by the Utah group, the Homestake Mine group and the Baksan group have been analysed with the aid of Monte Carlo simulations by Elbert et al (1981). They show that the data are consistent with a composition as presented in Model I above, implying a dominance of heavy nuclei between 10^{14} and 10^{15} eV. Mason et al (1975) have shown that the rate of muon pairs observed in their experiment can only be accounted for if the iron spectrum is flatter than other spectra up to the knee in the energy spectrum. At this energy they require the fraction of Fe nuclei in the beam to be ~80%.

Yodh et al (1984) have examined data from three other muon experiments. These experiments are concerned with lower energy muons ($E \gtrsim 5$ GeV) measured in association with air showers. Such muons are produced throughout the life of the shower via the decay of charged pions. The number of muons in these showers is expected to be sensitive to the composition of the initiating particles; showers initiated by heavy nuclei will be richer in muons than proton initiated showers. In order to study this, various parameters of the showers are measured including the density of muons at a fixed core distance, the lateral distribution of muon density and the ratio of muon number to electron number in a shower. Previous analyses of the available data had produced different predictions concerning the primary composition. For example the group

working at Tien Shan (depth 690 gcm^{-2} , muon energy $> 5 \text{ GeV}$) (e.g. Nikolsky et al 1981) and the group at the Kolar Gold fields (depth 930 gcm^{-2} , muon energy $> 220 \text{ GeV}$) (Acharya et al 1981) suggested that the composition between $10^{14} - 10^{16} \text{ eV}$ was proton dominated as at lower energies. On the other hand, the observations of the Moscow State University group (sea level, muon energy $> 10 \text{ GeV}$) (Grishna et al 1981) were found to be inconsistent with such a composition. Yodh et al (1984) looked at these three data sets and interpreted them all using a consistent model of shower development and muon production. They conclude that all the data are consistent with either a proton dominated flux or a composition rich in heavy nuclei as might occur with a rigidity dependent confinement. The problem is that the available muon data is grouped in terms of shower size rather than primary energy and the sensitivity to primary composition is almost completely lost.

Studies of the development of air showers in the atmosphere can shed light on the composition of cosmic rays above $\sim 10^{15} \text{ eV}$. Showers initiated by heavier nuclei generally develop more quickly. This can be understood in simple terms by considering the principle of superposition in the context of shower development. Consider two showers of the same energy E , one initiated by an iron nucleus and one by a proton. The superposition principle says that we may consider the iron shower as being made up of 56 subshowers each with energy $E/56$. These subshowers will grow and decay away more quickly

than the proton shower which is injected with the full energy E . The iron initiated shower, being the sum of the 56 subshowers, will therefore develop higher in the atmosphere than the proton shower. (However at their depth of maximum particle number, both showers will contain roughly the same number of particles - this number is proportional to E). It is also worth noting that due to the statistical effect of the 56 subshowers, the depth of maximum particle number for iron initiated showers of a given energy will be less subject to fluctuations compared with the depth for proton initiated showers of the same energy.

One way of studying shower development is the method of constant intensity cuts. This type of experiment has been carried out at Mt. Chacaltaya in Bolivia at an atmospheric depth of 530 g cm^{-2} . Here, the variation in shower size with zenith angle for a fixed shower intensity (no. of showers $\text{m}^{-2} \text{ sr}^{-1} \text{ s}^{-1}$) is measured. Fixing the shower intensity essentially fixes the primary energy of the showers observed and changing the zenith angle changes the depth in the atmosphere at which the shower is measured. Using these data it is possible to build up average shower development curves (i.e. shower electron size versus depth in the atmosphere) for a number of intensity values. Examples of these data from Mt. Chacaltaya (La Pointe et al 1968, Bradt et al 1965) and from Antonov (1974) are shown in figure 1.4. Gaisser et al (1978) have calculated shower profiles using the cascade theory described in their paper. These are also shown in the

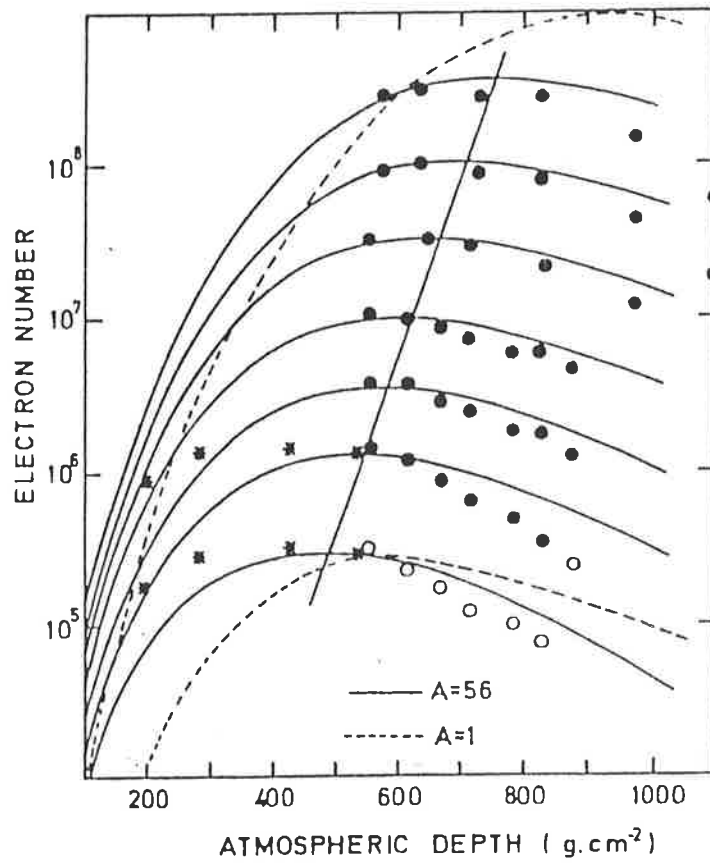


Figure 1.4: Longitudinal electron cascades from Gaiiser et al (1978). The lines represent their computed values; open circles, Bradt et al (1965); solid circles, LaPointe et al (1968); crosses, Antonov (1974).

figure. It can be seen that the rapid development exhibited by the iron initiated showers is favoured by the data. The calculations show that energies represented by the data range from 1.8×10^{15} eV to 5.5×10^{17} eV. Thus the method of constant intensity cuts favours a preponderance of iron nuclei in the region of the knee of the energy spectrum.

Another class of experiments concerned with the study of shower development is that concerned with the measurement of Cerenkov light emitted by the showers in the atmosphere. Since this light is produced by shower particles throughout the life of the shower, the flux of light measured at sea level, for example, will contain information on development. Measurements of the light include the time structure of the pulse and the lateral extent of the light pool. Observations have been made of showers with energies from below 10^{14} eV up to around 10^{18} eV. Details of experiments conducted will not be given here as they will be the subject of a section in the following chapter. However, we shall consider the results. Figure 1.5 shows a compilation of (mainly) Cerenkov results on the depth of maximum particle number versus primary energy. (Of course, the extraction of depths of maximum and primary energy from the Cerenkov measurements requires the use of model calculations). The solid line in the figure represents the average behaviour above 10^{17} eV. The apparent rapid development below this energy has been interpreted in terms of a cosmic ray composition changing from predominantly heavy at $10^{15} - 10^{16}$ eV to predominantly light above 10^{17} eV.

Figure 1.5: Explanation of symbols.

- a Antonov et al 1981; high altitude size measurements.
- A Akeno Cerenkov pulse widths; Inoue et al 1981.
- C Mt. Chacaltaya constant intensity cuts; Kakimoto et al 1983.
- G Gibson et al 1981; muon angles.
- K Yakutsk Cerenkov pulse widths; Kalmykov et al 1979.
- P Haverah Park pulse shapes; Hammond et al 1978 interpreted by Protheroe & Turver 1979.
- T Tornabene 1979; lateral distributions interpreted by Durham (Andam et al 1981).
- W Walker and Watson 1981 signal risetimes from water Cerenkov detectors.
- X and ⊗ Dugway Cerenkov lateral distributions and pulse shapes respectively; Chantler et al 1983
- Solid points Thornton 1984.
- Solid points inside circles Alimov et al 1983.
- Solid line An extrapolation of the high energy data.

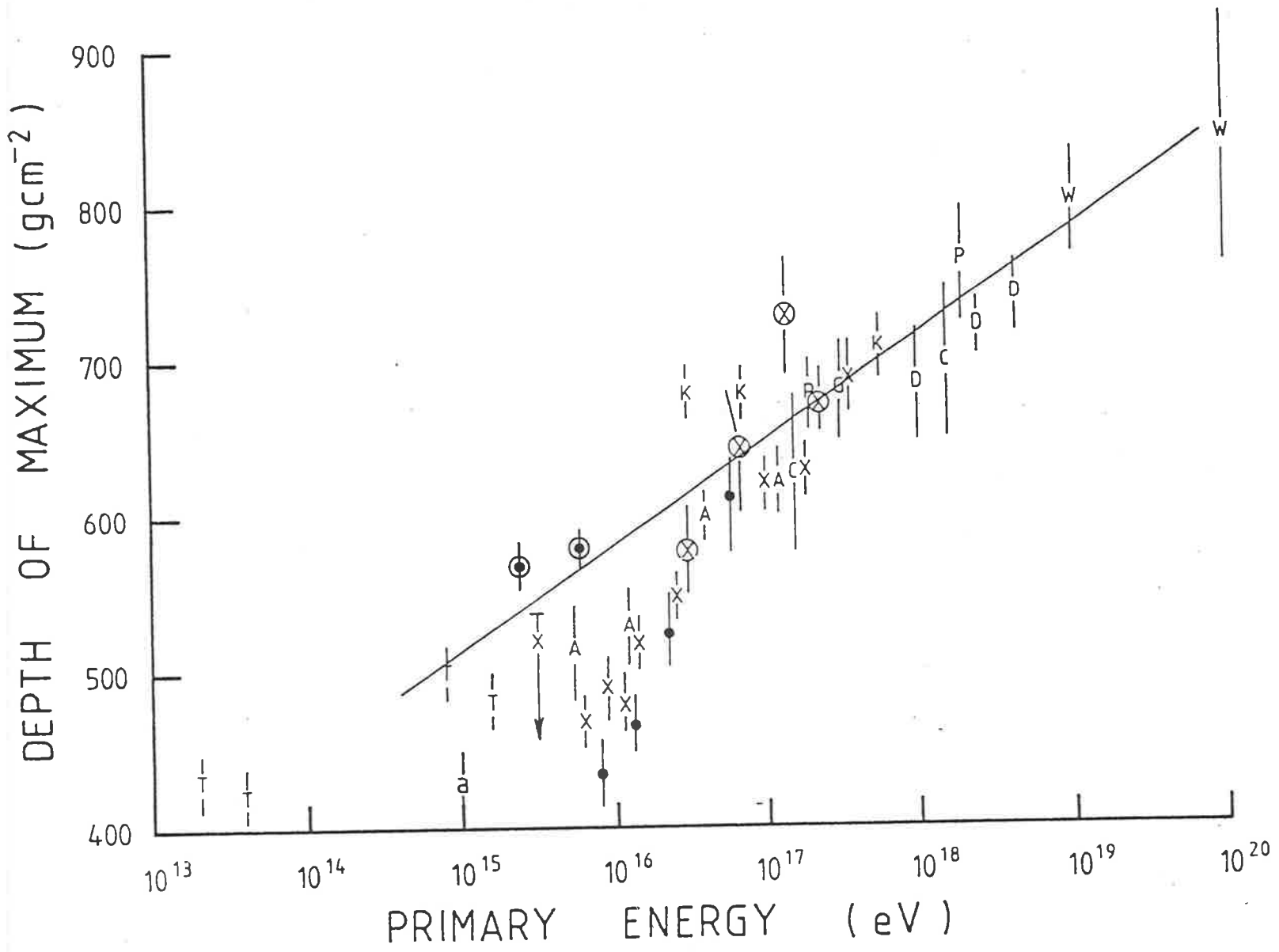


Figure 1.5: A compilation of depth of maximum data. The symbols are explained opposite.
 (after Thornton 1984)

However, the picture is not as clear cut as that. Recent preliminary data shown in the figure (Alimov et al 1983) imply a constant composition from 10^{15} eV upwards. It is also possible that the apparent rapid development of showers between 10^{15} - 10^{16} eV is due to changes in particle interactions.

Grieder (1984) claims that the depth of maximum development does not exhibit a strong primary mass signature. This signature, he says, is masked by interaction effects and large fluctuations in shower development. Instead he suggests an observable which exhibits a strong primary mass sensitivity; the high energy shower hadron spectrum. The spectrum of hadrons above 100 GeV for showers initiated by iron primaries is shown, through calculations, to cut off sharply at a much lower energy than the spectrum produced by a proton initiated shower of the same total energy. This is not surprising, given that the energy per nucleon in the Fe initiated shower is almost two orders of magnitude below that in the proton shower. Grieder has performed calculations of the high energy hadron spectra for proton and Fe showers and compared them with experimental results taken at sea level and a mountain altitude. The sea level data (e.g. Baruch et al 1979) are from showers with an average energy of $\sim 10^{15}$ eV and the data from the mountain altitude (Tien Shan; Nesterova and Dubovy 1979) have a mean energy of 4×10^{15} eV. In both cases, Grieder finds that the data are not consistent with a composition dominant with iron.

Thus it can be seen that studies of the high energy cosmic ray composition are producing contradictory results. However the support given to a change to a predominantly heavy composition around the knee of the energy spectrum is strong. This change may be consistent with a model of rigidity dependent confinement of cosmic rays in our Galaxy or local region. The apparent return to a proton dominated beam would then have to be explained in terms of acceleration processes or perhaps, an extragalactic source.

Interpretation of the experimental results in this field is hampered by uncertainties in our knowledge of particle interactions at these very high energies. It may turn out that the phenomena attributed to changes in the cosmic ray composition are, in fact, associated with drastic changes in particle physics at these energies.

1.4 Anisotropies

Cosmic ray astronomy faces a major disadvantage compared with, for example, optical astronomy. Attempts to look for "bright spots" of cosmic ray intensity in the sky are thwarted by the presence of a weak and irregular galactic magnetic field. The cosmic rays, being for most part charged particles, spiral around the magnetic field lines on a scale given by the Lamor radius,

$$r_L = 1.08 \frac{E}{ZB} \text{ parsecs} \quad \text{Eq 1.2}$$

where Z is the charge of the particle (in units of e), E is its energy (in units of $10^{15}eV$) and B is the magnetic field strength (in microgauss).

It is known that the structure of the galactic magnetic field is very complex. It is studied by observing phenomena such as the Faraday rotation of the plane of polarization of linearly polarized radiation in the Galaxy. The polarization of radio synchrotron emission is also observed since the plane of polarization of this radiation is perpendicular to the magnetic field direction at its source. Starlight can also be polarized through absorption by non-spherical dust grains oriented in the local field. For a review of techniques and results in this area see Heiles (1976). Reliable measurements of the galactic magnetic field are limited to a cylindrical region of the galactic plane within 2kpc of the sun. Outside this region the extent and magnitude of the field is very uncertain. However within the local region, there is a large scale longitudinal field (i.e. directed toward one direction below the galactic plane and toward the opposite direction above the plane) with a strength of $2-3\mu G$ directed towards the galactic longitude $l \sim 90^\circ$ (Gardner et al 1969). Superimposed on the regular field are large scale fluctuating components which have scales of several hundred parsecs and strengths approximately equal to the regular field. These seem to be associated with magnetic bubbles formed by the trapping of fieldlines in matter swept up by expanding shock waves initiated by supernovae. Smaller scale fluctuations also

exist.

The structure of the field outside the disc of the galaxy (in the "halo") is unclear. The halo consists of hot, low density gas and extends several kiloparsecs beyond the disc. Hillas (1982) has considered a model where field lines are trapped in matter expanding away from the disc and predicts a field strength of a few tenths of a microgauss. However, interpretations of synchrotron polarization put the field closer to $1\mu\text{G}$.

Even given this incomplete picture of the galactic magnetic field, it is clear that only the highest energy cosmic rays will move in trajectories approaching straight lines. For example a 10^{14}eV proton has a radius of gyration of only 0.04pc in a $3\mu\text{G}$ field. Thus the arrival directions of the cosmic rays are not expected to contain explicit information on the source directions, except at the highest energies. It has been found that cosmic rays at most energies are very isotropic. The degree of anisotropy is defined by the amplitude,

$$\delta = \frac{I_{\text{max}} - I_{\text{min}}}{I_{\text{max}} + I_{\text{min}}} \quad \text{Eq. 1.3}$$

where I_{max} and I_{min} are the maximum and minimum intensities of cosmic rays across the sky. The direction (or phase) of the anisotropy is generally quoted in terms of Right Ascension. (Results are generally averaged over the declination band visible to the detector). A summary of northern hemisphere

data (showing both amplitude and phase) is shown in figure 1.6 (from Watson 1981). The lowest energy data come from experiments conducted underground where muons from interactions of the primary cosmic rays are detected. Around $10^{13} - 10^{14}$ eV the data is derived from air shower counting rate experiments conducted at mountain altitudes. The remaining data result from studies of larger air showers near sea level.

The first notable feature of the figure is the constancy of the anisotropy between 5×10^{11} eV and 10^{14} eV, in terms of both amplitude and phase. This has been interpreted by Kiraly and Kota (1979) as implying a nearly constant confinement time for the cosmic rays in this energy range. This must mean that a more efficient confinement mechanism exists here compared with lower energies where the confinement time was energy dependent. (This result was expressed in terms of path length in section 1.3) Above 10^{14} eV, the anisotropy changes in both phase and amplitude. The amplitude dependence goes roughly as $E^{0.5}$. This increase is not unexpected given the presence of medium scale (\sim few parsecs) irregularities in the interstellar medium which are associated with magnetic field irregularities. The fact that this change in anisotropy occurs at energies near the knee of the energy spectrum has not escaped notice. Peters (1961) suggested that the coincidence may reflect the inability of the Galaxy to retain cosmic ray protons with energies above 10^{15} eV. A result of this hypothesis is that heavier nuclei would begin to dominate the cosmic ray flux above 10^{15} eV. Hillas (1979, 1982) has reviewed

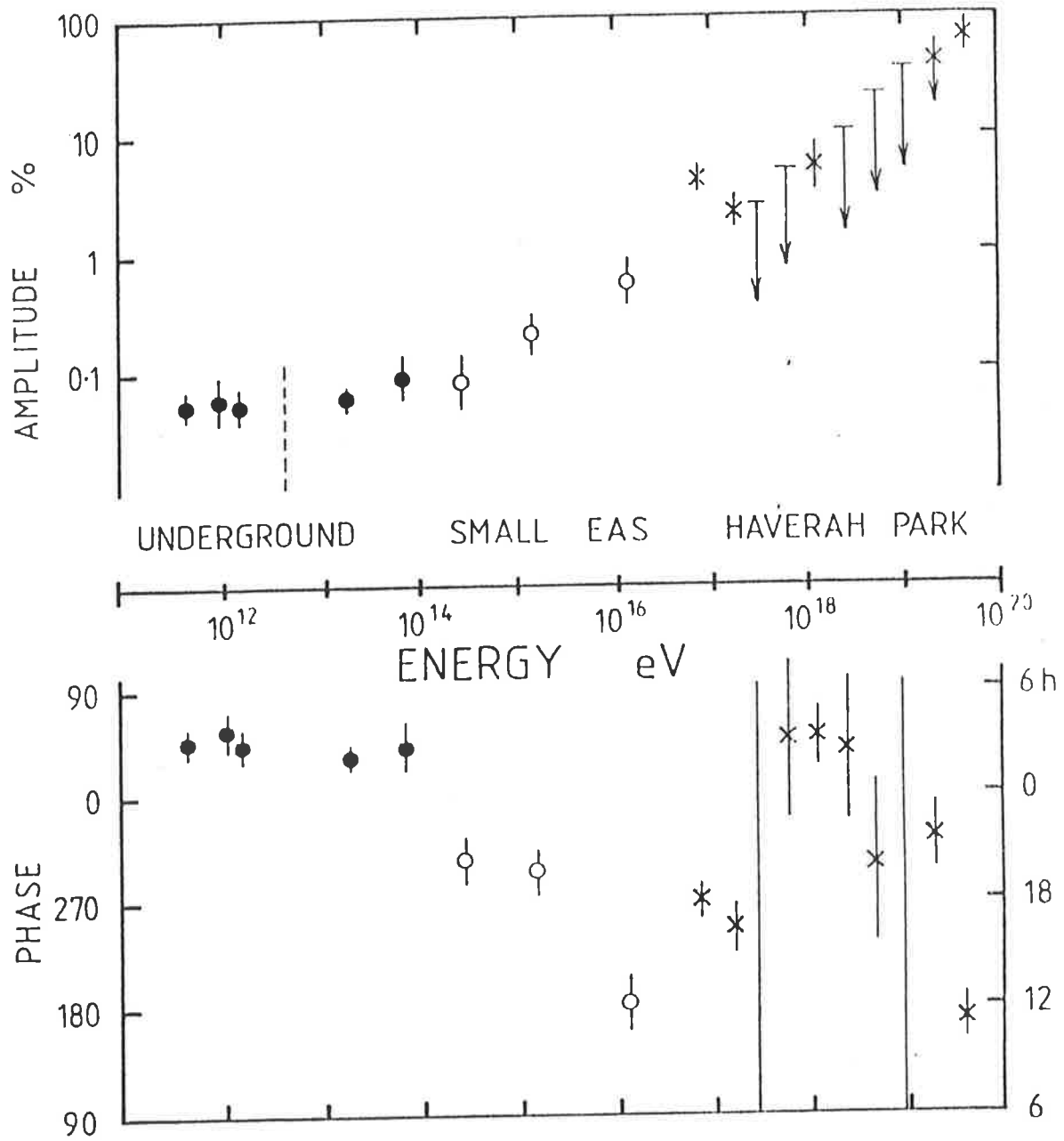


Figure 1.6: The amplitude and phase of the observed anisotropy of cosmic rays (after Watson 1981).

the composition data (which on the whole shows an onset of "heavy" dominance below 10^{15} eV, section 1.3.2) and rules out the galaxy leakage model. Whatever the case, the data have been interpreted by Lloyd-Evans and Watson (1982) in favour of a galactic origin for cosmic rays with energies up to $\sim 2 \times 10^{17}$ eV.

Above this energy, the interpretation of the results is hampered in two areas. Certainly at these energies the Larmor radii are sufficiently large so that the particle paths are not significantly altered by large scale galactic magnetic field irregularities. This means that arrival direction studies are more meaningful, but interpretation in terms of galactic or extragalactic origin depends on the models of halo magnetic field and cosmic ray composition used. Astley et al (1981) working at Haverah Park report an excess of cosmic rays from southern galactic latitudes in the energy range $5 \times 10^{17} - 5 \times 10^{18}$ eV. The origin of these particles is unclear - if the magnetic field in the galactic halo is as strong as the synchrotron emission suggests ($> 1 \mu$ G) then Hillas (1982) has shown that the particles could have a galactic origin. If, however, the field is weak then the cosmic rays could only be galactic if the beam was composed entirely of iron nuclei (Astley et al 1981).

Above 10^{19} eV the statistics are very poor. However it appears that in this energy range more cosmic rays arrive from northerly galactic latitudes (Cunningham et al 1980). It is thought that these particles are extragalactic, originating

from somewhere in the Virgo supercluster. (Their source must lie within ~ 200 Mpc, the attenuation length for the interaction between protons and the 3K microwave background - Greisen 1966).

A major discovery has been made recently which has immense implications for cosmic ray source studies - the discovery of ultra high energy (UHE) gamma ray sources. The gamma rays observed have energies in excess of 10^{15} eV and produce air showers in the atmosphere in a way similar to cosmic rays. Of course their advantage over cosmic rays is that they travel in straight lines from their source. The Kiel group (Samorski and Stamm 1983) have reported an excess of showers arriving from the direction of Cygnus X-3. These excess events were modulated with the 4.8 hour orbital period of the Cyg X-3 system, and so were interpreted as ultra-high energy gamma rays. This result was confirmed by the Havarah Park group (Lloyd-Evans et al 1983). The first southern hemisphere source, Vela X-1, was identified by the Adelaide group (Protheroe et al 1984) using the Buckland Park array. This group has also recently reported the first extragalactic source of these photons; LMC X-4 in the Large Magellenic Cloud (Protheroe and Clay 1985). All three sources are neutron star binary X-ray systems. These observations have important consequences for cosmic rays - the UHE gamma rays are probably produced in interactions of UHE protons or nuclei (accelerated in the vicinity of the compact object) with the atmosphere of the companion star (e.g. Eichler and Vestrand 1984).

Preliminary studies of the differential energy spectrum of these gamma rays shows that it approximates E^{-2} which would imply a E^{-2} particle spectrum. This agrees with the spectrum which has been inferred for sources from measurements of the particle spectra at Earth (Ormes and Protheroe 1983, Protheroe 1984).

Considerable activity is now in progress in this new area of astronomy. The new Buckland Park array (Prescott et al 1983) will be especially suited to UHE gamma ray work with its improved directional accuracy. On the theoretical side, it will be interesting to see the production mechanisms proposed. There is a strong possibility that neutron star binary systems produce a large proportion of the high energy cosmic rays we see. This will be discussed further in the following section.

1.5 Acceleration and Propagation

Realistic models of cosmic ray acceleration and propagation need to make predictions in accord with the established experimental results. These include the results on the energy spectra (of individual species at low energies and the all-particle spectrum) and the low energy composition (including details of the elemental and isotopic composition and the proportion of secondary particles in the flux). It will be seen that current models are quite successful in explaining these features, and make interesting predictions about controversial areas such as the high energy cosmic ray

composition.

One of the earliest models of cosmic ray acceleration was put forward by Fermi (1949). Here, cosmic ray particles gain energy gradually through collisions with randomly moving gas clouds in interstellar space. (This mechanism has become known as second order Fermi acceleration). Another early model involved cosmic ray nuclei being accelerated in supernovae explosions. It was claimed that this mechanism could account for the entire observed spectrum of cosmic rays. (Colgate and Johnson 1960)

Recently, a group of models has emerged which borrows elements from each of these early mechanisms. This is the field of acceleration by diffusive shock waves, a field which has become very popular in recent years. (For a review, see Axford 1981). The main reason for its popularity is that this mechanism successfully predicts the slope of the galactic cosmic ray spectrum inferred from measurements at Earth ($\sim E^{-2}$) (Blandford and Ostriker 1980). In a modification of the Fermi mechanism, particles are accelerated by continually being scattered across a shock front. The mechanism is known as first order Fermi acceleration, the scattering centres in this case having a non-random bulk motion. The shock wave may be due to a supernova explosion or it may be due to a strong stellar wind. It has been shown that cosmic ray nuclei require a minimum amount of energy before shock acceleration is feasible. Cowsik (1980) has predicted the value to be ~ 10 MeV. It seems possible that supernova explosions and

second order Fermi acceleration can provide particles with this minimum energy.

As mentioned in section 1.3.1, it has been observed that the ratio of the number of secondary to primary particles (the S/P ratio) in the cosmic ray flux decreases with energy (Müller 1982). This places a restriction on the shock front acceleration models as it implies that there is no significant reacceleration of the secondaries. In fact this restricts the number of times a shock wave can pass through a region during the cosmic ray lifetime ($\sim 2 \times 10^7$ yrs) to once or twice. However, given that a supernova occurs in our galaxy every 25-30 years, Axford (1980) has calculated that supernova shock waves pass through every point in the galaxy ten times in 2×10^7 years. In an attempt to reduce this exposure, a number of models have been proposed. Streitmatter et al (1983) have included so called "superbubbles" in their model. These large shells of neutral hydrogen have been discovered recently (Heiles 1979) and have been interpreted as being made up of matter swept up by the stellar winds and supernovae of OB associations. These structures have scales of hundreds of parsecs and contain hot, low density gas. In their model, Streitmatter et al envisage acceleration taking place only at the boundary of the bubble, and only when a supernova shock impinges on it. This model successfully predicts the S/P ratio. Another consequence of the superbubble model is that the bubble would cease to confine cosmic rays if they became too energetic. If the solar system was inside such a

superbubble (as Streitmatter et al have suggested) then this fact may help to explain the features of the anisotropy and energy spectrum at these energies.

It has been pointed out that given the constraints placed on shock acceleration by the S/P ratio, there is a maximum possible particle energy for acceleration using this mechanism. The most recent estimate of E_{\max} has been made by Lagage and Cesarsky (1983). They find that in the most optimistic case, nuclei cannot be accelerated to energies greater than 10^{14} eV/nucleon. However a more realistic model puts an upper limit at 10^{13} eV/nucleon.

It seems that there may need to be another mechanism for cosmic ray acceleration above $\sim 10^{13}$ eV per nucleon. This possibility was arrived at from another direction by Protheroe (1984). After determining the source spectra for H, He, O and Fe using direct measurements up to $\sim 10^{13}$ eV/nucleus (see section 1.3.2), the elemental abundances expected at air shower energies were calculated. It was assumed that the structure in the observed energy spectrum is due solely to rigidity dependent acceleration or propagation effects. The results of the calculation were inconsistent with the composition derived from air shower measurements (section 1.3.2) and it was concluded that either the processes involved were not solely rigidity dependent, or that some other type of source of cosmic rays was responsible for the particles at air shower energies.

The recent discovery of UHE gamma rays from neutron star binary systems (section 1.4) has important implications for

sources of high energy cosmic rays. It is thought likely that these photons are products of high energy particles accelerated by the compact object. It has been calculated that the particles need to be protons or nuclei with energies in excess of 10^{16} eV (Eichler and Vestrand 1984). It is believed that the particles travel from the compact object and interact with the tenuous outer layers of the companion star, producing gamma rays through the decay of neutral pions. This hypothesis is supported by the observations of Cygnus X-3 where gamma rays are seen briefly at two times during the 4.8 hour rotation period (Samorski and Stamm 1983) i.e., we are seeing the compact object through the atmosphere of the companion star just before and just after total eclipse.

Wdowczyk and Wolfendale (1983a) have calculated that about 30 Cygnus X-3s could supply enough power to maintain the cosmic rays in our Galaxy (Vela X-1 has a power of only 10^{-2} of the power of Cygnus X-3 - Protheroe et al 1984). Hillas (1984) has proposed a model of gamma ray production in Cyg X-3 involving the production of monoenergetic 10^{17} eV protons at the pulsar. The interactions of these protons to produce electron-photon cascades in the atmosphere of the companion can account for the observed E^{-2} photon energy spectrum above a few GeV. Hillas points out that the particle beam does not need to be strictly monoenergetic; only that the energy carried by protons with energies above 5×10^{16} eV is greater than the energy carried by protons in the four decades of energy below this. Also, the particles need not be protons. Nuclei with the same energy per

nucleon are also consistent with the model. Most of the nuclei will escape from the system providing an energy input of 10^{39} erg s^{-1} above 10^{16} eV/nucleon. Hillas has calculated that this is enough power to maintain the galactic cosmic rays above 10^{16} eV against leakage. This means that Cygnus X-3 may be the only major source in the Galaxy (at this time) of high energy cosmic rays. If the beam is indeed monoenergetic, the observed energy spectrum of cosmic rays could be explained in terms of an evolution with time of the beam energy of the compact object (Gunn and Ostriker 1969).

Whatever the mechanism, it appears likely that these binary objects provide the galactic cosmic rays above the shock front acceleration cut off energy. However the sources of the highest energy cosmic rays are still unknown. From arguments presented in section 1.4, it seems likely that they are extragalactic. Hillas (1982) has suggested two possible classes of accelerators; small very dense objects with intense magnetic fields (pulsars, black holes, active galactic nuclei) and large (\sim megaparsec) objects with weak magnetic fields. An example of the latter class would be shockfront acceleration in the turbulent wake of galaxies. As yet no plausible mechanism has been discovered.

C H A P T E R T W O

EXTENSIVE AIR SHOWERS

2.1 Introduction

It is clear that the direct observation of cosmic ray primary particles is limited to energies below $\sim 10^{12}$ eV where the intensity is large enough to make small detectors useful. Above this energy, indirect methods are used. Fortunately, the high energy cosmic rays produce cascades of secondary particles in the atmosphere known as extensive air showers (EAS). These showers spread laterally as they develop in the atmosphere, and can be detected at ground level with an array of detectors. Arrays usually consist of a number of small detectors spread over a large area, making the study of the highest energy cosmic rays feasible.

In this chapter we shall review our knowledge of the major components of extensive air showers. We shall then consider one of the methods used to study air shower development - the observation of atmospheric Cerenkov light from EAS.

2.2 The Components of Extensive Air Showers.

An EAS is initiated when a primary cosmic ray nucleus collides with a nucleus within an atmospheric molecule. The depth in the atmosphere of this first interaction depends on the nature of the primary particle and its energy; for a 10^{16} eV proton the mean free path in air is $\sim 50 \text{gcm}^{-2}$ (Ellsworth et al 1982) while for an iron nucleus the figure is only

$\sim 13 \text{ g cm}^{-2}$ (Westfall et al 1979). The collision results in a number of secondary mesons (mainly pions, with equal numbers of π^+ , π^- , π^0) and fragment nucleons. A schematic diagram of an EAS is shown in figure 2.1. The neutral pions produced in the collision decay rapidly into two photons ($T_{1/2} = 7.6 \times 10^{-17} \text{ s}$) initiating the largest component of an air shower, the electromagnetic cascade. The charged pions may decay into muons of the same charge and a muon neutrino ($T_{1/2} = 2.6 \times 10^{-8} \text{ s}$) contributing to the muon component of the EAS. The remaining charged pions and the fragment nucleons interact to sustain the hadronic core of the cascade. This core continues to feed the electromagnetic and muon components of the shower as it passes down through the atmosphere. In the following sections we shall discuss the features of the three major components in some detail.

2.2.1 The Hadron Component

This component, being a result of interactions of the primary cosmic ray and its descendents, is the source of energy for the entire cascade. It is often known as the core of the shower, since the lateral spread of the component (determined by the transverse momentum acquired by the hadrons in interactions) is small compared with that of the electromagnetic cascade. The growth and subsequent decay of air showers depend critically on a number of interaction parameters of nucleons and mesons. These include the nucleon and pion interaction lengths in air (λ_N and λ_π respectively), the fraction of energy expended by a primary or "leading" particle in a collision (the inelasticity, $K < 1$) and the

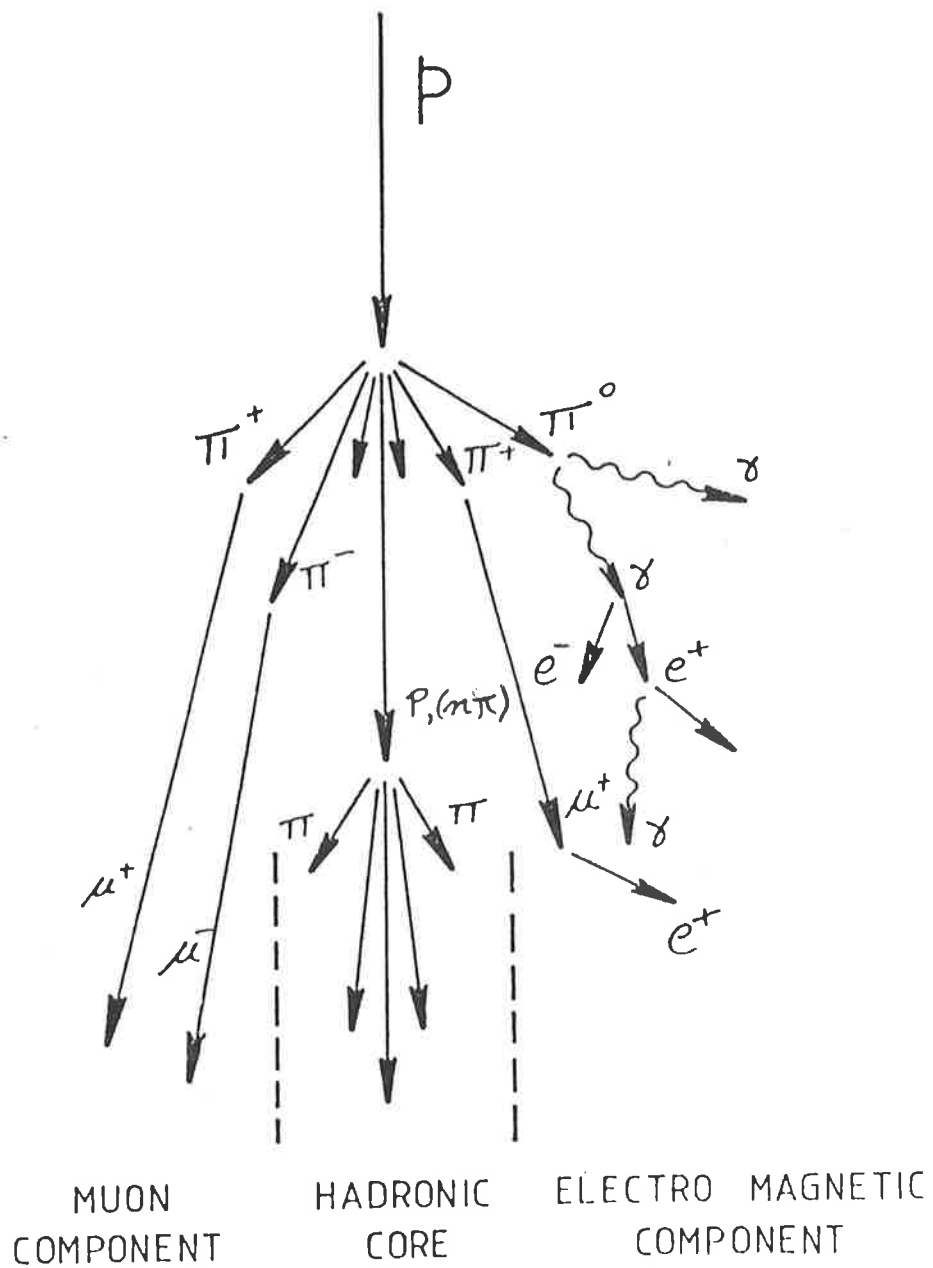


Figure 2.1: A schematic diagram of an EAS. The neutrinos accompanying the pion and muon decays have been omitted for clarity (after Thornton 1984).

number of secondary mesons (mainly pions) produced in a nucleon-nucleon collision (the multiplicity, g). Controlled measurements of these parameters have been confined to accelerator experiments. The highest energy accelerator collisions so far produced have been achieved using the CERN SPS $p-\bar{p}$ colliding beam experiment. In the equivalent laboratory reference frame, the energy of these collisions is $\sim 1.5 \times 10^{14}$ eV (e.g. Kalmus 1982). In order to interpret air shower processes above this energy it is necessary to resort to models of particle interactions.

Accelerator studies have shown that the secondary multiplicity, g , increases with the energy of the projectile. The way in which g changes with energy above the energies reached using accelerators is model dependent. There is however an upper limit imposed on the rate of increase of g with E . This kinematic limit would be reached if the entire centre of mass energy of the system was converted to pion mass in a collision. Since the centre of mass energy is $\propto E^{1/2}$ (E is the laboratory frame energy of the projectile) we find that the limit on the rate of change of multiplicity with energy is expressed by

$$g \propto E^{1/2} \quad \text{Eq. 2.1}$$

In accelerator collisions it is observed that the multiplicity changes more slowly than this. This means that most of the incident energy emerges from the collisions as the kinetic energy of the outgoing particles. In the centre of mass frame, the collision results in two jets of particles

travelling with only small deviations from the directions of the incoming particles; whereas the longitudinal components of the secondary momenta, p_L , take a wide range of values, the transverse momenta, p_T , are generally quite small. Consider the following interaction,



where A and B collide to produce a particle, C, which is observed, and a number of other particles, represented by X, which are not observed because of practical limitations. Since not all of the particles can be observed, this is known as an "inclusive" observation. The invariant inclusive cross section is defined

$$E_c \frac{d^3\sigma}{d^3p_c^3} \qquad \text{Eq. 2.3}$$

where $d^3\sigma/d^3p_c^3$ is the differential cross section (i.e. the probability per unit incident flux) for detecting the particle C within the phase space volume $d^3p_c^3$. The energy E_c is included to make the quantity invariant under Lorentz transformation. The momentum p_c has components p_L and p_T . Consider the dimensionless quantity

$$x = \frac{p_L}{p} \qquad \text{Eq. 2.4}$$

which measures, in the centre of mass frame, the fraction of the beam's momentum (p) which is contained in the longitudinal momentum component (p_L) of a detected particle. Clearly

$0 < x < 1$. It is found that if the invariant inclusive cross section for a collision is plotted as a function of x , it is observed that a large number of slow particles is produced (cross section high, x near 0), but that the cross section decreases rapidly to zero as $x \rightarrow 1$. The important point is that this distribution is found to be essentially independent of energy, an effect which is known as Feynman scaling (Feynman 1969). This is the basis of a successful group of models which use the variable x (and other similar variables) to "scale up" the results of accelerator experiments to air shower energies. An important result of the original Feynman scaling model was that the secondary multiplicity varies as

$$g \propto \ln E \qquad \text{Eq. 2.5}$$

where E is the laboratory frame energy of the projectile. It is worth pointing out here that another class of models, the thermodynamic models (Fermi 1951, Landau 1953) predict $g \propto E^{1/4}$.

The original scaling model was conceived at a time when it was believed that the total proton - proton cross section was becoming constant at high energies. However, this cross section has now been observed to increase with energy, in cosmic ray experiments (Yodh et al 1972, Baltrusaitis et al 1984) and in accelerator experiments (Amaldi et al 1977). It has also been found that the average transverse momentum of secondary particles is increasing slowly at accelerator energies (e.g. McCubbin 1981). Current scaling models therefore contain elements of the original model together with

components expressing increases in cross sections and transverse momenta. However, the investigation of the validity of interaction models at air shower energies is hampered by our lack of knowledge of the cosmic ray composition. This problem will be discussed more fully in Chapter 6.

2.2.2 The muon component.

Charged pions produced in particle collisions in the hadronic cascade may either suffer further collisions or may decay into a muon and neutrino. The probability of decay depends on the energy of the pion (as this determines the relativistic half life for the decay process) and the local air density.

For a production height of 5km, pions of energy less than 30 GeV are more likely to decay than interact (e.g. Protheroe 1977). At greater heights, where the density is lower, this threshold increases.

The muons produced in these decays have a relatively long half life ($\tau \sim 2.2 \times 10^{-6}$ s), and consequently the high energy particles (with Lorentz factors $\gamma > 20$) often survive down to sea level. The low energy muons often decay to an electron and two neutrinos and thereby contribute a small amount to the electromagnetic cascade. Since the high energy muons are generally produced early in the life of the shower, their lateral spread at sea level (determined by the height of production and the transverse momentum imparted to the parent pions) is comparable with that of the electromagnetic component.

The high energy muons ($E > 100$ GeV) are of particular

interest because they are produced early in the cascade and carry information about the nature of the cosmic ray nucleus and the interaction physics (see for example Yodh et al 1982 and Chapter One).

2.2.3 The Electromagnetic Component.

This component of air showers is by far the largest in terms of particle numbers. The component grows during the passage of the shower through the atmosphere, fed with energy from the hadronic cascade. Eventually however, the energy lost by the cascade to the atmosphere becomes greater than the energy supplied by the core. At this stage, the electromagnetic cascade begins to decay. In this section we shall discuss some of the features of electromagnetic cascades and in the following section it will be seen how studies of the development of the cascade can shed light on the questions of composition and particle interactions.

The electromagnetic component of a shower is initiated with the decay of a π^0 meson. Because of the very short half life of this particle, it will decay before having an opportunity to interact. The two high-energy gamma rays produced in the decay can transfer energy to electrons in one of three ways. These are through the processes of photoelectric absorption by a bound electron, Compton scattering off an essentially free electron, and the production of an electron-positron pair. For gamma rays of this energy, the first of these processes is relatively unimportant. Figure 2.2 shows the probabilities for the remaining processes as a function of gamma ray energy. It can be seen that Compton

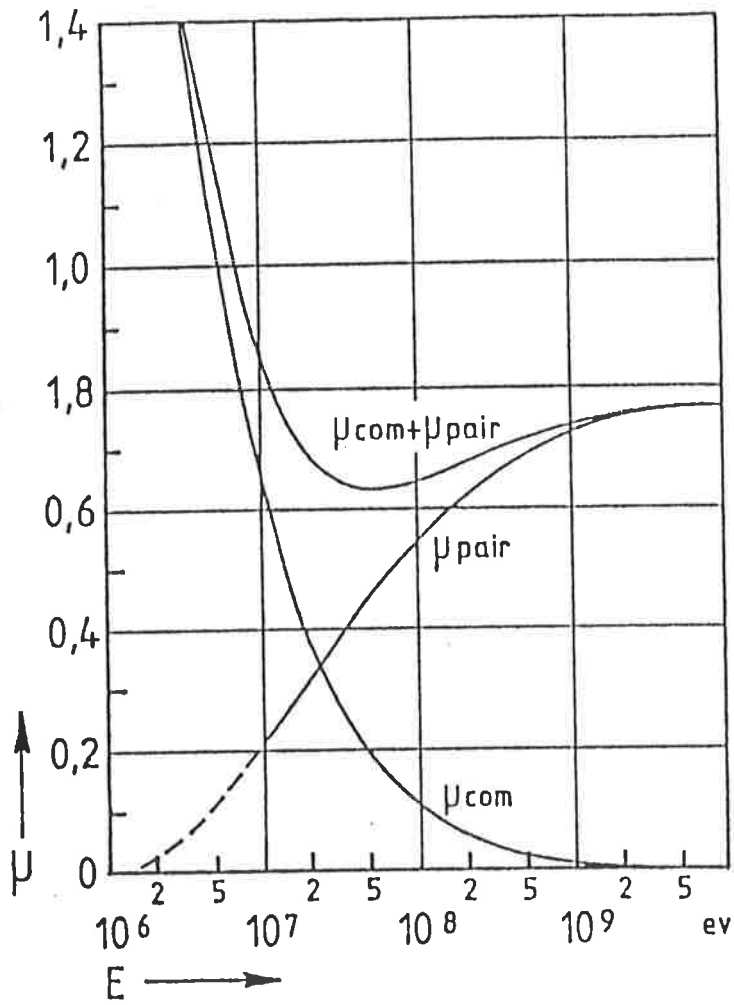


Figure 2.2: The total probability per radiation length for air for Compton scattering, for pair production and for either. (After Rossi and Greisen 1941).

scattering is the most likely interaction mechanism for photons with energy $\lesssim 20\text{MeV}$, while pair production is the most likely mechanism for photons above this energy (e.g. Rossi and Greisen 1941).

The energetic electrons produced in these interactions may then interact by ionizing atoms in the air, or by emitting a photon as they are decelerated in the electric field of a nucleus. The latter process is known as bremsstrahlung. For electrons with energies greater than $\sim 81\text{MeV}$ (known as the critical energy, E_c) bremsstrahlung is the most likely process. Below this energy, ionization dominates.

Thus in the energy regime above E_c , each photon will most likely interact to produce an electron - positron pair and each of those particles will most likely interact to produce more photons through bremsstrahlung. In this way, an electron - photon, or electromagnetic, cascade is built up. The cascade grows until the energy of the electrons drops below E_c , at which time energy will be lost to the atmosphere through ionization. As energy is lost, the number of electrons in the cascade falls.

The processes of bremsstrahlung and pair production have characteristic path lengths. In the case of bremsstrahlung this length is known as the radiation length (X_0) which has been estimated to be 36.1 gcm^{-2} in air (Linsley 1981). For photons with energy $\gg E_c$, the path length for pair production is

$$X_{p-p} = \frac{9}{7} X_0.$$

Eq. 2.6

The similarity of the two path lengths is not a coincidence; it reflects the similarity of the bremsstrahlung and pair production processes according to quantum electrodynamics.

The properties of pure electromagnetic cascades are now well understood (Kamata and Nishimura 1958). However, in cosmic ray air showers, the development of the electromagnetic cascade is dominated by the development of the hadronic component. Nevertheless, some useful information can be gained from the theory of pure electromagnetic cascades.

For example, Allan (1971) has modelled a pure cascade with the assumption that the path lengths for bremsstrahlung and pair production are equal (i.e. $X_o = X_{p-p}$). In this simple model, the number of particles (electrons, positrons and photons) in the shower at its maximum size (before ionization causes it to decay) is

$$N_{\max} = E_0 / E_c$$

where E_0 is the energy of the gamma ray which initiated the cascade. The depth in the medium at which this maximum size occurs is given by

$$X_{\max} = X_o \ln (E_0 / E_c)$$

(This parameter is known as the depth of maximum, or DOM). Thus, the important results of this analysis are that the number of particles in the shower at its maximum size is proportional to the primary energy and that the depth of maximum development is proportional to the logarithm of this

energy. In the case of real EAS, the size of the shower at maximum development is fairly model independent and is given by (Allan 1971)

$$N_{\max} = E_0 / (2 \times 10^9 \text{eV}) \quad \text{Eq. 2.7}$$

where N_{\max} here refers to the number of electrons (and positrons) in the shower.

The electrons in an electromagnetic cascade suffer multiple Coulomb scattering during their passage through the atmosphere. This process causes a spread, both longitudinally and laterally, in the shower front. Roberg and Nordheim (1949) have shown that the rms scattering angle is

$$\theta_{\text{rms}} \sim 0.7 / (1 + E/E_s) \text{ radians} \quad \text{Eq. 2.8}$$

where E is the energy of the electron and $E_s = 21\text{MeV}$ is the characteristic Coulomb scattering energy in air. Because of the energy dependence of the scattering function, the higher energy electrons are concentrated at the centre and front of a thin curved shower front, which has a thickness of $\sim 3\text{m}$ and a diameter of several hundred metres at sea level. Greisen (1956) has proposed a function which describes the lateral distribution of particle density in the shower front. It is based on the function derived for pure electromagnetic cascades by Kamata and Nishimura (1958) and has been modified so as to be a better fit to real EAS data. The resulting function is



known as the Nishimura-Kamata-Greisen (NKG) lateral distribution,

$$\rho(N, R) = \frac{C(s)N}{R_0} (R/R_0)^{s-2} (1 + R/R_0)^{s-4.5} \quad \text{Eq. 2.9}$$

where N = total number of electrons in the disc

R = distance from the shower core (m)

R_0 = Moliere radius $\sim 70\text{m}$

and $c(s) = \frac{\Gamma(4.5 - s)}{2\pi\Gamma(s)\Gamma(4.5 - 2s)}$, a normalising factor.

The variable s in this function is known as the "age" of the shower. In electromagnetic cascade theory it is defined as being between 0 and 1 before maximum, equal to 1 at maximum, and between 1 and 2 after maximum. In real EAS, s is still found to be a monotonic measure of the stage of shower development. A large value of s implies an "old", flat shower, one which developed a large distance from the detection level. The average sea level age for 10^{16}eV EAS is ~ 1.3 .

2.3 EAS Development.

The way in which air showers develop in the atmosphere is an important area of study. To a large extent, the development is dependent on the processes occurring in the hadronic core of the shower and on the nature of the primary particle. It will be shown that air shower development can be used to study the distribution of energy in the core (e.g. inelasticity, multiplicity) and the question of high energy cosmic ray composition.

The decay of the cascade after shower maximum is a process which is fairly well understood. At atmospheric depths well

past maximum, the influence of the hadronic core is minimal and the shower behaves like a pure electromagnetic cascade. The number of particles in the shower decreases exponentially with depth, with a scale factor (the attenuation length) of $\sim 200\text{gcm}^{-2}$. This figure may vary slightly with shower energy - for sea level shower sizes of $\sim 10^6$ particles, the attenuation length has been found to be 185gcm^{-2} (Clay and Gerhardy 1982). While this decay may be well understood, the way in which a shower grows and its behaviour around shower maximum are areas in need of further investigation.

Showers of the same energy initiated by nuclei of different mass can develop very differently. To illustrate this, consider two showers of equal energy, one initiated by a proton and the other by an iron nucleus. The first difference in development is caused by the two nuclei travelling different distances in the atmosphere before their first interaction. The proton mean free path in air is energy dependent and is $\sim 67\text{gcm}^{-2}$ at 10^{14}eV and $\sim 37\text{gcm}^{-2}$ at 10^{18}eV (Ellsworth et al 1982) while the mean free path for Fe nuclei is approximately constant at EAS energies and only $\sim 13\text{gcm}^{-2}$ (Westfall et al 1979). The depth of this first interaction is especially important since roughly half of the primary energy is distributed in this collision. Thus, protons will, on average suffer their first interaction deeper in the atmosphere than heavier nuclei, such as iron. The depth of the first interaction will also fluctuate more for proton showers than for iron showers. Because so much of the primary energy is released in this interaction, fluctuations in its depth will manifest themselves in fluctuations in the depth of shower

maximum.

After the initial interaction, the iron initiated shower will develop more quickly than the proton initiated shower. This can be understood in a simple way by considering the superposition model of shower development. This states that a shower initiated by a nucleus with mass number A and energy E may be considered as the sum of subshowers, each with energy E/A . Using this principle, an iron initiated shower will reach shower maximum at the same depth as a proton initiated shower with $1/56$ th of the energy of the Fe nucleus. Also, because of the statistical smoothing effect of the 56 subshowers, the development of Fe initiated showers will suffer smaller fluctuations than showers initiated by protons of the same energy.

An interesting feature of EAS development is the way in which the average depth of shower maximum increases with primary energy. A measure of this change was invented by Linsley (1977), and is called the elongation rate,

$$D_e = \frac{dX_m}{d \ln E} \quad \text{Eq. 2.10}$$

where X_m is the depth of shower maximum (in gcm^{-2}) and E is the primary energy. Linsley's Elongation Rate Theorem states that for a flux of primaries of the one composition, the elongation rate can be expressed as

$$D_e = (1-B)X_0 \quad \text{Eq. 2.11}$$

where X_0 is the radiation length for electromagnetic cascades

in air and B is a number which was originally taken as the exponent of the secondary pion multiplicity function, viz

$$\text{if } g \propto E^B \quad \text{Eq. 2.12}$$

$$\text{then } B = \frac{d \ln g}{d \ln E} = B_g$$

However, B is now taken to be a sum of two terms, B_g above, and another term which expresses the energy dependence of hadronic cross sections (Gaisser et al 1979),

$$B_\lambda = \beta \frac{d(\lambda_N + \lambda_\pi)}{d \ln E} \quad \text{Eq. 2.13}$$

where βX_0 is a dimensionless constant of order unity and λ_N and λ_π are the mean free paths in air for nucleons and pions respectively. The values of B_g and B_λ at high energies are, of course, model dependent. In scaling models, where $g \propto \ln E$, the value of B_g would be very low, and in the other extreme case, very high multiplicity models ($g \propto E^{1/2}$) would predict $B_g = 0.5$. Gaisser et al (1979) have used accelerator data to calculate a value of $B = B_g + B_\lambda = 0.23 \pm 0.12$ for energies up to 10^{12} eV.

The effect of a variable composition can be included in the elongation rate expression giving

$$D_e = (1-B) X_0 \left(1 - \frac{d \ln \langle A \rangle}{d \ln E}\right) \quad \text{Eq. 2.14}$$

where $\langle A \rangle$ is the average mass number at energy E . From this expression it can be seen that a change in elongation rate may

be caused by either a change in hadronic interactions (i.e. a change in B) or a change in primary composition. We shall now consider some numerical results of the theorem. Here it is more convenient to use D_{10} , the change in depth of maximum per decade of energy. If the composition is constant, and if we assume that the value of B quoted above is correct in the EAS regime, then $D_{10} = 67 \pm 10 \text{gcm}^{-2}$. It has been noted (Linsley and Watson 1981) that D_{10} cannot be much smaller than this figure. Even with $B_g = 0.25$ (a significant departure from scaling) and no change in B_λ , D_{10} would only decrease from 67 to 45gcm^{-2} . However, changes in D_{10} due to changes in composition could be very large. A change from the directly measured low energy composition to a pure iron flux over three decades of energy would reduce D_{10} from 67 to 42gcm^{-2} over that range. If the flux changed from pure iron to pure protons over a single decade, the elongation rate would be $D_{10} = 184 \text{gcm}^{-2}$.

2.4 Cerenkov Radiation.

When a charged particle passes through a dielectric medium with a velocity greater than the speed of light in the medium, an optical shock front is produced. (This shock front is analogous to the sonic boom induced by supersonic aircraft.) The light produced is known as Cerenkov radiation and was first observed fifty years ago (Cerenkov 1934, 1937). The definitive theoretical treatment of the radiation is given by Frank and Tamm (1937). We shall summarise some of the major results below.

As a charged particle moves past an atom in a dielectric medium it displaces the bound electrons of the atom, causing a

momentary polarization. Radiation is produced as a result of the time variation in this polarization. A coherent light front is produced only if the velocity of the particle is greater than the local speed of light. The angle of emission of the light with respect to the path of the particle is given by

$$\theta = \arccos\left(\frac{c}{vn}\right) \quad \text{Eq. 2.15}$$

where c is the speed of light in vacuum, v is the speed of the particle and n is the refractive index of the medium. Clearly, the threshold velocity is given by

$$v_{\min} = \frac{c}{n} \quad \text{Eq. 2.16}$$

and the maximum Cerenkov emission angle (for $v=c$) is

$$\theta_{\max} = \arccos\left(\frac{1}{n}\right). \quad \text{Eq. 2.17}$$

Our atmosphere is a dielectric medium with a refractive index of $n = 1.00029$ at standard temperature and pressure (STP). Following the treatment of Jelley (1967), if n is written in the form

$$n = 1 + \eta, \quad \eta \ll 1$$

then
$$\theta_{\max} \approx (2\eta)^{1/2} \text{ radians} = 81\eta^{1/2} \text{ degrees} \quad \text{Eq. 2.18}$$

and the threshold energy for emission is

$$E_{\min} = m_0 c^2 (2\eta)^{-1/2} \quad \text{Eq. 2.19}$$

where $m_0 c^2$ is the rest mass energy of the particle. Thus at STP the maximum emission angle is $\sim 1.3^\circ$ and the threshold energy for electrons ($m_0 c^2 = 0.51 \text{ MeV}$) is 21 MeV. The threshold energies for muons and protons are 4.3 GeV and 39 GeV respectively.

The rate of energy loss due to the Cerenkov mechanism for a particle of single electric charge and energy E is expressed by

$$\frac{dN}{d\ell} = 4\pi\alpha \left(1 - \frac{E_{\min}^2}{E^2}\right) \int \eta \frac{d\lambda}{\lambda^2} \text{photons } m^{-1} \quad \text{Eq. 2.20}$$

where $\alpha = 1/137$ is the fine structure constant. It can be seen that the spectral distribution of Cerenkov light is proportional to $1/\lambda^2$ i.e. the emission increases toward the UV region of the spectrum until limited by refractive index effects.

2.4.1. Cerenkov Radiation from EAS.

A typical extensive air shower contains a considerable number of particles with energies above the Cerenkov threshold. Allan (1971) has estimated the integral energy spectrum of electrons in an electromagnetic cascade at shower maximum to be

$$N(>E) = N_e / (1 + E/30) \quad \text{Eq. 2.21}$$

where N_e is the total number of electrons in the shower and E is energy in MeV. Given this expression it is clear that even at shower maximum (where the threshold energy will be larger than the sea level value of 21MeV) about half of the electrons in the shower will be capable of inducing Cerenkov emission. Light produced at all levels in the atmosphere will reach ground level with a lateral spread determined by the lateral spread of the electrons producing the radiation and the Cerenkov emission angle. The total flux of Cerenkov light is a measure of the total track length of the electrons in the shower with $E > E_{\min}$. This information can be used to infer the total energy of the shower. Also, because the light is received from all levels in the atmosphere, information can be gained regarding shower development.

Observations of Cerenkov light from EAS are made on clear, moonless nights. In clear conditions, the optical transmission of the atmosphere in the wavelength region of interest is better than 70% (Allen, 1955). The moon is a major source of background noise and its presence causes a significant reduction in the suitable observing time.

Since the first Cerenkov pulses associated with EAS were observed (Galbraith and Jelley, 1953) a number of groups have worked in this field. Observations have concentrated on features of the Cerenkov flux which can be related to shower development, in particular the depth of shower maximum. These include the time structure of the Cerenkov pulse and the lateral distribution of the light.

2.4.2. The Time Structure of Cerenkov Pulses.

The time structure of a Cerenkov pulse measured at ground level is not simply a consequence of the changes in path length as the shower front passes down through the atmosphere. The situation is more complicated because the refractive index of the atmosphere changes with depth. While the shower front moves with a velocity effectively equal to the speed of light c , the light moves with a velocity c/n , where n increases with depth. Thus the shape of the Cerenkov pulse is not only determined by geometric effects but also by refractive index effects.

The core distance at which the Cerenkov pulse is observed determines which of the two effects becomes dominant. It turns out that if the pulse is observed close to the shower core, light produced low in the atmosphere reaches the detector first. However, at large core distances the situation is reversed and light produced high in the atmosphere arrives first. For these reasons there is only a one to one relationship between arrival time and height of production for core distances $\sim 0\text{m}$ and $\gtrsim 150\text{m}$.

Jelley (1958) recognised that the Cerenkov pulse shape contained information about shower development. In early experiments (e.g. Boley et al, 1961) narrow angle detectors were used to record the Cerenkov light near the shower core. In these experiments, however, no dependence of pulse shape on other shower development parameters was demonstrated. Calculations by Bohm et al (1975) explained this lack of dependence. If the axis of the narrow acceptance angle detector was not parallel with the shower axis, the Cerenkov

pulse represented an oblique cross section of the shower and was in fact a measure of the electron lateral distribution. Here, the detector geometry played a large part in determining the Cerenkov pulse shape.

It has now been established that the alternative method, of using wide angle detectors at large core distances, is preferable and that it can provide information on EAS development. In principle, the technique has the capability of reconstructing the actual electron cascade profile (Fomin and Khristiansen, 1972). However, to do this it is necessary to determine the arrival time of the light front. In practice this is difficult to do as it requires an accurate determination of the shower direction. This problem was avoided by Orford and Turver (1976) who used a number of detectors and assumed that any particular point on the measured pulses (e.g. the 10% level on the rising edge) corresponded to one point in the development of the shower. Under this assumption, it was possible to define the shower axis and to reconstruct the shower profile to some extent. This work by the Durham group produced results on some Cerenkov development features (Hammond et al 1977) and the depth of shower maximum (Andam et al 1981).

Another approach is to use simulations to relate a particular parameter of the Cerenkov pulse to some specific feature of the development of the shower. An example of this is the theoretical relation of Kalmykov et al (1979) relating the full width at half maximum (FWHM) of the pulse at a core distance of 300m to the height of maximum (the distance to the shower maximum along the axis),

$$h_m = 17.05 - 9.17 \log (FWHM_{300}) \quad \text{Eq. 2.22}$$

where $FWHM_{300}$ is in nanoseconds and h_m is in kilometres. The form of this relationship has been verified by the recent simulations of Patterson and Hillas (1983a). In order to use this relationship, it is necessary to know the dependence of pulse width on core distance. This has been measured by Liebing et al (1983) for sea level shower sizes of $\sim 10^6$ particles and is found to have a power law form with an index of ~ 1.4 .

The extraction of depth of maximum from pulse width measurements has been practised at Akeno (e.g. Inoue et al 1981), Yakutsk (e.g. Kalmykov et al 1979) and Adelaide (e.g. Thornton and Clay, 1979, 1981). The interpretation of these and other data on the depth of shower maximum will be presented in Chapter Six.

2.4.3. The Lateral Distribution of Cerenkov Light.

In this section we shall give a brief introduction to the lateral distribution of Cerenkov light from EAS, the subject of this thesis. The detailed shape and its interpretation in terms of shower development will be discussed fully in Chapter Four.

The lateral distribution (LD) is the function that describes the lateral variation of Cerenkov flux with core distance. Consider the simple case where all the electrons in the shower are moving along the shower axis at the speed of light (figure 2.3). High in the atmosphere, where the

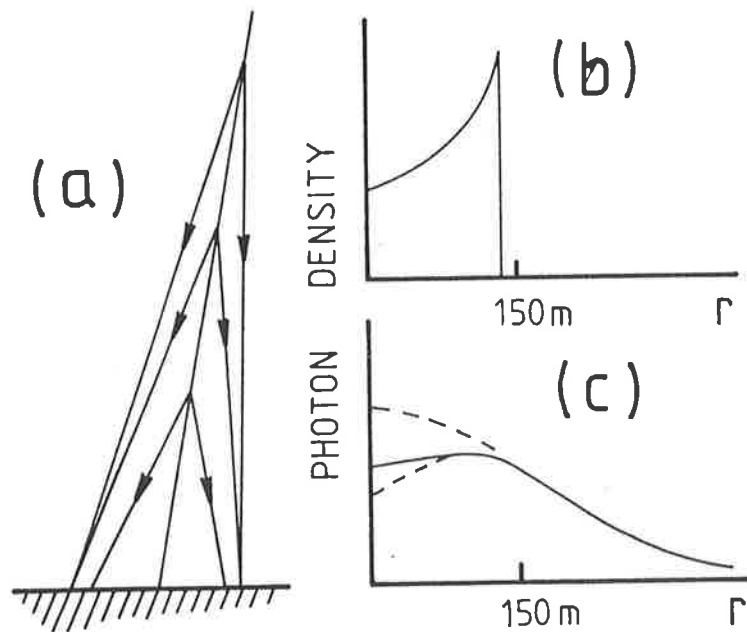


Figure 2.3: A simplified look at the lateral distribution of Cerenkov light. See text. (After Hillas 1982b).

refractive index of the air is smaller, the Cerenkov emission angle is smaller. Consequently, in this simple model, light originating from altitudes of 7 to 20 km all falls within a ring of ~ 110 to 145m in radius, changes in the emission angle compensating for changes in the height of production (fig. 2.3a). The corresponding LD is shown in figure 2.3b. However, in real showers where the electrons diverge from the shower axis because of multiple scattering, the Cerenkov photons are spread more widely and the "ring" is considerably blurred.

Since the first measurements of the LD were made (Chudakov et al 1960) a number of experiments and calculations have been carried out. Their aim has been to relate features of the shape of the LD to aspects of shower development. It is now established that the steepness of the LD is a measure of the distance between shower maximum and the observer along the shower axis. (see Chapter Four, sections 4.2, 4.3).

C H A P T E R T H R E E

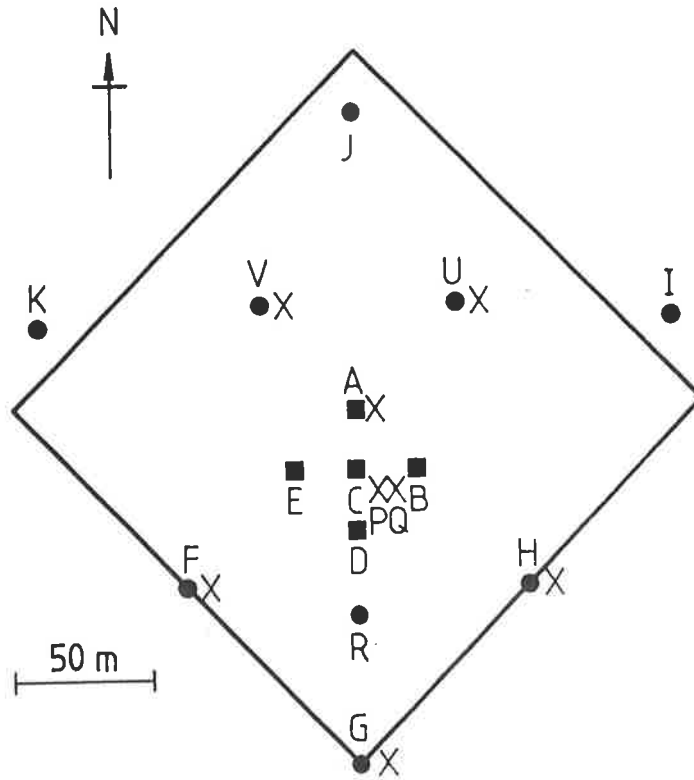
EXPERIMENTAL DETAILS

3.1 Introduction

This chapter will describe in detail the experimental arrangement used to measure the lateral distribution of Cerenkov light from extensive air showers. The experiment was carried out at the Buckland Park Research Station of the University of Adelaide, which is located at sea level altitude on a coastal plain approximately forty kilometres north of the city (35°S). While the site is not ideal for Cerenkov light studies because of an increasing problem of scattered city light and also the abundance of winter cloud, it has the advantage that a well-established cosmic ray particle array exists there with a sensitivity in the shower size region of interest. The air shower array will be discussed first, together with a description of some aspects of the recording system. A discussion of the Cerenkov light array and experiment will follow.

3.2 The Buckland Park Air Shower Array.

The air shower array at Buckland Park was originally established in 1972 using components from an array operated by the University of Calgary at Penticton, Canada. At the time that the experiment described here was carried out, the array was set out as shown in figure 3.1. Each of the 12 particle



- FAST TIMING AND DENSITY DETECTOR
 - DENSITY DETECTOR
 - X CERENKOV DETECTOR
- XL

Figure 3.1: The Buckland Park array, showing particle and Cerenkov detectors.

detector sites contains 1 square metre of 50mm thick plastic scintillator viewed by a 120mm diameter photomultiplier (RCA 8055). The central sites (A,B,C,D,E) also contain a faster 120mm photomultiplier (Philips XP 2040) for measuring the shower front arrival times. The array encloses an area of approximately 30 000 m² and is sensitive to showers with sea level sizes in the range $N_e \sim 5 \cdot 10^4 - 10^7$ particles. For a full description of the array characteristics, see Crouch et al (1981).

The array is used to provide measurements of the size, core location and arrival direction of a shower (see section 3.4). It also provides a number of prompt triggers useful for subsidiary experiments such as the Cerenkov lateral distribution study. The commonly used triggers are known as the "fast" trigger which requires a coincidence of more than 2 particles in each of the central five detectors (A,B,C,D,E) and the "slow" trigger which requires a fast trigger together with greater than 6 and 8 particles in detectors A and D respectively. The rate of fast triggers is approximately 1 min⁻¹, while the rate of slow triggers is approximately 8 hr⁻¹. The latter trigger was found to be optimum in terms of collecting area for shower sizes in the range $10^5 - 10^7$ particles (Crouch et al 1981). However in the Cerenkov experiment described here, a looser trigger than this was required. In fact, a modification of the fast trigger was used (see sect. 3.4).

3.2.1. The Array Recording System.

Prior to 1981 the array signals were processed by

predominantly home built electronics and the data written onto seven-track magnetic tape. The data were then transferred to the University's main computer (a CDC Cyber 173) for analysis. While this system worked very well as a dedicated data logger, it was unable to perform any on-line data analysis. Also, it lacked the facility for recording data from subsidiary experiments. To remedy these shortcomings a new measurement and control system was commissioned by the author in 1981-82. This system now runs the particle array and the Cerenkov lateral distribution experiment and is described in the following section.

3.2.1.1. The CAMAC Based Recording System.

The new electronics installed at Buckland Park consisted of a CAMAC based module system and a Data General Nova 4S minicomputer with a 12.5 Mbyte Winchester and diskette drives. CAMAC is an acronym for Computer Automated Measurement and Control and is a standard created by the ESONE Committee of the European Joint Nuclear Research Center (see for example Document EUR 4100e, JNRC, Ispra, Italy, 1969.). It is an international standard of computer interfaced modular electronics. The heart of any CAMAC system is the "crate", which is a receptacle capable of accomodating up to 25 plug-in modules. Station 25 is reserved for the crate controller, the module which interfaces the crate with the computer. The controller communicates with the other modules in the crate via the so called dataway, which is a series of bus and individual lines forming the motherboard of the crate.

Common types of modules in CAMAC systems include analogue

to digital converters (ADCs), time to digital converters (TDCs), scalers and latchable input/output data ports. Each module can have up to 16 addressable channels. The computer can perform an operation on a module by sending a command word to the controller. This command word (NAF) consists of three parts specifying the station number of the module to be serviced (N, ranging from 0-22) the sub-address of the channel required (A, 0-15) and the code of the function to be performed (F, 0-31). If the function code specifies a read or write operation, up to 24 bits of parallel information can be transferred between the module and the computer.

When a module requires servicing (for example an ADC after it has been triggered) it can be configured to send a "Look at Me" (LAM) signal to the crate controller. When the controller receives one or more of these signals it can be made to send an interrupt signal to the computer. This is the most efficient way to run a CAMAC system; the computer can be busy performing other functions (for example data analysis) while the CAMAC system is idle. Once an interrupt signal is received however, the computer can immediately service the crate through user-written interrupt routines.

As an example of a typical servicing procedure consider the case of a lone 12 channel ADC in a CAMAC crate. This module would have 12 inputs for pulses or voltage levels together with "start" or "trigger" input. On the receipt of a "start" signal the device would capture the signals at each of the 12 inputs and would proceed to digitize them. When this operation was complete, the module would send a LAM signal to the crate controller which would in turn send an interrupt

signal to the computer. After identifying the ADC module as the source of the LAM the computer would send out a series of NAF commands to read the digitized data. There would be 12 such commands sent out; each would have the same N (station number) and F (function code) components but would differ in the A (sub-address) part. This section of the command would increment from 0-11 in order to read the contents of each of the 12 channels of the ADC.

Work began on the Buckland Park CAMAC system in 1981. The hardware includes a Kinetic Systems CAMAC crate and a Nuclear Enterprises 9030 CAMAC controller containing a NE9039 Nova interface board. We had a lot of trouble interfacing the new equipment with the computer; in particular we found it impossible to induce the controller to send interrupts to the computer. Initially we suspected problems with our own software but after some time we discovered that it was a hardware problem. After a long investigation the fault was traced to a design fault in the NE9039 Nova interface board. It appears that our board was one of the first produced by the manufacturer. Although much time was wasted tracking down the fault, those weeks were a valuable learning experience.

Once these problems had been sorted out, a local computing science graduate, Anthony Berglass, was hired to write a versatile software package for our system. His brief was to write a program to run the Buckland Park particle array but to allow for additions to run other experiments. This was achieved quite successfully. Other software has been added from time to time by the author, including the code necessary for the Cerenkov lateral distribution experiment.

The CAMAC modules in the system, which were in use during the Cerenkov experiment included a 12 channel peak sensing ADC (LeCroy 2259A) and a 8 channel TDC (LeCroy 2228A) for the particle array, and a 12 channel integrating ADC (LeCroy 2249SG) for the Cerenkov array. A LeCroy 2551 12 channel scaler is used to monitor individual particle detector triggering rates and a data logger is used to input data from the array barometer, thermometers and clock. Another module provides output signals under computer control for use in various experiments.

The data collected, which can be partially analysed on the Nova computer (depending on the event rate), is finally transferred to diskette or nine track magnetic tape for further analysis at the University.

The aspects of the recording and control system pertaining to the Cerenkov lateral distribution experiment will be discussed in more detail in the following section.

3.3. The Cerenkov Lateral Distribution Experiment.

3.3.1. The Array

The array of Cerenkov detectors used in this experiment was based on the one developed by Kuhlmann (see for example Kuhlmann and Clay 1981). The disposition of the detectors with respect to the particle array is shown in figure 3.1. Kuhlmann's site 300m south of C has been discontinued and two new sites (U and V) have been added to the north. Each Cerenkov site consists of a 190mm open faced photomultiplier (EMI 9623B, S-11 photocathode) surrounded by a cylindrical

collimator allowing viewing within approximately 45° of the zenith. (The collimators have a diameter of 520mm and a height of 130mm). The photomultipliers are not fast, but they do have the advantage of a relatively large photocathode. The impulse response of the tube has a rise time (t_r) of $\sim 12\text{ns}$ and a full width at half maximum (FWHM) of $\sim 60\text{ns}$. In the interests of retaining an acceptable signal to noise ratio, it was thought necessary that this impulse response not be degraded appreciably with subsequent electronics and cables. However compromises had to be made on the basis of cost. Thus, the on-site preamplifiers chosen to replace Kuhlmann's (which had become unpredictable) were based on the economical and reliable Le Croy TRA-1000 monolithic chip which was used in the current amplifying mode ($t_r \sim 24\text{ns}$). The signal cable used for most sites was the type RG-58. However for the distant site, L and the two newer sites (U,V) the larger bandwidth cable RG-8 was used. The signals were amplified in the central laboratory by large bandwidth (50MHz) line receivers. The impulse response of a typical site was measured at the central laboratory to have a risetime of $\sim 30\text{ns}$ and a FWHM of 90ns .

Figure 3.2 shows a block diagram of the Cerenkov recording system. The signals from the photomultipliers are amplified at the sites by the preamplifiers mentioned above (gain ~ 60) and then travel down coaxial cable to the central laboratory. The line receivers have a gain of 2 and each have two outputs - a normal output and an attenuated (-20dB) output. The normal signals are fed to discriminators and the attenuated signals fed to the CAMAC integrating ADC (Le Croy 2249SG). This module is a 12 channel device with the facility that each channel can

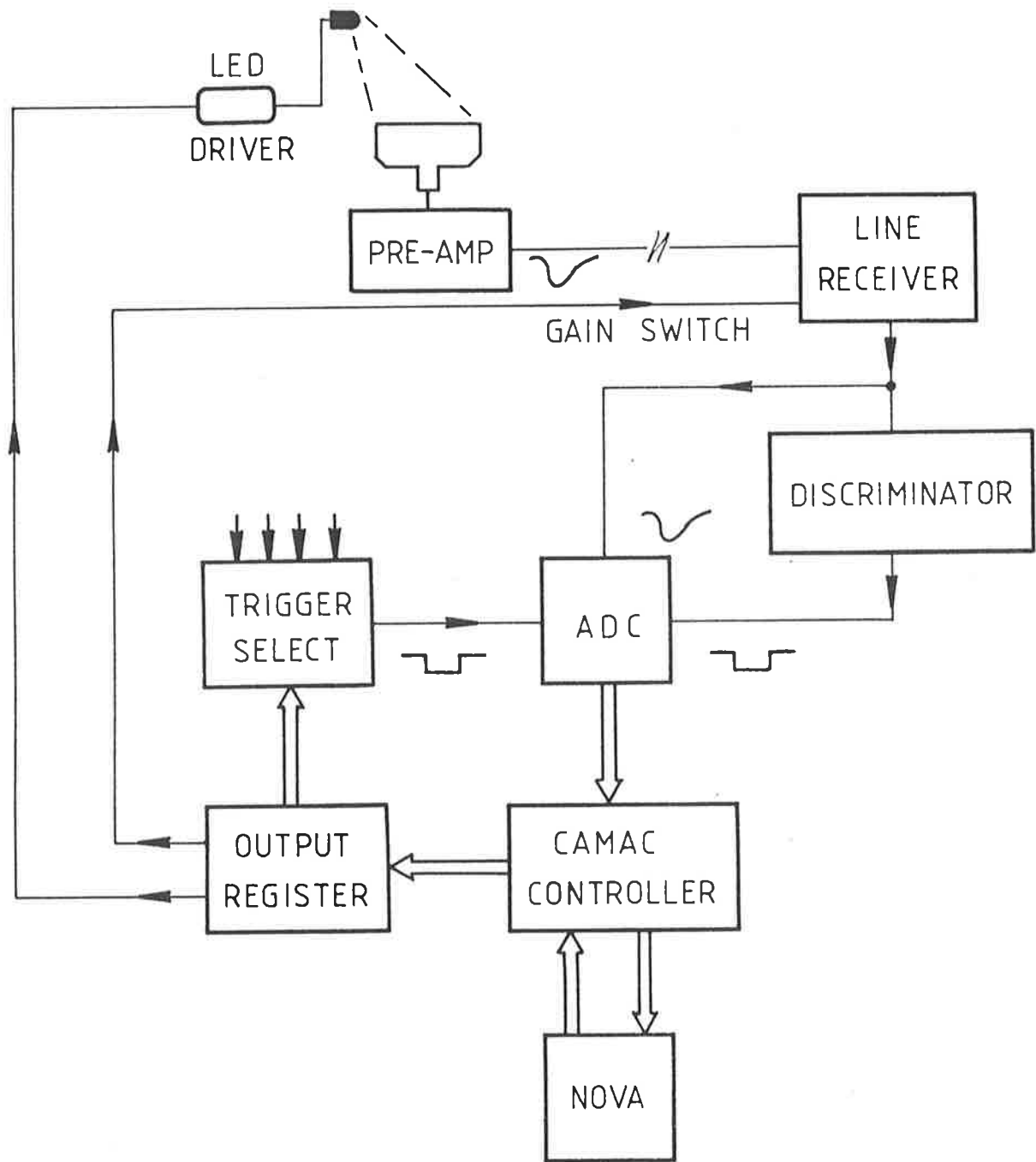


Figure 3.2: Block diagram of the Cerenkov lateral distribution array recording system.

be separately gated. The digital output of each channel is proportional to the amount of charge injected into the input during the gate signal. In this particular application, the amount of charge is in turn proportional to the integrated flux of light incident on the face of the photomultiplier. These gate signals are produced by the discriminators, which are set at their minimum threshold levels ($\sim 30\text{mV}$). The gate signals are fed into the ADC together with the photomultiplier pulses, the latter being delayed by approximately 30ns to allow for discriminator triggering jitter caused by the finite risetime of the pulses. The gate pulse width is important as it determines the integration time for the signal. It needs to be wide enough to enclose the signal pulse (at least from the 10% level on the rise to the 10% level on the fall of the pulse) but should not be so wide that an excessive amount of background noise is included in the integration. It is here that the advantage of a large bandwidth system becomes apparent. Taking these points into consideration, the gate widths were set at $\sim 250\text{ns}$.

The integrating ADCs give a full scale count of 1024 corresponding to an integrated charge of 256pC into $50\ \text{ohms}$. With the shape of the pulses as described, this corresponds to a pulse height of $\sim 150\text{mV}$. In terms of the pulse height from the unattenuated output of the line receiver this value is 1.5V . On the other hand, the minimum pulse height which can be digitized is determined by the discriminator thresholds which are set at 30mV . Thus the dynamic range of the system is approximately 50. This is higher than was possible with the system used by Kuhlmann which was an oscilloscope/camera based

In response to an examiner's query about the effect of the limited dynamic range of the Cerenkov system on the conclusions of this thesis, a simulation of the Cerenkov array bias was carried out. This was not done before because it was thought that any bias present would be small compared with the bias associated with the particle array (section 5.3). However, the results of the simulation show that this assumption would only be strictly true for a system with a dynamic range somewhat larger than 50. It was found that at low energies, any bias present in the Cerenkov array is negligible when compared to that present in the particle array, and that at the energy at which the particle array becomes unbiased, the Cerenkov array is also completely free of bias. However, above an energy of $\sim 2 \times 10^{16}$ eV, the Cerenkov array does become less sensitive to lower developing (for example, proton) showers. This may well explain why a transition back to a predominantly light composition is not seen in the data (see section 5.5). However, the fundamental conclusion of the thesis with respect to composition is still intact; the composition appears to be rich in iron in the region around 10^{16} eV.

system. While a still larger dynamic range would be desirable, the figure of 50 was considered quite adequate.

This section has described some of the hardware associated with the Cerenkov recording system. Data was collected from the system during the observing periods whenever an air shower was detected by the particle array. This data, together with particle density and timing information and the barometric pressure were recorded on diskette for analysis at the University.

3.3.2. Cerenkov Pulse Height Calibration.

There are two aspects of pulse height calibration which must be addressed in an experiment of this sort. They will be discussed separately in the following sections.

3.3.2.1. Monitoring of Individual Tube Gains.

In order to optimise the accuracy of Cerenkov flux measurements, the gain of each site was monitored during each observing night. The causes of gain changes are two-fold. The EMI 9623B photomultipliers have a gain/temperature coefficient which was measured to be $\sim -1.3\%$ per degree C. Given a typical temperature change of $\sim 10^0$ during a night, such a gain change is not insignificant. Also, because the tubes are operated in an environment where the ambient light level is relatively high their anode currents can exceed the manufacturer's recommended operating limit. Under these conditions the gain of the tube can alter with changes in the background light intensity. Again the resulting gain changes can be significant - especially during the passage overhead of the Milky Way.

To monitor the tube performance, each site is fitted with a green LED flasher which produces light pulses with temporal characteristics similar to those of atmospheric Cerenkov pulses. The device is mounted on the collimator at the site in such a way that the LED light pool illuminates the whole photocathode uniformly. To overcome the temperature dependence of the light output of the LED itself, the LED, together with the other temperature sensitive electronics, is encased in a stabilised copper oven with an opening at one end. This oven is embedded in thermal insulation inside a weatherproof plastic tube with a perspex window. The heating element is a resistor in close thermal contact with the outside of the copper tube. The temperature is controlled by a commercially available oven controller chip (see circuit diagram, Fig. 3.3) which is also in close thermal contact with the copper. Many prototypes of the device were constructed. It was found that it was very important to have the three oven components (the copper tube, heater and controller/sensor) in close thermal contact. This was achieved with the help of liberal amounts of thermally conducting grease. Also when using an oven controller of this type, the heater element is periodically turned on and off to maintain the temperature. Care had to be taken to ensure that the copper tube had enough thermal capacity to smooth out these sudden influxes of heat. Finally, it was found that good insulation was important. The resulting device has proved to be very successful. The short term stability is very good and the change in light output from the flasher over a thirty degree change in ambient temperature was measured to be of the order of 2%. In the field the temperature controllers were set

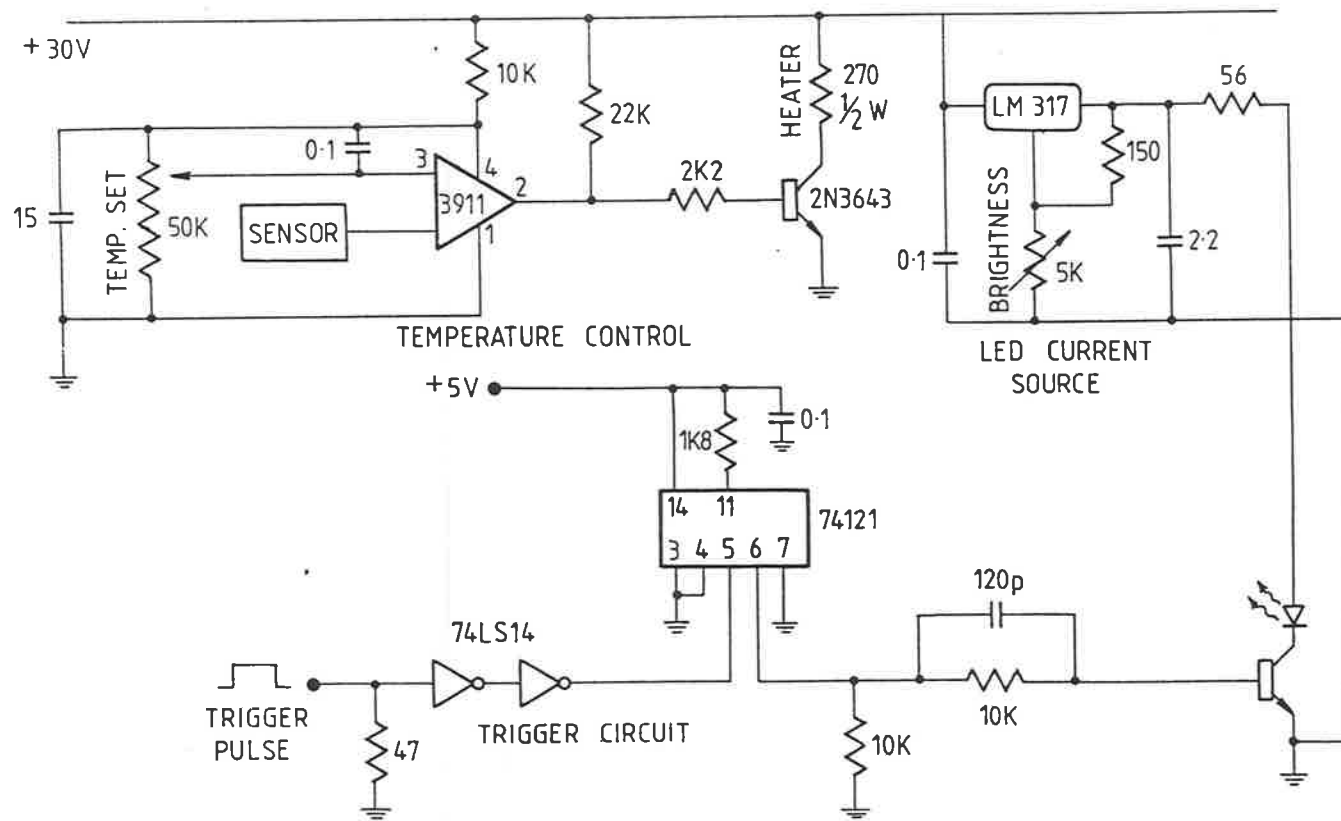


Figure 3.3: Circuit diagram of the temperature stabilised green LED flasher.

at 40°C.

The flashers are activated by TTL signals from the central laboratory which are generated by the CAMAC output register. At the same time the computer programs the trigger select device (fig. 3.2) which changes the source of the ADC "start" signal from the particle array to the discriminator output of Cerenkov site A (the closest Cerenkov site to the central laboratory). The system then measures a series of twenty LED pulses from each site and calculates a mean pulse height together with a standard deviation. The pulse height is a measure of the gain of the site while the standard deviation is an uncertainty of the uncertainty in the measurement, an uncertainty caused largely by the fluctuating background night sky. (The inherent jitter in the flasher itself is insignificant here). Thus, besides monitoring the gain of each site it is possible to monitor the affect of the background noise on the measurement of a Cerenkov pulse. the latter information is used to assign weights to the Cerenkov data during analysis (see section 3.3.3).

This calibration procedure was activated automatically after every 10 events during the observing periods.

3.3.2.2. Relative Calibration of Cerenkov Sites.

A knowledge of the relative gains of individual Cerenkov detectors is obviously necessary in a lateral distribution experiment. Several methods of performing this intercalibration were investigated early in the experiment.

A calibration light source must have spectral distribution which is compatible with the Cerenkov spectrum (Chapter 2,

section 2.4) and the spectral response of the photomultiplier. The 9623B photomultipliers have S-11 photocathodes peaking around 480nm, with the exact shape of the response curve varying slightly from tube to tube. Because of this variation it was thought advisable that the chosen light source have its spectral peak near the peak in the response of the tube (i.e., the blue region). It should be pointed out here that the use of green LEDs as monitoring devices as described in the previous section does not contradict this requirement. This is because the shape of the spectral response curve of an individual tube is not expected to change significantly with time. So, even though the spectrum of light produced by the green LED peaks at 560nm (corresponding to a point on the trailing edge of the tube response) it is thought to be an appropriate source for the measurement of the gain of a particular tube. It would be unwise however to use a green source for the intercalibration of tubes whose spectral responses were slightly different - small differences in the response shapes could then translate to large apparent differences in gain.

A source of suitable light was therefore sought. An initially promising idea was put forward by R.W. Clay. He suggested using the background of atmospheric Cerenkov light as an intercalibration source. The pulse height spectrum of Cerenkov light pulses from small air showers measured by a single detector is known to follow a power law form with a differential index of approximately -2.5 (Hartman et al 1977). The method suggested involved collecting a pulse height spectrum for a short time from each of the sites in turn, under

X ,
computer control. The spectra would all have the same power law index but would be shifted laterally according to the relative gains of the sites. The advantages of this method as first proposed were two-fold. Firstly, the calibration light source had spectral characteristics identical to those of the Cerenkov pulses from larger air showers. Secondly, the method was seen as a very quick and easy one. Problems arose when the method was put into practice, however. It was found that the expected power law spectrum was swamped by a much steeper spectrum at small pulse heights. The source of this light was unclear, although it was probably associated with scattered city light. In order to acquire a Cerenkov spectrum it was therefore necessary to increase the threshold level on the site. This increased the running time required to perform the intercalibration significantly and therefore lessened the appeal of the method. Consequently this technique was abandoned. It may have been possible to use the steeper spectrum as the intercalibration tool, but as its source was uncertain this was considered hazardous.

Another source of light considered for the intercalibration procedure was the scintillation light from a NaI(Tl) crystal irradiated with mono-energetic γ -rays. The emission spectrum of the light is in the blue region and so is, in that regard, suitable for the application. However, the source was not found to be ideal because of the problems associated with illuminating the entire 190mm diameter face of the photomultiplier. This was believed to be important even though a great deal of time was spent adjusting each photomultiplier base to maximize the uniformity of response

across the face.

The third method investigated, and the one which was finally adopted, became possible with the availability of a blue LED (Siemens SFH 710). These became available in 1982 and although expensive (~\$A250) were thought to be a worthwhile purchase. The peak emission wavelength of the blue LED (480nm) is close to the peak response wavelength of the S-11 photocathode. The flasher circuit described in the previous section was modified for the blue LED and again the device was enclosed in a temperature controlled environment. The flasher was mounted on a portable tripod (designed to sit above the tube) which incorporated a field lens which ensures that the tube faces are illuminated uniformly by the LED. The unit is therefore a standard reference light source capable of being moved from site to site for intercalibration purposes. However, there is one major disadvantage associated with the blue LED. The LED has been designed to produce pulses with a minimum rise time of $\sim 0.5\mu\text{s}$ (similar to the risetime of NaI(Tl)), while the recording system used has been tailored to cope with photomultiplier pulses with FWHM $\sim 100\text{ns}$. Consequently the blue LED calibration pulses cannot be recorded via the CAMAC integrating ADC. Instead these signals are measured with an oscilloscope at the output of each line receiver inside the central laboratory. At about the same time measurements are made of the individual green LED signals using the computer controlled procedure described in the previous section. Thus at the end of the intercalibration a set of oscilloscope measurements of blue LED signals is available together with corresponding measurements on the computer of the

green LED signal. Using a combination of the two sets of data it is possible to calculate the relative gains of the sites at any time by performing another computer controlled green LED calibration. During the period of the experiment, a blue LED calibration was done monthly. Given the observed stability of the individual green LED flashers, even this was probably too often.

3.3.3. Cerenkov Data Reduction.

Here we describe briefly the conversion of an output "count" from the integrating ADC into a measurement of the Cerenkov flux incident on a detector. The fluxes used in this work are expressed in arbitrary units. The conversion to absolute values (photons m⁻², for example) was not necessary.

The information available with each measurement was

- a. COUNT, the output from the ADC. Each channel of the ADC was calibrated regularly with a pulse generator to provide a relationship between the output count and pulse area (in arbitrary units),

$$AREA = A (COUNT - B) \qquad \text{Eq. 3.1}$$

where A and B are constants.

- b. GL, GLDEV, the mean and standard deviation of the ADC counts measured during the most recent green LED calibration of the site. (The calibration was carried out at intervals of ~10 minutes). GL provided a measure of the gain of the system and GLDEV was an

indication of the accuracy of any flux measurement.

- c. BL, a measurement (in millivolts) of the blue LED signal at the site.
- d. GLB, a green LED measurement, taken at the time of the blue LED calibration.

The flux F , and a measure of its uncertainty, SIGF, were then calculated in the following way,

$$F = \frac{\text{AREA}}{(\text{GL}-\text{B})} \cdot \frac{(\text{GLB}-\text{B})}{\text{BL}} \sec\theta$$

Eq. 3.2

$$\text{SIGF} = \frac{A(\text{GLDEV}-\text{B})}{(\text{GL}-\text{B})} \cdot \frac{(\text{GLB}-\text{B})}{\text{BL}} \sec\theta$$

where θ is the shower zenith angle.

3.4. Analysis of Particle Data.

A modified version of the Buckland Park particle array "fast" trigger was used in this experiment. The triggering requirement was a density of at least 2 particles m^{-2} in detector C and any two of the remaining fast detectors (A,B,D,E). This provided an event rate in excess of 1 per minute. However, the results described in this thesis were derived from a subset of the data collected. The selection criteria applied were imposed in order to obtain well analysed particle array events. (The consequences of this selection process are discussed in Chapter Five). Thus the events analysed

had the following properties,

- a. At least 3 non-colinear timing measurements, and
- b. At least 5 particle density measurements.

The details of the analysis procedure will not be discussed here. A similar procedure is described by Gerhardy (1983). However, briefly, the shower zenith and azimuth angles were calculated using a least squares fit to the timing measurements, assuming a planar shower front. The shower size, age and core location were then estimated assuming an NKG lateral distribution (described in Chapter Two, section 2.2.3.). The typical accuracy of shower directions was found to be $\sim(2.5 \sec\theta)^0$ where θ is the shower zenith angle. Through simulations it was found that a typical core location error was $\sim 4\text{m}$ for a 10^6 particle shower landing at $(20\text{m}, -20\text{m})$ with respect to C (Gerhardy 1983).

3.5 Conclusion.

The Cerenkov system described here is in a number of areas a step forward from the original system built by Kuhlmann. The automation of the measurements has been the main improvement, allowing for a possible collection rate of up to $\sim 10\text{Hz}$. There has also been an increase in the dynamic range of the system with the new measurement electronics.

An important feature of this system is the accuracy with which calibrations can be performed. The green and blue flasher units have been very successful tools. They provide a

reliable and accurate measure of the relative gains of the sites, allowing for a more detailed study of the shape of the Cerenkov lateral distribution.

C H A P T E R F O U R

THE SHAPE OF THE LATERAL DISTRIBUTION

4.1 Introduction.

The notion that atmospheric Cerenkov light from EAS contains information on shower development was first put forward by Brennan et al (1958) and Chudakov et al (1960). Since that time, a number of experiments and calculations have been performed to try to relate one property of the radiation, its lateral distribution, to one aspect of development, the depth of shower maximum. It is generally believed that the "slope" of the lateral distribution is a measure of the distance between the observer and shower maximum along the shower axis; steep lateral distributions are associated with showers which develop close to the observer. The question of the most appropriate measure of this slope, and how it is related to the distance to maximum, is the subject of this chapter. We shall begin with a review of the published work in the field, and shall later move on to the author's measurements of the lateral distribution for showers with sea level sizes of $\sim 10^5$ - 10^7 particles.

4.2 Early Work.

One of the first calculations of the expected shape of the lateral distribution was made by Jelley and Galbraith (1955). In this work, the showers were assumed to be electromagnetic cascades in which the lateral spread of the

shower electrons was ignored. The results were flat lateral distributions, each with an intensity cut off at $\sim 125\text{m}$. This result is as expected, given the reasons outlined in Chapter 2, section 2.4.3. The more realistic calculations of Goldanski and Zhdanov (1954) and Zatsepin and Chudakov (1962) followed. The latter study included the important ingredients of Coulomb scattering, realistic angular and energy distributions for shower particles, and three dimensional shower structure. The calculation was performed for proton-induced showers with energies $\lesssim 10^{16}\text{eV}$ for observers at sea level and an altitude of 3860m. The resulting lateral distributions showed evidence of an inflection at 125m, and the connection between the shape of the distribution and shower development was established in that the lateral distribution at mountain altitude (closer to shower maximum) was steeper than at sea level for the same primary energy.

The first measurements of the lateral distribution were made in the Pamir Mountains, USSR (alt. 3860m) by Chudakov and Nesterova (1958) and Chudakov et al (1960) using an array of Cerenkov detectors in association with a particle array. The Cerenkov array consisted of eight parabolic mirrors, each with a photomultiplier at its focus. The results were found to be in reasonable agreement with the calculations of Zatsepin and Chudakov.

The difficulty of interpreting results from experiments in which mirrors are used as light collectors (Sitte 1962, Böhm et al 1975) led to the use of open faced photomultipliers with large fields of view ($> \pm 30^\circ$) in later studies. These include the experiments of Krieger and Bradt

(1968,1969) performed at Mt. Chacaltaya (alt. 5200m) and those of Egorov et al (1971 a,b) and Dyakonov et al (1973) performed at Yakutsk (alt. 100m). The Yakutsk measurements were made on showers with primary energies $>10^{17}$ eV. The results have been compared with the calculations of Dyakonov et al (1975) who based their work on that of Zatsepin and Chudakov, but included an allowance for Rayleigh scattering of the light in the atmosphere and a more realistic electron lateral distribution. It was found that the agreement between the experiment and the calculation was good, although the experimental distributions were steeper than expected at large core distances (>300 m) for the most energetic showers.

Early results of the Durham group's experiment at Haverah Park were reported by Hammond et al (1977, 1978). Measurements of the lateral distribution were made in the core distance range 150m - 600m for showers with primary energies $>10^{17}$ eV. The average lateral distribution was shown to broaden with increasing distance to shower maximum. Also, the lateral distribution was shown to steepen with an increase in the particle array primary energy estimator $\rho(500)$ (the particle density measured by a water Cerenkov detector at a distance of 500m from the shower axis). Since high energy showers maximise low in the atmosphere, this demonstrates again the connection between the shape of the lateral distribution and the distance to shower maximum.

Similar results were reported by Kuhlmann et al (1977) working at Buckland Park, who measured the lateral distribution of smaller showers (10^5 - 10^6 particles at sea level) out to ~ 300 m from the axis. It was found that the average lateral distributions were steeper for the showers with

larger sea level sizes, and for showers arriving from smaller zenith angles.

4.3 The Shape of the Distribution and its Interpretation.

One of the first theoretical studies concerning the relationship between the shape of the lateral distribution and air shower development was that of Smith and Turver (1973). Here, Monte Carlo simulations were performed for proton-initiated showers with energies between 10^{15} eV and 10^{18} eV. A major result was that the ratio of the Cerenkov flux at 100m and 600m, $Q(100)/Q(600)$ was a function of the depth of shower maximum, DOM (for vertical showers). A ratio of 20 corresponded to a DOM of just over 600gcm^{-2} while one of 80 corresponded to a DOM of $\sim 850\text{gcm}^{-2}$. Also it was found that the flux at a core distance of $\sim 300\text{m}$ was essentially independent of shower development, and was a measure of the energy of the primary proton.

In the early experimental work of the Durham group at Haverah Park (Orford et al 1975, Hammond et al 1977, 1978), the lateral distributions were well fitted by a structure function of the form

$$Q(r) = Cr^{-\gamma} \quad \text{Eq. 4.1}$$

for a core distance range $100\text{m} < r < 500\text{m}$ and primary energies $> 10^{17}$ eV. The exponent γ (which typically had values between 1 and 3) was found to vary with the primary energy estimator, $\rho(500)$, and the shower zenith angle, θ , in the following way,

$$\gamma = 1.20 - 0.27 \times \log \rho(500) - 3.55 \times \cos \theta \quad \text{Eq. 4.2}$$

(Hammond et al 1978). This expression gave a figure for the elongation rate of $85 \text{gcm}^{-2}/\text{decade}$ which was consistent with theoretical calculations for energies $>10^{17} \text{eV}$. With the move of their experimental site to Dugway, Utah (depth $\sim 835 \text{gcm}^{-2}$) the Durham group changed the structure function to

$$Q(r) = C(r+r_0)^{-\delta} \quad r_0=50\text{m} \quad \text{Eq. 4.3}$$

in the core distance range $50\text{m} < r < 500\text{m}$. This new function was better able to take account of an observed change in slope around 100m . The exponent δ (with typical values between 1 and 4) was shown to be a measure of the distance between the observer and shower maximum. This result was strengthened by the simulations of Protheroe and Turver (1979). They performed Monte Carlo calculations of proton, α particle and iron nuclei induced air showers based on the Feynman scaling model of particle interactions. The results confirmed that the parameter δ was a measure of the depth of maximum for the Dugway experiment and that changes in the lateral distribution due to changes in the composition of the primary, its energy or the particle physics processes, only manifest themselves through changes in the development of the electromagnetic cascade and the depth of maximum. A linear relationship between δ and depth of maximum was produced which was shown to be independent of the energy and composition of the primary. Similar, but less precise conclusions had been drawn by

Ivanenko et al (1977).

In more recent experimental work, the Durham group have continued to use Eq. 4.3 to locate the shower core, but have used the function

$$R(r_1, r_2) = Q(r_1)/Q(r_2) \quad \text{Eq. 4.4}$$

the ratio of fluxes at two core distances, to characterise the lateral distribution (Chantler et al 1981, Andam et al 1982). Three arrays of different sizes were used to investigate the lateral distribution in the energy range 3×10^{15} - 5×10^{17} eV. The values of r_1 and r_2 were different for each array and the function $R(r_1, r_2)$ was related to the depth of maximum using the simulations of McComb and Turver (1982).

The lateral distribution of Cerenkov light from low energy showers in the range 2×10^{13} eV to $\sim 10^{15}$ eV has been investigated by Tornabene (1979). For the very low energy showers, searchlight mirrors were used as light collectors. An exponential structure function of the form

$$Q(r) = A \exp \left(-\left(\frac{r}{B}\right)^c \right) \quad \text{Eq. 4.5}$$

was used to locate the shower core and the function

$$P = 20 \log \left(\frac{Q(50)}{Q(150)} \right) \quad \text{Eq. 4.6}$$

was used to characterise the lateral distribution.

The Adelaide group working at Buckland Park has also used an exponential structure function,

$$Q(r) = A \exp(-br/10^4). \quad \text{Eq. 4.7}$$

Kuhlmann and Clay (1981a) examined this function in the sea level size range $10^5 - 10^6$ particles. The normalization parameter, A, was found to be correlated with the sea level shower size. This is to be expected since the light near the shower core is known to be produced late in the life of the cascade. The value of b (which ranges in value from ~ 70 to ~ 150) was found to decrease with increasing zenith angle and good agreement was found with the work of Tornabene in the overlapping size range. Kuhlmann et al (1981) have also shown a marked correlation between the b parameter and time profile measurements of individual showers.

Recently, Patterson and Hillas (1983b) have performed detailed Monte Carlo calculations of the shape of the lateral distribution and the relationship between the shape and the distance to shower maximum, H_m (in kilometres). The details of the simulation are given in the paper, and in Hillas (1982b). Briefly, proton showers are simulated assuming a radial scaling model with a rising cross section. The Cerenkov emission from the shower particles with energies $> 20\text{MeV}$, the Cerenkov threshold, was calculated by summing the emission from individual gamma-initiated sub-showers injected regularly along the shower axis. A realistic atmospheric transmission model was used, together with a photomultiplier optical frequency response matching that of a S-11 photocathode.

A feature of the results of Patterson and Hillas is a shoulder in the lateral distribution at $\sim 150\text{m}$ from the shower axis. This shoulder is especially prominent for showers which develop at a large distance from the observer. The shoulder is a consequence of the Cerenkov ring which was discussed in simple terms in the final section of Chapter Two. There we made the point that if we considered all the shower particles to be moving along the shower axis, then all the Cerenkov radiation emitted between the heights of 7 and 20km would land on the ground in a ring of ~ 110 to 145m radius, changes in the Cerenkov emission angle being compensated by changes in the emission height. In a real shower, the ring is blurred considerably because of the Coulomb scattering of the shower electrons, but Hillas (1982b) points out that the ring does not completely disappear for showers which develop high enough to form it. This is partly because the angular distribution of particles in an electromagnetic cascade is far from Gaussian in form (a form assumed by Zatsepin and Chudakov 1962) and has a sharp peak near 0° , which means that appreciable numbers of particles are moving along near the shower axis (Hillas 1982a). However, if most of the shower develops below 7km, the ring will be much less obvious.

An example of the results of Patterson and Hillas is shown in figure 4.1. Here the lateral distribution expected for an average 10^{16}eV proton induced shower at a zenith angle of 15° ($H_m = 4.4\text{km}$) is shown together with the contributions of 3 of the 17 10GeV subshowers. It can be seen that the Cerenkov ring is obvious in the subshower injected high in the atmosphere (no. 4) and is completely blurred for subshower 12

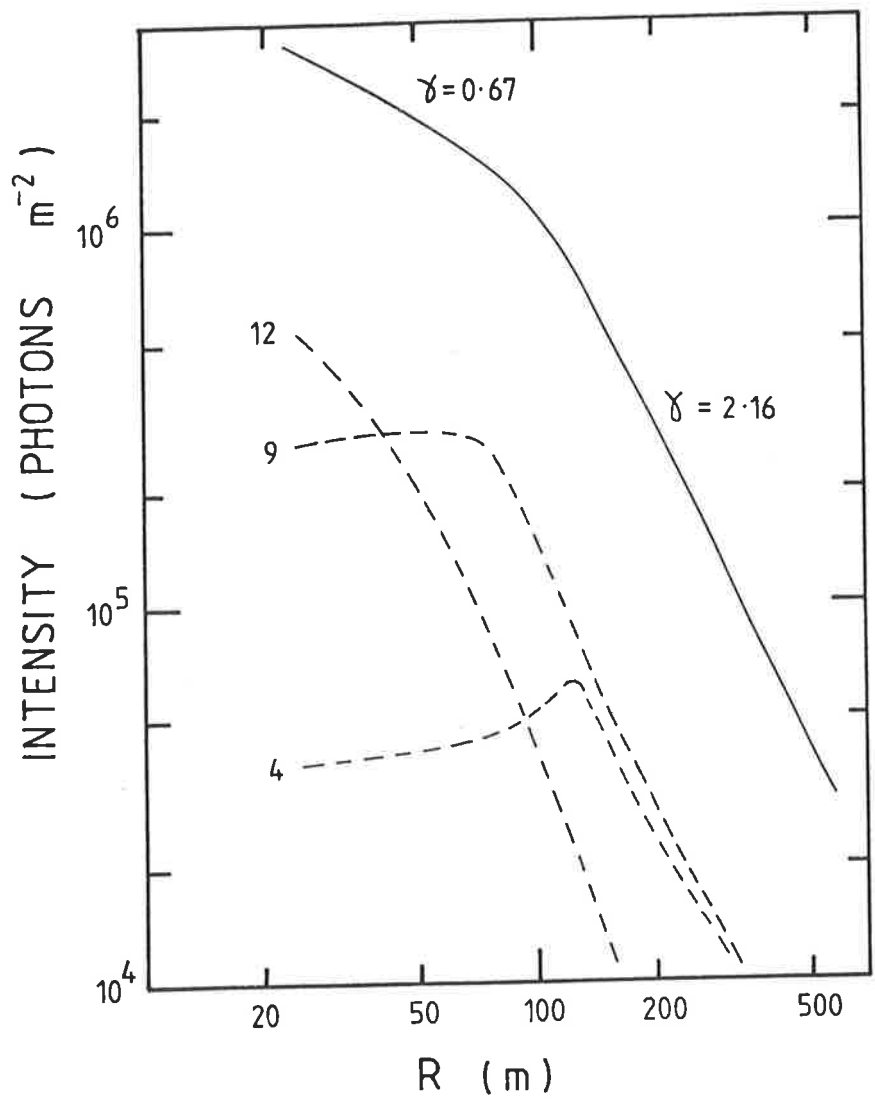


Figure 4.1: Lateral distribution of a simulated 10^{16} eV proton shower at a zenith angle of 15 degrees, $H_m = 4.4$ km (after Patterson and Hillas 1983b). The dashed lines show contributions from three subshowers.

which was injected after shower maximum. The shape of the lateral distribution close to the axis ($<125\text{m}$) is found to be very sensitive to the distance to maximum, H_m . However, the shape near the axis is also found to be sensitive to development fluctuations after shower maximum, which causes some uncertainty in the estimation of DOM by this method. The technique is complementary to the study of the Cerenkov pulse shape, which is sensitive to fluctuations in the early development of showers.

The lateral distribution in figure 4.1 can be fitted with two power laws, one inside 100m and the other outside 200m. While the outer power law is a good fit, the inner one cannot cope with the shoulder which causes a deviation from power law behaviour outside $\sim 50\text{m}$. If the same lateral distribution is plotted on a semilogarithmic plot (figure 4.2) it is seen to follow an approximate exponential form out to $\sim 200\text{m}$. It is an especially good fit between 25m and 125m. In this representation, the change in slope at the shoulder is less marked. Thus the exponential fit is preferred to the power law fit for $r < 125\text{m}$, but Patterson and Hillas warn that the exponential fit ceases to be such a good representation for showers with $H_m > 5\text{km}$. Here the fit is only good over a reduced core distance range. Figure 4.3 shows some other examples of lateral distributions from the work of Patterson and Hillas (Patterson, private communication) with a variety of values of H_m .

Patterson and Hillas prefer the flux ratio $Q(50\text{m})/Q(150\text{m})$ (as used by Tornabene 1979) as a measure of the steepness of the lateral distribution for values of H_m up to

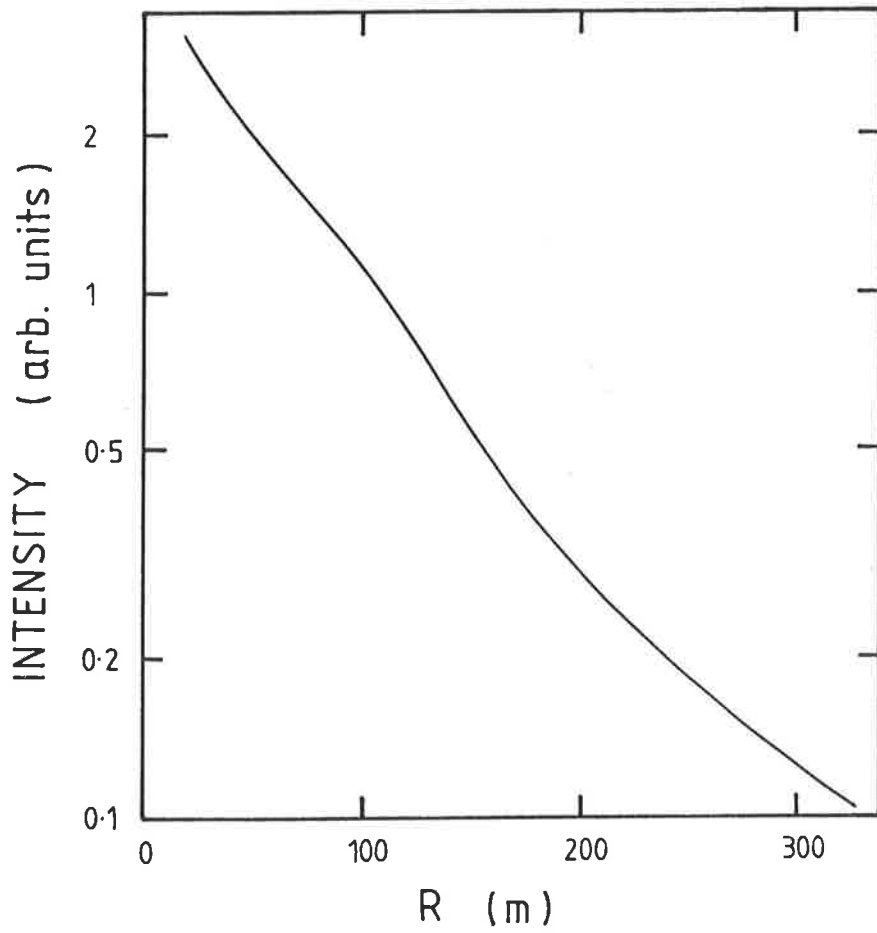


Figure 4.2: The lateral distribution from figure 4.1 plotted on semilogarithmic graph.

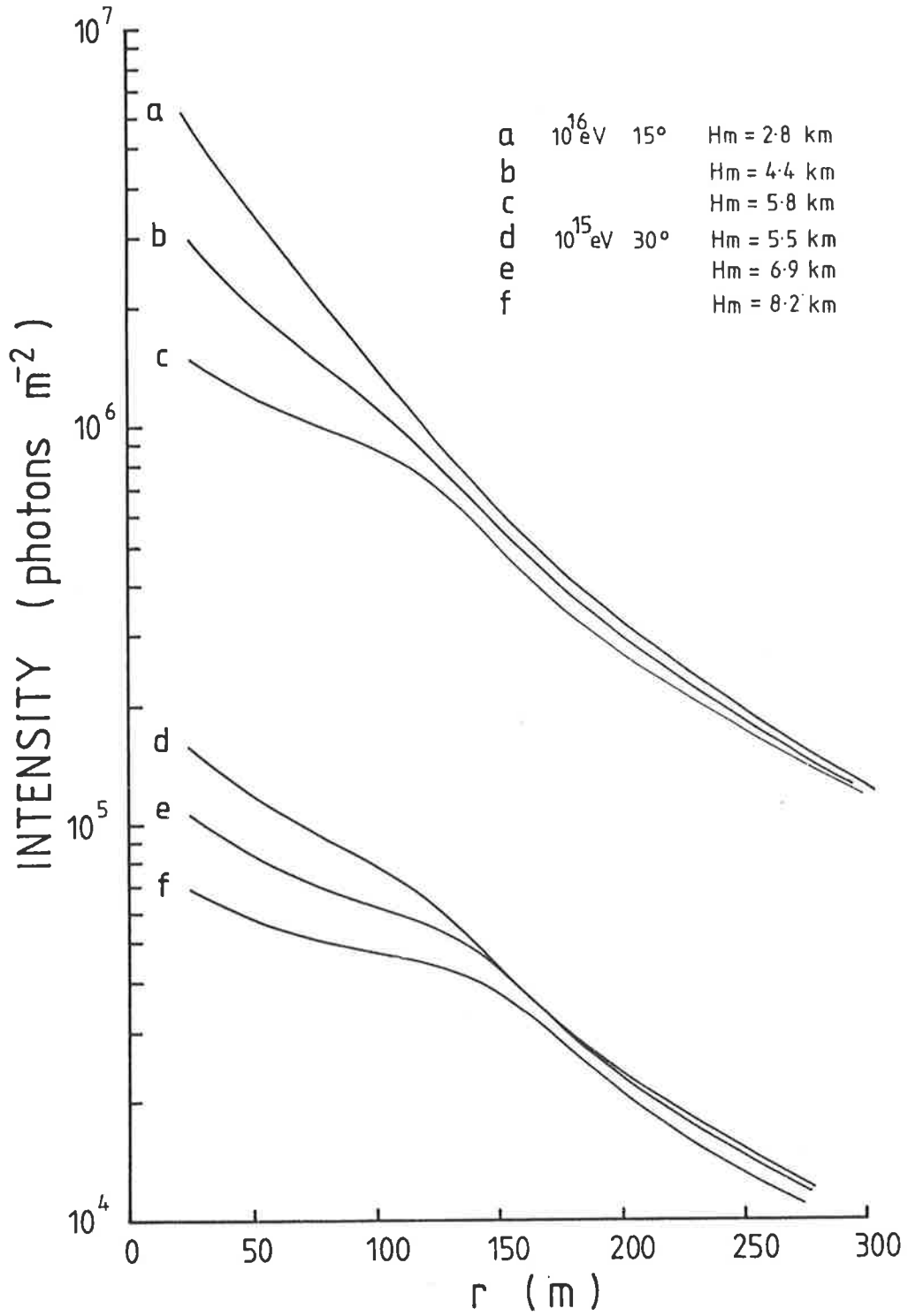


Figure 4.3: Some examples of the calculations of Patterson and Hillas (1983b).

10km. The relationship between this parameter and H_m is shown in figure 4.4 for four zenith angles. Recognising the difficulty of measuring the flux ratio experimentally, Patterson and Hillas have also produced a plot of the relationship between b (fitted in the core distance range 50-125m) and H_m . This is reproduced in figure 4.5.

4.4 Current Work.

The aim of the present work was to investigate the development of extensive air showers with sea level shower sizes above $\sim 10^5$ particles. To do this it was necessary to examine the shape of the lateral distribution in some detail in order to decide on an appropriate and simple measure of its slope, which could be used to determine the distance to shower maximum. The detailed shape was also of interest as a test of recent theoretical work.

In the first section of this discussion, some examples are given of the connection between the shape of the lateral distribution (in particular its steepness) and air shower development. We shall follow this with a more detailed investigation of the shape and we shall propose a simple functional form which is a good fit to the data in the radial region of interest.

In the following sections, a number of distributions derived from the experimental data will be presented. These distributions have been compiled using a number of subsets of the entire data set. In the interests of clarity, we outline three of these subsets here:

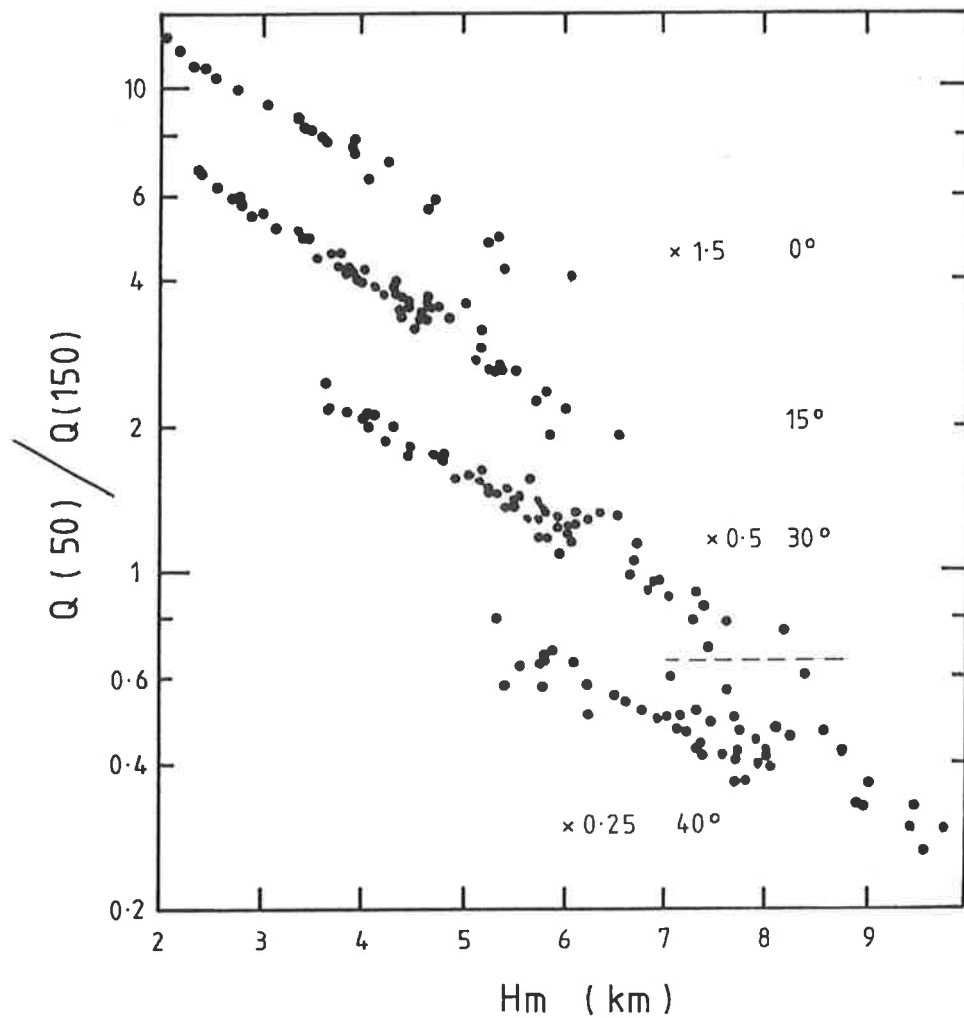


Figure 4.4: The relationship between the Cerenkov flux ratio $Q(50)/Q(150)$ and the distance to maximum, H_m (after Patterson and Hillas 1983b).

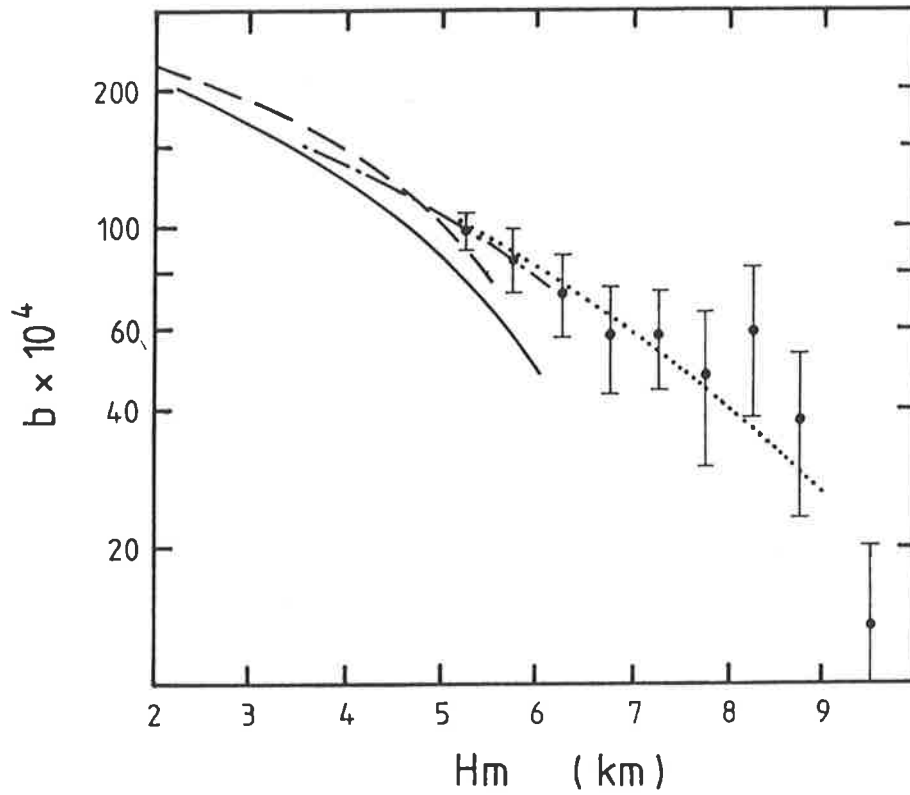


Figure 4.5: The relationship between the Cerenkov slope parameter b and the distance to maximum H_m . Zenith angles represented are 0° (dashed), 15° (full line), 30° (chain) and 40° (dotted).

The points indicate the uncertainty in the 40° curve.

Data Set A: 1286 events.

Particle Data Criteria: > 5 density measurements
 > 2 non-colinear timing
 measurements

NKG function chi-squared $< 2 + 2 \log (N_e / 10^4)$ where
 N_e is the sea level shower size.

Timing chi-squared < 20 (assuming a plane shower front).
 shower zenith angle $< 35^\circ$.

Cerenkov Data Criterion: >5 Cerenkov flux measurements.

Data Set B: 945 events.

Particle Data Criteria: same as Data Set A.

Cerenkov Data Criteria: >5 Cerenkov flux measurements in
 the core distance range 25m-150m with the added
 requirement that there be at least one flux
 measurement between 25m and 75m and at least one
 between 100m and 150m.

Data Set C: 863 events.

Particle Data Criteria: same as Data Set A.

Cerenkov Data Criteria: >5 Cerenkov flux measurements in
 the core distance range 25m-130m with the added
 requirement that there be at least one flux
 measurement between 25m and 75m and at least one
 between 100m and 130m.

Data sets B and C ensure a spread in the Cerenkov measurements
 without (hopefully) introducing any selection bias.

4.4.1 The Lateral Distribution and Shower Development.

A result of the early theoretical work of Zatsepin and Chudakov (1962) was that the fraction of the total Cerenkov flux present in the central region of a shower depends on the fraction of electrons in the shower adjacent to the observation level. As a test of this Kuhlmann and Clay (1981) showed that their lateral distribution normalisation parameter, A (defined in Eq. 4.7), was correlated with the sea level shower size. We have repeated this exercise using data set B. The exponential function was fitted over a reduced radial range, 25-150m (a method discussed in section 4.4.2). The resulting plot of A versus sea level shower size is shown in figure 4.6. The correlation between the two parameters is obvious. The error bars in the figure represent standard deviations and reflect the significant fluctuations in A within the size bins. The size of the fluctuations is not unexpected since showers of a given sea level size are known to be the result of showers of varying primary energy with a broad spread in depth of maximum. Also, it has already been mentioned that Patterson and Hillas (1983b) point out that the shape of the lateral distribution near the core ($r < 150\text{m}$) is especially sensitive to fluctuations in the development of the cascade after shower maximum.

In electromagnetic cascade theory, the slope of the electron lateral distribution is a measure of the stage of the development of the shower. This slope is represented by the age parameter, s (section 2.2.3), which has the value 0 at the beginning of the cascade, is equal to 1 at shower maximum and is equal to 2 at the end of the cascade. Even in real showers

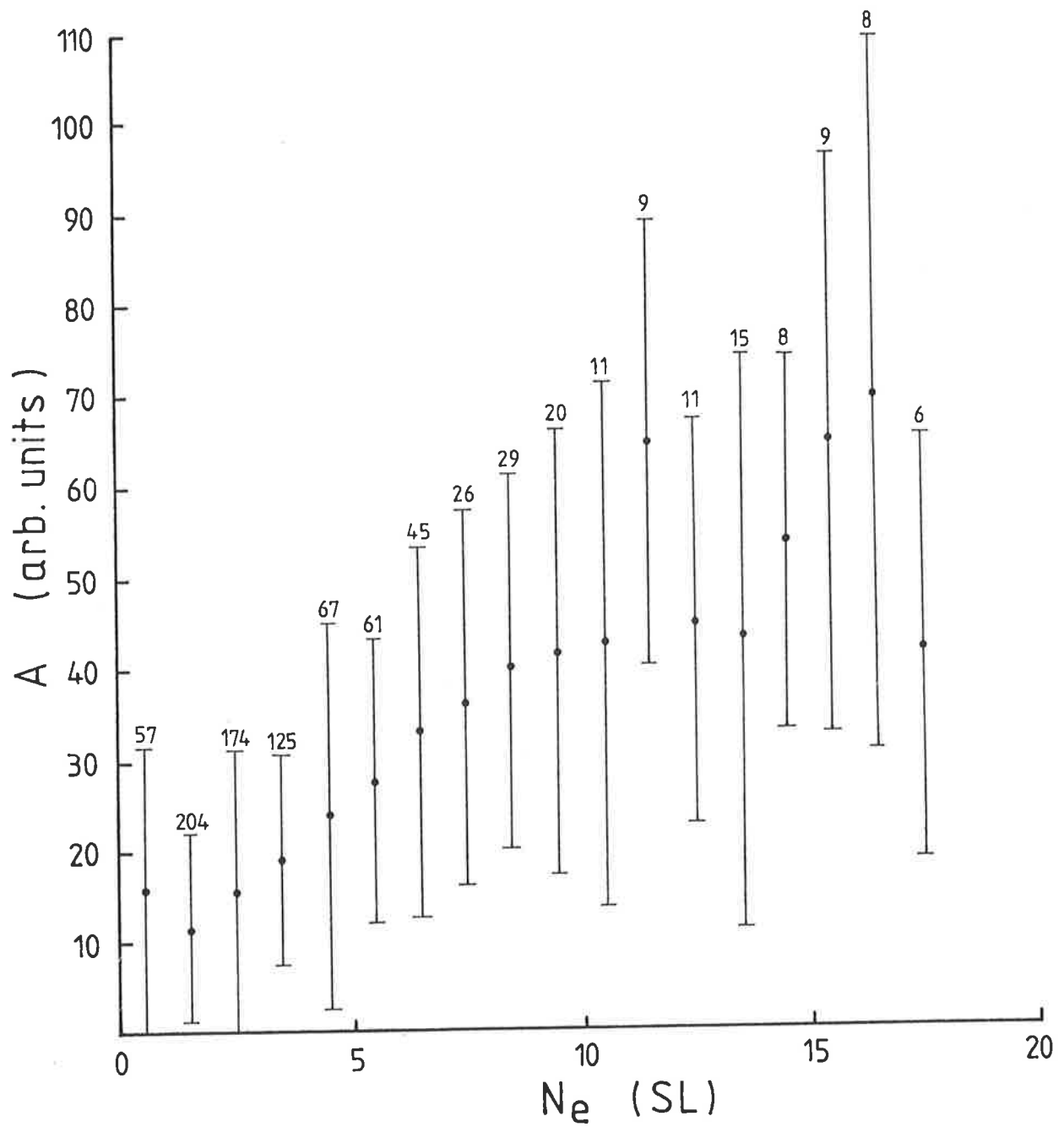


Figure 4.6: The Cerenkov flux on axis as a function of sea level shower size. The error bars represent standard deviations.

it has been found that the age parameter in the NKG lateral distribution function is a monotonically increasing measure of the stage of shower development. Figure 4.7 shows a plot of the electron lateral distribution age parameter s (derived from NKG function fits) versus the Cerenkov lateral distribution slope parameter, b (fitted in the core distance range 25-150m). The 945 events of data set B were used for this figure. The trend is quite clear; "older" (flatter) electron lateral distributions are associated with small b (flatter) Cerenkov lateral distributions. This demonstrates that if the age parameter is indeed a measure of shower development then so is the Cerenkov b parameter.

We shall now consider some average lateral distributions. In the following examples, individual lateral distributions have been added together using 20m wide core distance bins. (In fact, $\log(Q)$ was averaged). Before combining, the individual lateral distributions were normalized so that the flux at 150m, $Q(150) = 100$ (arbitrary units). The quantity $Q(150)$ was calculated on the basis of an exponential fit to each lateral distribution in the core distance range 25-150m. The normalizing radius was chosen to be 150m because the flux at this distance is expected to be a measure of primary energy and to be largely independent of development. The 945 events of data set B were used here. Averages were compiled for five ranges of $N_e(1000)$ (shower size calculated for a depth of 1000gcm^{-2}) in three zenith angle ranges. Some examples are shown in figures 4.8, 4.9, 4.10. As measures of the steepness of the averages, we have fitted exponential functions (using a weighted least squares regression technique)

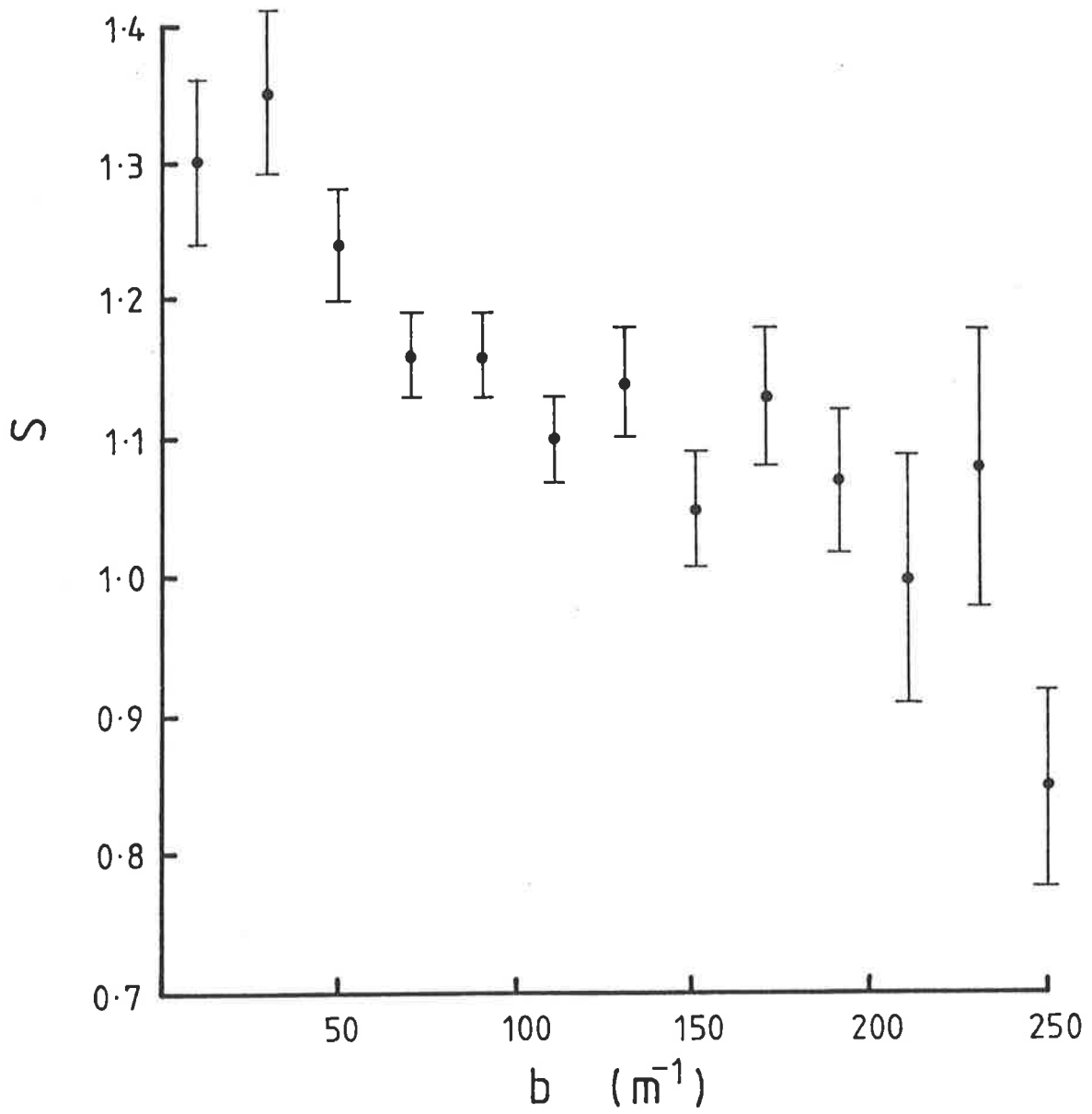


Figure 4.7: The shower age parameter, s , versus the Cerenkov lateral distribution slope parameter, b .

to the distribution over a) the full range of core distances, r , represented and b) a reduced core distances range $30 < r < 150\text{m}$. In table 4.1 we show the results, including the number of events in each average and the slope parameters for the two fits. The trends in the b values indicate a steepening (b larger) of the average lateral distribution with increasing $N_e(1000)$ within a particular zenith angle range. This is interpreted as being a confirmation that the larger $N_e(1000)$ showers develop closer to the observer. Also, it can be seen that the average lateral distribution flattens with increasing zenith angle within a given $N_e(1000)$ range. This is because the distance between the observer and shower maximum increases with increasing zenith angle for showers of the same $N_e(1000)$ (\equiv primary energy). These examples confirm that the measured lateral distributions exhibit the expected connection between the "slope" of the lateral distribution and the distance to shower maximum.

This relationship is explored further in figure 4.11. Here the b slope parameters determined by exponential fits (in the core distance range 25-150m) to individual events in data set B are plotted as a function of $N_e(1000)$ for $\theta < 10^\circ$ (figure 4.11a) and $20^\circ < \theta < 30^\circ$ (figure 4.11b). Apart from the obvious trend towards large b (steep lateral distributions) for large showers, there is also a similar trend towards large b for the smallest showers (especially in fig 4.11b). The latter effect, which is an indication that the smaller showers observed developed close to the observation level, is believed to be a result of particle array selection biases. This effect will be investigated fully in Chapter

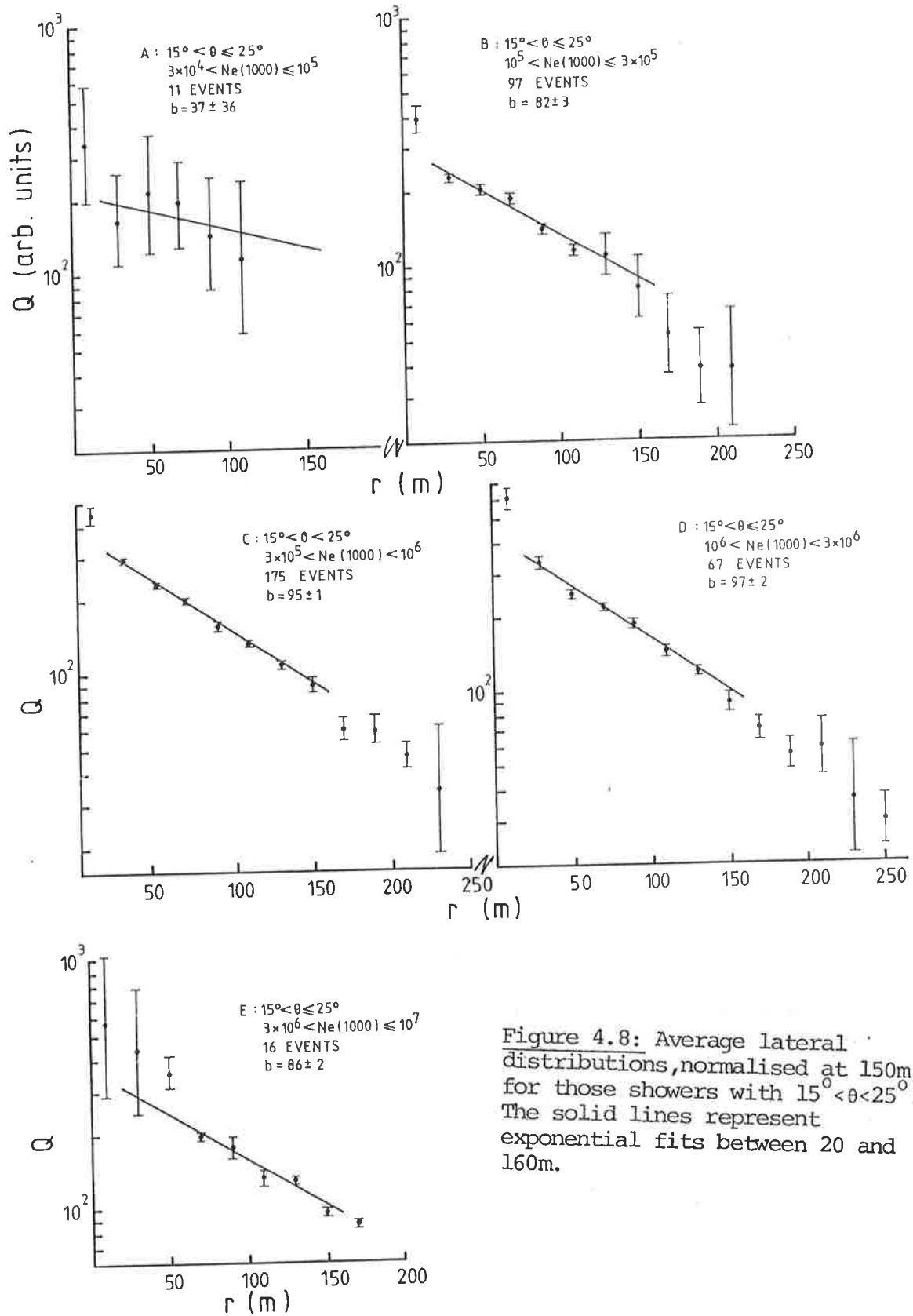


Figure 4.8: Average lateral distributions, normalised at 150m, for those showers with $15^\circ < \theta < 25^\circ$. The solid lines represent exponential fits between 20 and 160m.

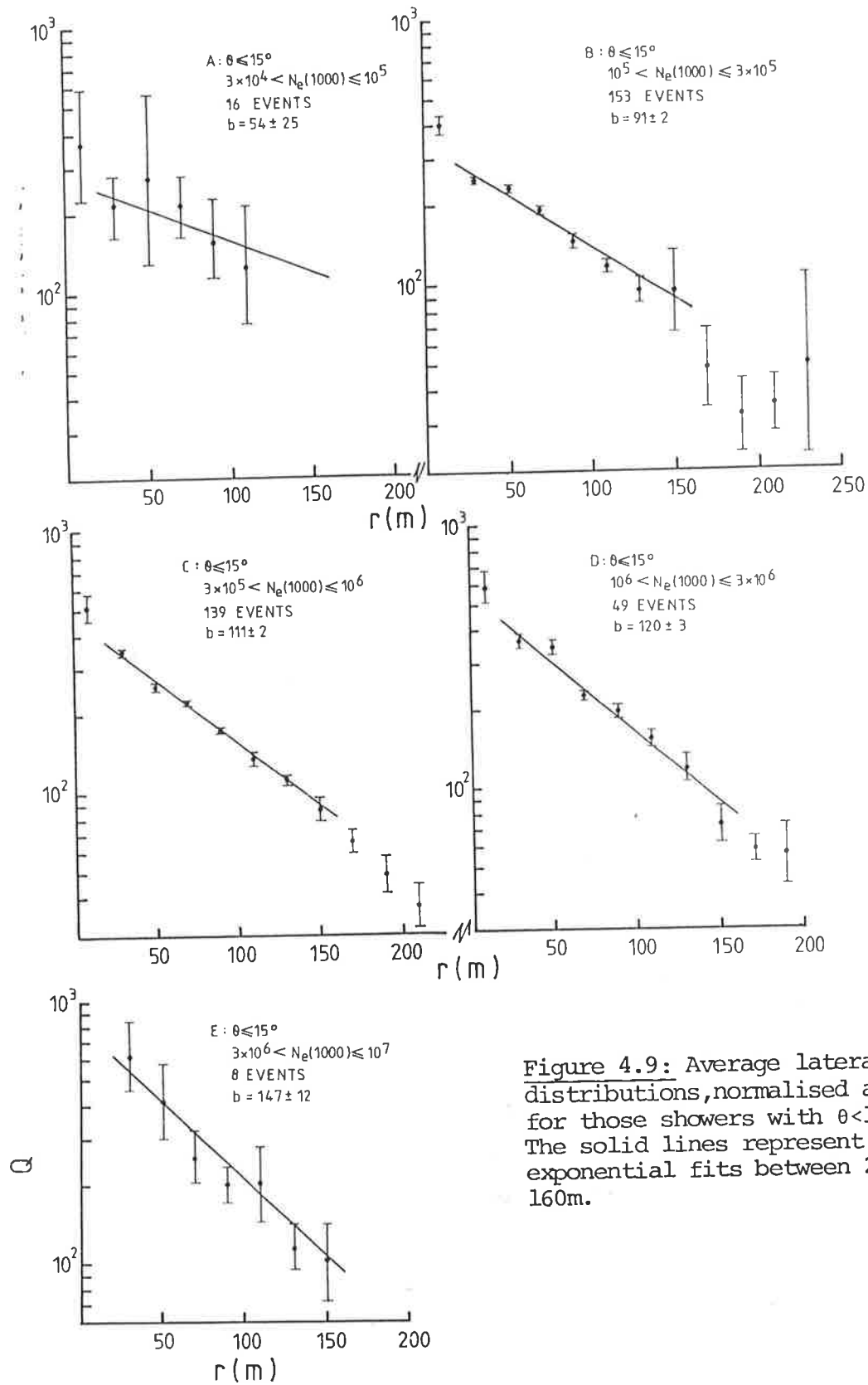


Figure 4.9: Average lateral distributions, normalised at 150m, for those showers with $\theta < 15^\circ$. The solid lines represent exponential fits between 20 and 160m.

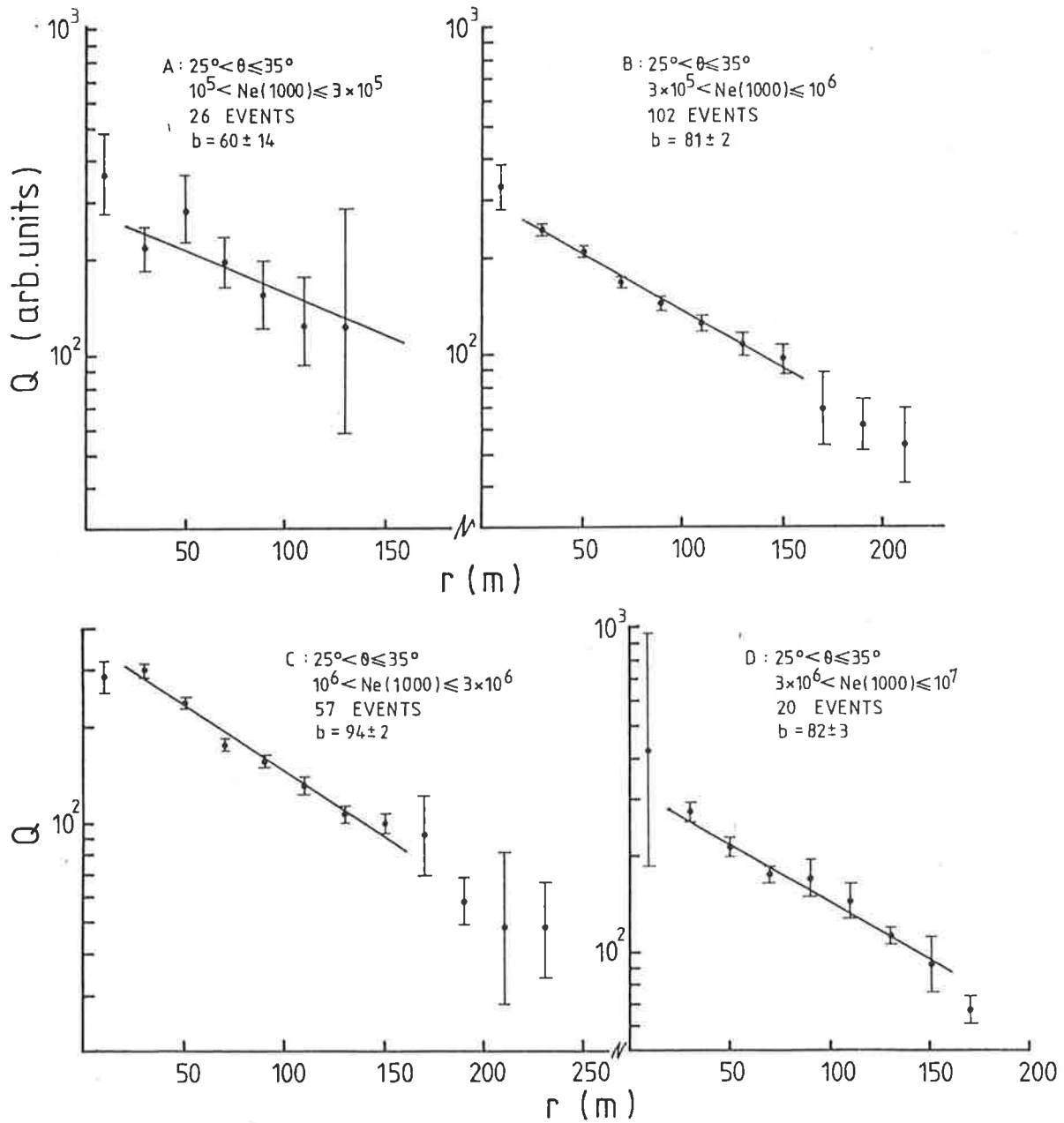


Figure 4.10: Average lateral distributions normalised at 150m, for those showers with $25^\circ < \theta \leq 35^\circ$. The solid line represents an exponential fit between 20 and 160m.

	$0 < \theta < 15^\circ$	$15^\circ < \theta < 25^\circ$	$25^\circ < \theta < 35^\circ$
$3 \times 10^4 < N_e < 10^5$	n=16 b=71±21 b'=54±25	11 71±29 37±36	-
$10^5 < N_e < 3 \times 10^5$	n=153 b=99±2 b'=91±2	97 91±3 82±3	26 74±12 60±14
$3 \times 10^5 < N_e < 10^6$	n=139 b=114±1 b'=111±2	175 99±1 95±1	102 82±2 81±2
$10^6 < N_e < 3 \times 10^6$	n=49 b=128±3 b'=120±3	69 107±2 97±2	57 92±2 94±2
$3 \times 10^6 < N_e < 10^7$	n=8 b=147±12 b'=147±12	16 87±1 86±2	20 91±2 82±3

Table 4.1: Results from average lateral distributions. Here n is the number of events in each average, b is the slope parameter derived using all data and b' is the slope parameter derived from the data with $30 < r < 150$ m.

Five. For the moment we shall disregard the data below $N_e(1000) = 1.6 \times 10^5$ particles in figure 4.11a and those below $N_e(1000) = 4.0 \times 10^5$ particles in figure 4.11b. The remaining data are represented by weighted lines of best fit in figure 4.11c. Here we see a summary of the familiar trends - an increase in steepness of the lateral distribution with increasing shower size and decreasing zenith angle. (The two lines in figure 4.11c should be parallel if b is a measure of the distance to maximum irrespective of shower zenith angle. While the lines of best fit are not parallel, the results of the weighted regression analysis show that the data are consistent with a hypothesis that the lines are parallel). Given these curves it is possible to extract a rough measure of the elongation rate.

Recall from section 2.3 that the elongation rate is the rate of change of depth of shower maximum (X_m) per decade of primary energy (or, shower size).

From the $\theta < 10^\circ$ curve we have

$$\frac{\Delta b}{\Delta \log N_e(1000)} = 27 \text{ m}^{-1} / \text{decade} \quad \text{Eq. 4.8}$$

The difference in average $\sec\theta$ between the two curves is $\overline{\Delta \sec\theta} = 1.10 - 1.01 = 0.09$. At a shower size of 10^6 we can write

$$\frac{\Delta b}{\Delta \sec\theta} = \frac{16}{0.09} \text{ m}^{-1} \quad \text{Eq. 4.9}$$

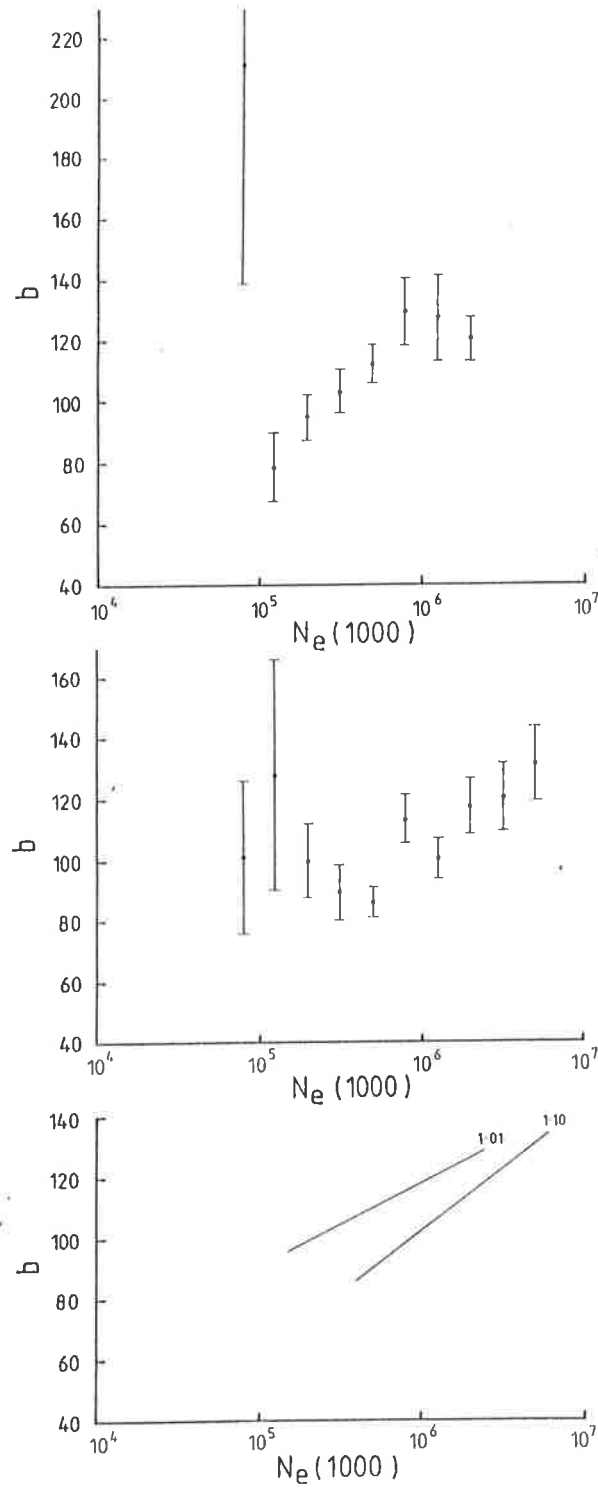


Figure 4.11: a: Cerenkov slope parameter, b versus shower size at 1000gcm^{-2} for $\theta < 10^\circ$
 b: As above, but for $20^\circ < \theta < 30^\circ$
 c: Lines of best fit for a and b (see text).
 The mean values of $\sec\theta$ are given

Assuming that the average change in depth of shower maximum between the two curves depends only on zenith angle effects,

$$\Delta X_m = 1000 \overline{\Delta \sec \theta} \text{ gcm}^{-2} \quad \text{Eq. 4.10}$$

and so at $N_e(1000) = 10^6$,

$$\frac{\Delta b}{\Delta X_m} = \frac{16}{90} \text{ m}^{-1} / \text{gcm}^{-2} \quad \text{Eq. 4.11}$$

Dividing Eq. 4.11 by Eq. 4.8 we get

$$\frac{\Delta X_m}{\Delta \log N_e(1000)} = 27 \cdot \frac{90}{16} = 150 \text{ gcm}^{-2} / \text{decade of shower size}$$

While this example has illustrated how information about development can be gained from the lateral distribution, it is nonetheless crude. The figure of 150 gcm^{-2} /decade of shower size is much higher than the figure expected for the energy elongation rate for a constant cosmic ray composition and conventional particle physics, $67 \pm 10 \text{ gcm}^{-2}$ / decade (section 2.3). A more detailed examination of the question of composition is made in Chapter 5.

4.4.2 The Shape of the Lateral Distribution.

In this section we present results of an investigation into the shape of the lateral distribution. A

number of comparisons with the recent theoretical work of Patterson and Hillas (1983b) (hereafter designated by P & H) will be made. Recall from section 4.3 that P & H predict that the lateral distribution can be well represented by simple exponentials in the core distance range $\sim 25-130\text{m}$ provided that the shower maximises closer than $\sim 5\text{km}$. For showers developing further away, the radial range over which an exponential is a good fit is reduced. The calculations show that a well fitted exponential in the core distance range $25-130\text{m}$ will, in general, underestimate the flux at distances $r > 200\text{m}$ if $H_m \lesssim 4\text{km}$. Similarly it will underestimate the flux for $r < 25\text{m}$ and overestimate it for $r > 200\text{m}$ if the shower develops with $H_m \gtrsim 4\text{km}$ (see again the examples in figure 4.3).

An examination has been made of the present data set and it has been found that the majority of the data are well fitted (within experimental errors) by exponential functions of the familiar form

$$Q(r) = Ae^{-br/10^4} \quad \text{Eq. 4.12}$$

in the core distance range $25\text{m} - 150\text{m}$. Given this fit it is possible to extract P & H's preferred measure of the slope of the lateral distribution, the flux ratio $Q(50)/Q(150)$. The relationship between this parameter and the distance to shower maximum, H_m is well defined by P & H (figure 4.4). However there is some evidence in the experimental distributions of departures from an exponential form near 150m for those showers with "flat" lateral distributions inside 130m (an effect predicted by P & H). In these cases, the use of an exponential

fit in the range 25-150m to estimate $Q(150)$ would result in an overestimate of this flux. This would lead to an underestimate of the flux ratio and an overestimate of the distance to maximum, H_m . The alternative procedure is to fit exponentials in the smaller radial range 25-130m and then relate the slope parameter b directly to the distance to maximum through the (less precise) relationships given by P & H (figure 4.5). In this section we include a discussion of the suitability of, and the differences between, the two approaches.

We have examined data set B and have selected those showers with $N_e(1000) > 10^6$ particles and a Cerenkov flux measurement further than 150m from the shower axis. Showers of this size were chosen to ensure that the Cerenkov flux measurements were well above sky noise. An exponential function was fitted to the Cerenkov data for each event in the core distance range 25-150m. The flux ratio $Q(50)/Q(150)$ was calculated on the basis of this fit, and a distance to maximum, H_m , was calculated for each event. The relationships between the flux ratio and H_m have been derived from the plot of P & H (fig. 4.4), and are

$$\begin{aligned} \text{for } \theta < 10^\circ, & \quad H_m = - 8.0 \log \left(\frac{Q(50)}{Q(150)} \right) + 9.4 \text{ km} \\ 10^\circ < \theta < 20^\circ & \quad H_m = - 7.7 \log \left(\frac{Q(50)}{Q(150)} \right) + 8.7 \text{ km} \quad \text{Eq. 4.13} \\ 20^\circ < \theta < 35^\circ & \quad H_m = - 8.3 \log \left(\frac{Q(50)}{Q(150)} \right) + 9.3 \text{ km} . \end{aligned}$$

Of the showers analysed in this way, 58 had deduced distances to maximum less than 5km and 29 had deduced distances

to maximum greater than 6km. We have selected six events from each of these groups as examples to compare their features. Figure 4.12 shows the examples from the group with $H_m < 5\text{km}$. It can be seen that the exponential function is a good fit to the data in the radial range over which it was fitted (25-150m) and that in all cases the fit provides a good estimate of the flux ratio $Q(50)/Q(150)$. This was true for every one of the 58 events in the data set. Note that there is some evidence in these examples of the lateral distribution shape predicted by P & H - for example, the exponential function fitted in the range 25-150m underestimates the flux at $r \gtrsim 200\text{m}$ for showers with $H_m < 4\text{km}$.

Consider now figure 4.13, showing some examples of showers which have been assigned $H_m > 6\text{km}$ on the basis of the exponential fit for $25 < r < 150\text{m}$. In the majority of cases, the exponential is again a good fit to the data in this core distance range. However, in some of these flatter lateral distributions there is evidence for a departure from the exponential outside 130m. In these cases, the flux at 150m from the axis is overestimated by fit. This results in an overestimation of H_m . Of the 29 events in this set, 6 appeared to have exponential fits which overestimated $Q(150)$. In five of those cases the overestimation was minimal. The sixth event is shown as one of the examples (fig. 4.13e). The fit produced an estimate of $H_m = 7.2\text{km}$ (depth of maximum = 410gcm^{-2}). However if we take the data point at 155m as an estimate of $Q(150)$ and take $Q(50)$ from the exponential fit, we obtain $H_m = 5.2\text{km}$ (depth of maximum = 530gcm^{-2}). These are the extreme figures, and it is likely that the true figure lies

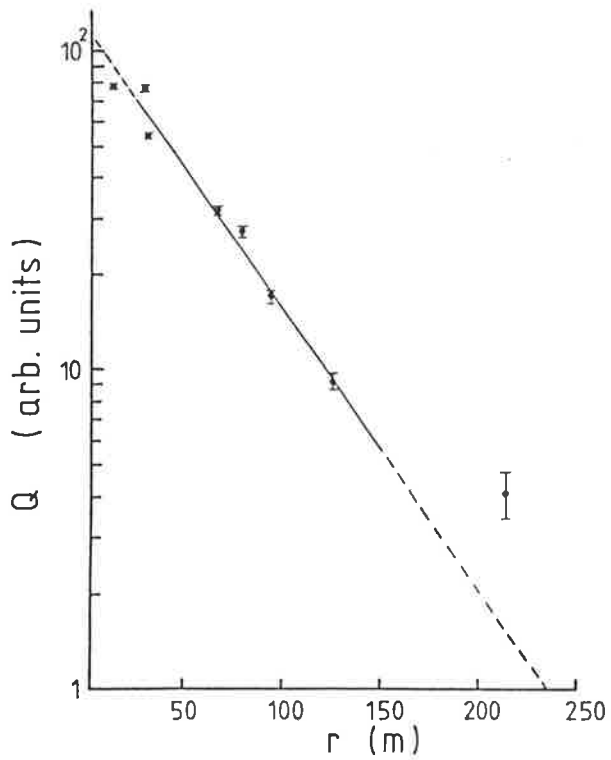
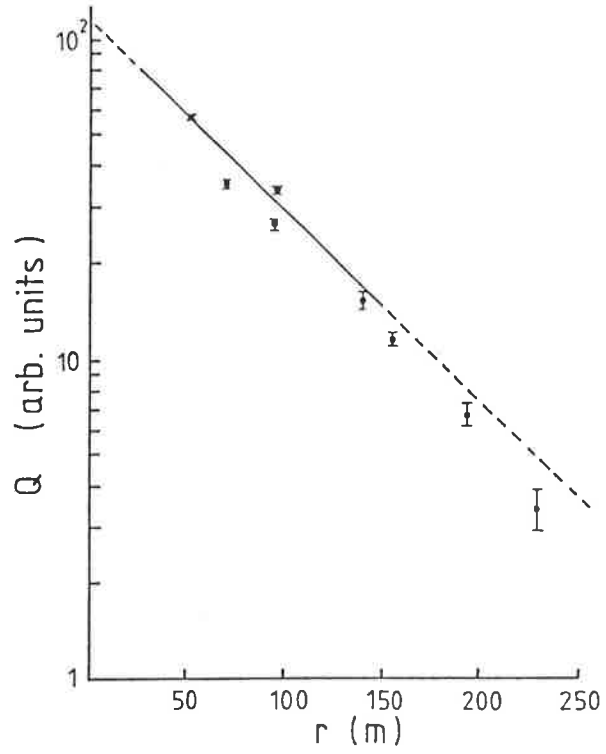


Figure 4.12(a,b): Examples of individual lateral distributions with inferred values of H_m less than 5km.

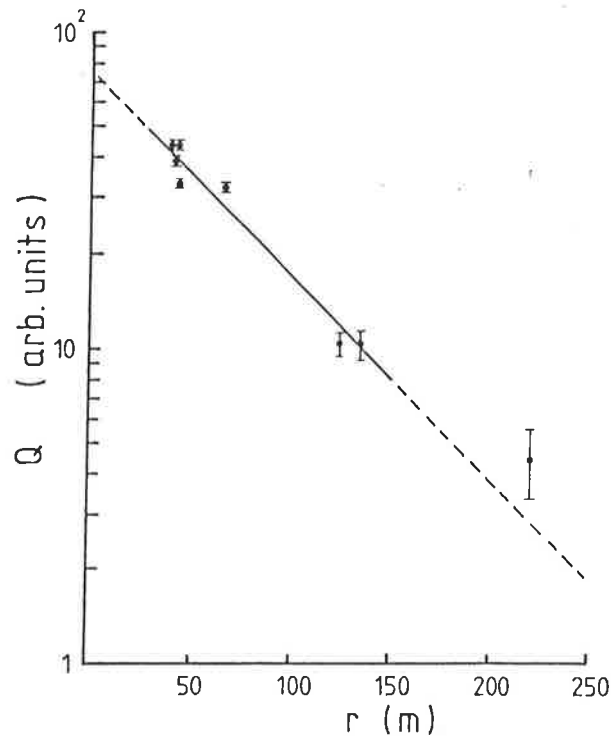
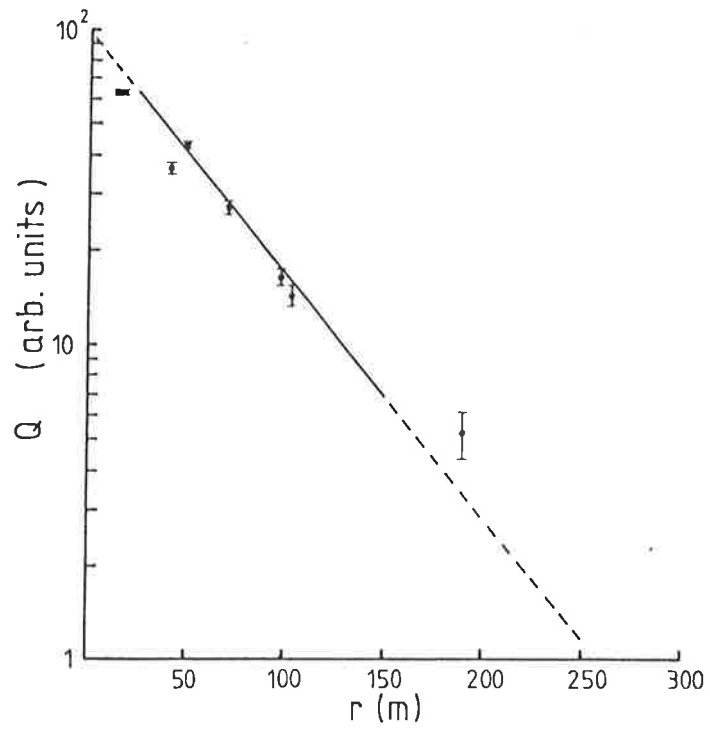


Figure 4.12(c,d): $H_m < 5\text{km}$.

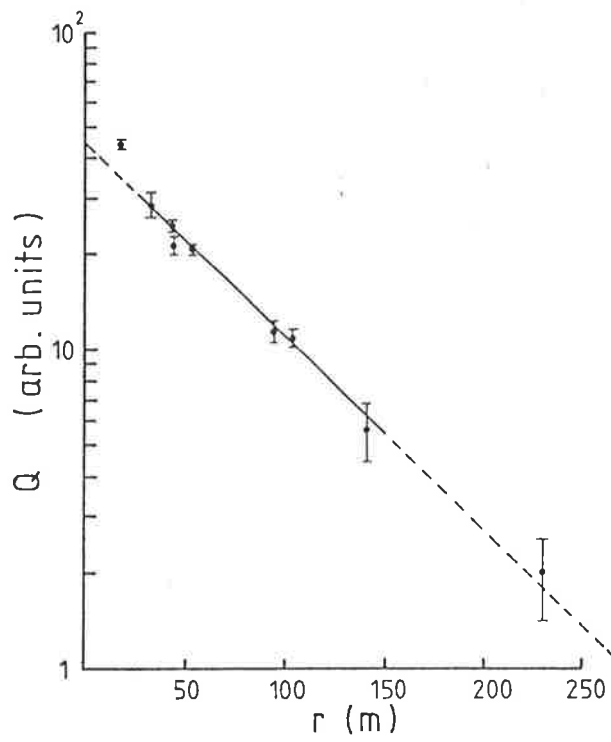
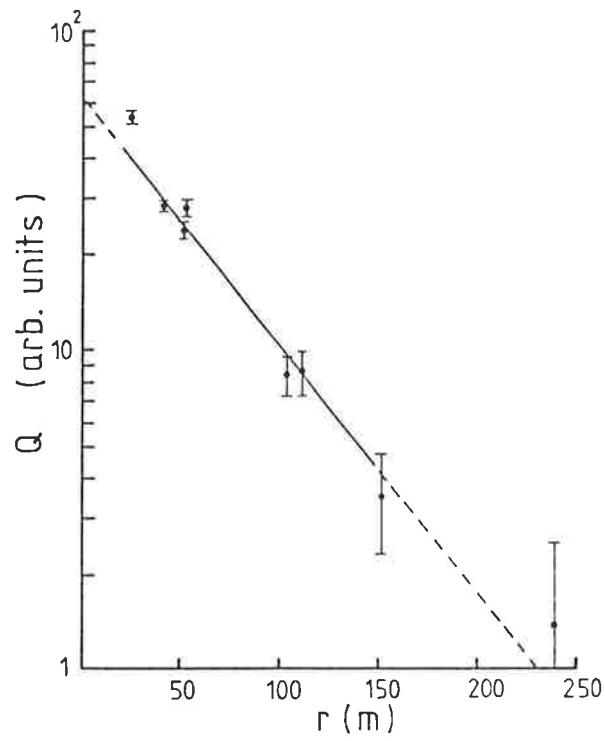


Figure 4.12(e,f): $H_m < 5\text{km}$.

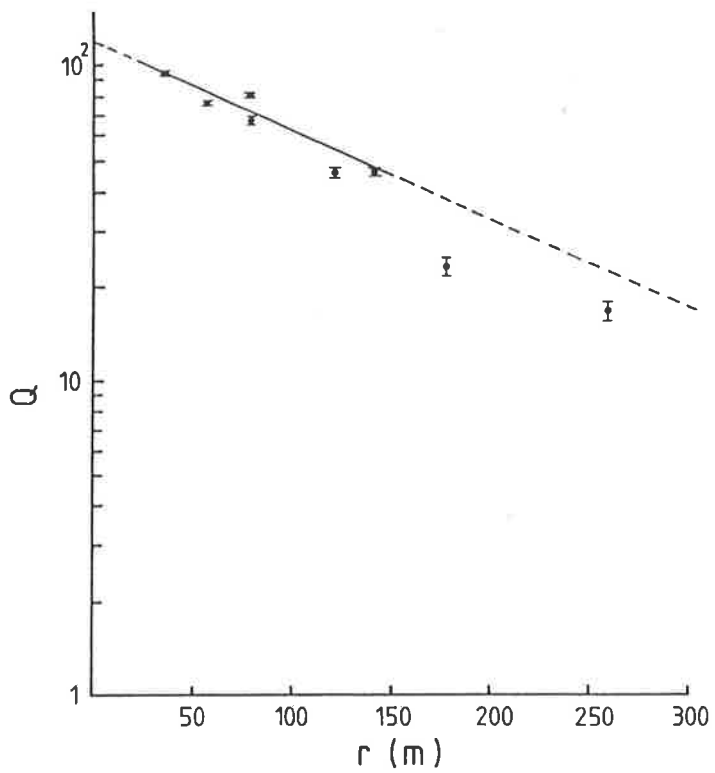
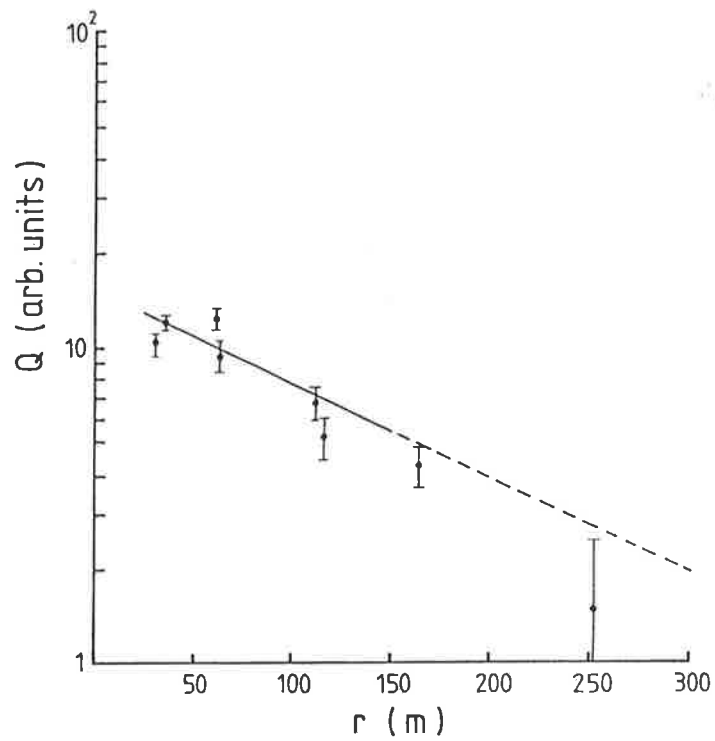


Figure 4.13(a,b): Examples of individual lateral distributions with inferred values of H_m greater than 6km.

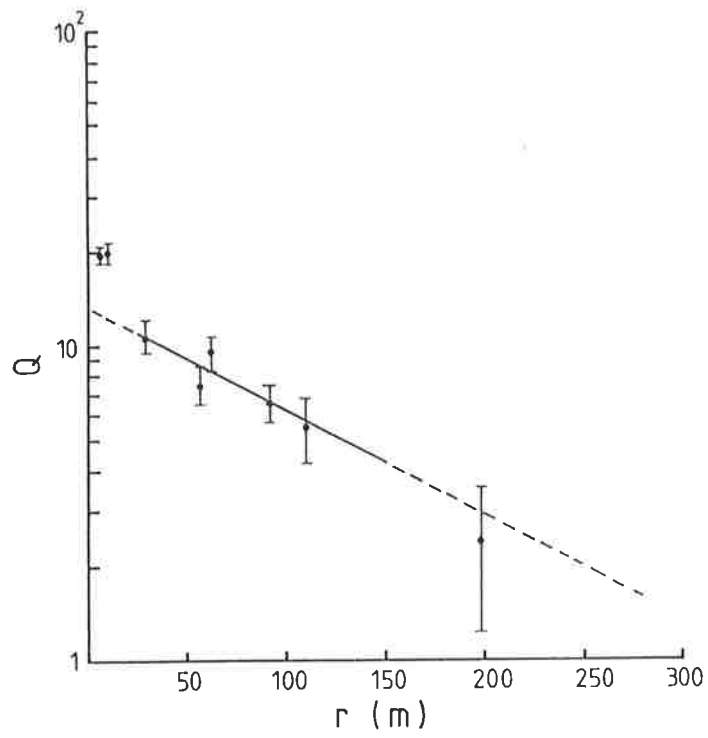
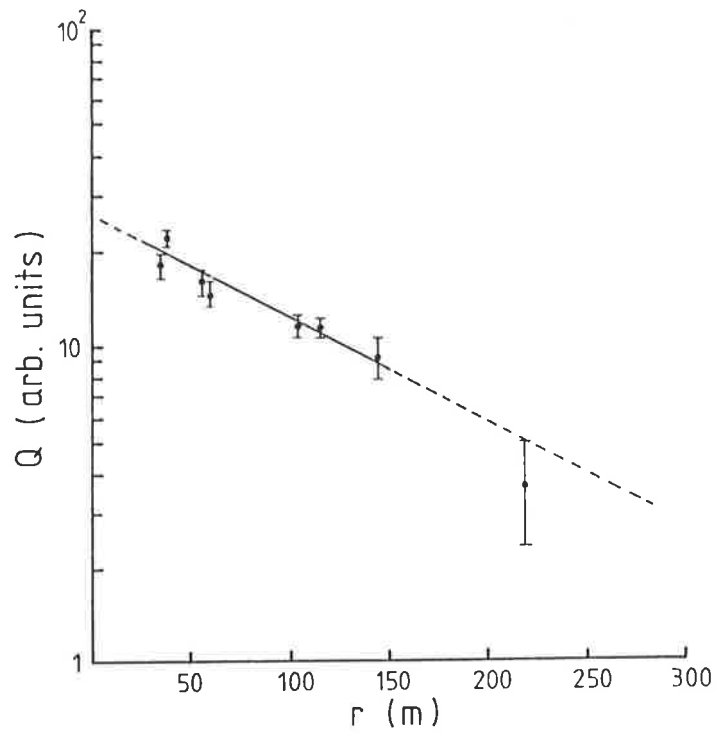


Figure 4.13(c,d): $H_m > 6\text{km}$.

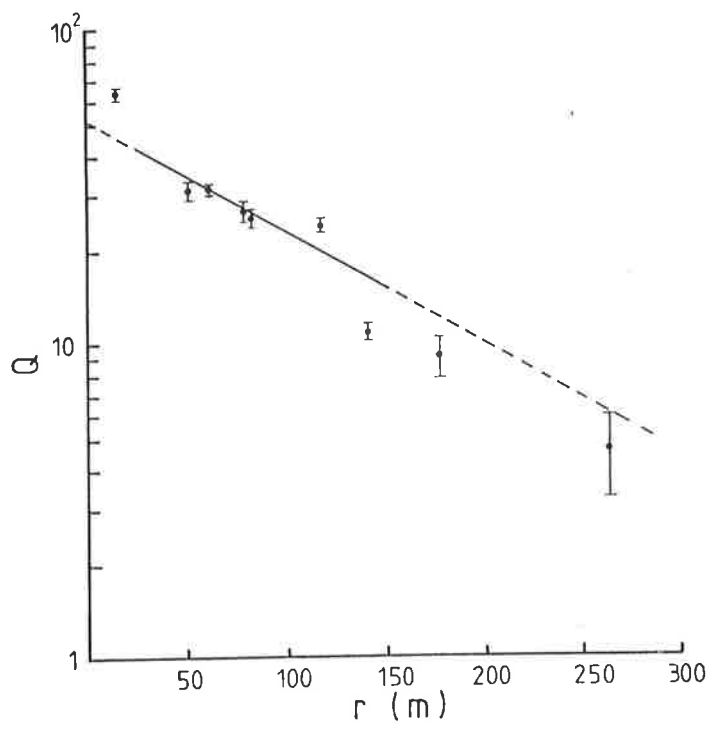
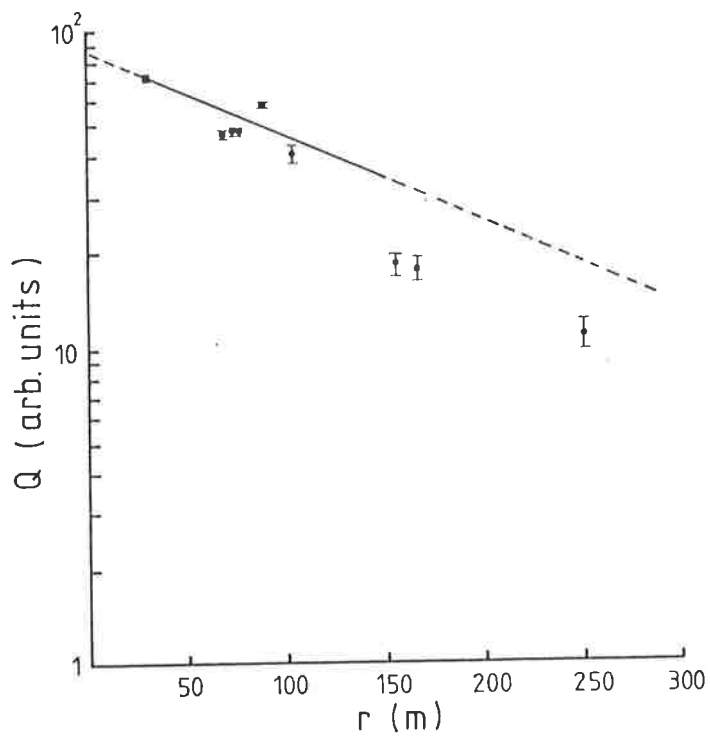


Figure 4.13(e,f): $H_m > 6$ km.

somewhere in between. However the example does highlight the problem of the overestimation of H_m on the assumption that an exponential function is a good fit to the data out to a core distance of 150m. While this assumption is a correct one in the majority of cases, a problem does arise for a small number of "flat" lateral distributions.

In this discussion it is worthwhile to re-examine the average lateral distributions described in the previous section (figures 4.8, 4.9, 4.10). Exponential functions were fitted to the averages (which were compiled on the basis of shower size and zenith angle) in the core distance range 20-160m and are shown in the figures. It can be seen that in these average lateral distributions the exponential is a simple function which represents the data well, and that it provides a good estimate of the flux ratio required for the determination of H_m .

The showers which contributed to these averages have been individually fitted with exponential functions in the core distance range 25-150m. Using these fits a flux ratio and a distance to maximum, H_m , have been calculated for each event. It has therefore been possible to assign a mean value of H_m (with a standard deviation) to each of the average lateral distributions. A few examples of these lateral distributions have been reproduced in figure 4.14, with mean values of H_m as shown. In each figure we have overlaid (with arbitrary normalization) an example of a lateral distribution from the work of Patterson and Hillas (Patterson, private communication) with a comparable distance to maximum. It can be seen that the agreement between the theory and experiment is

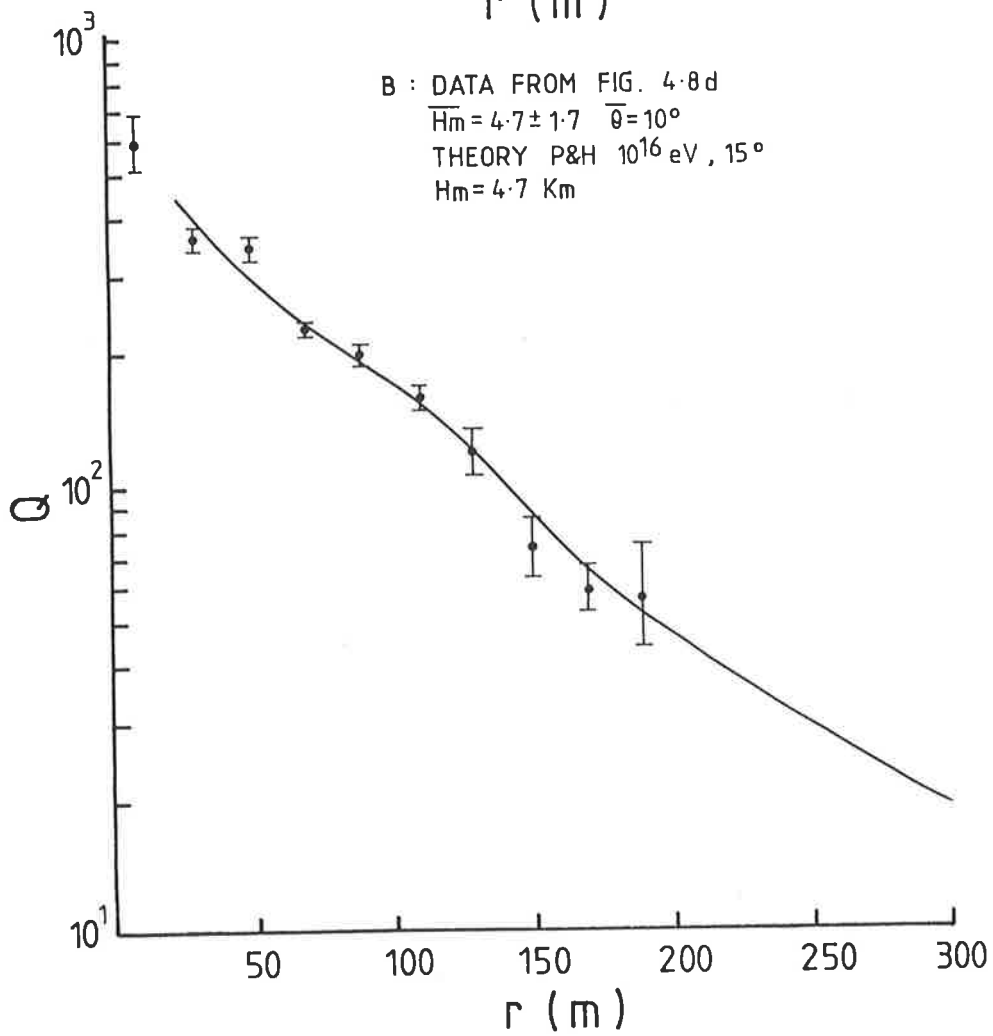
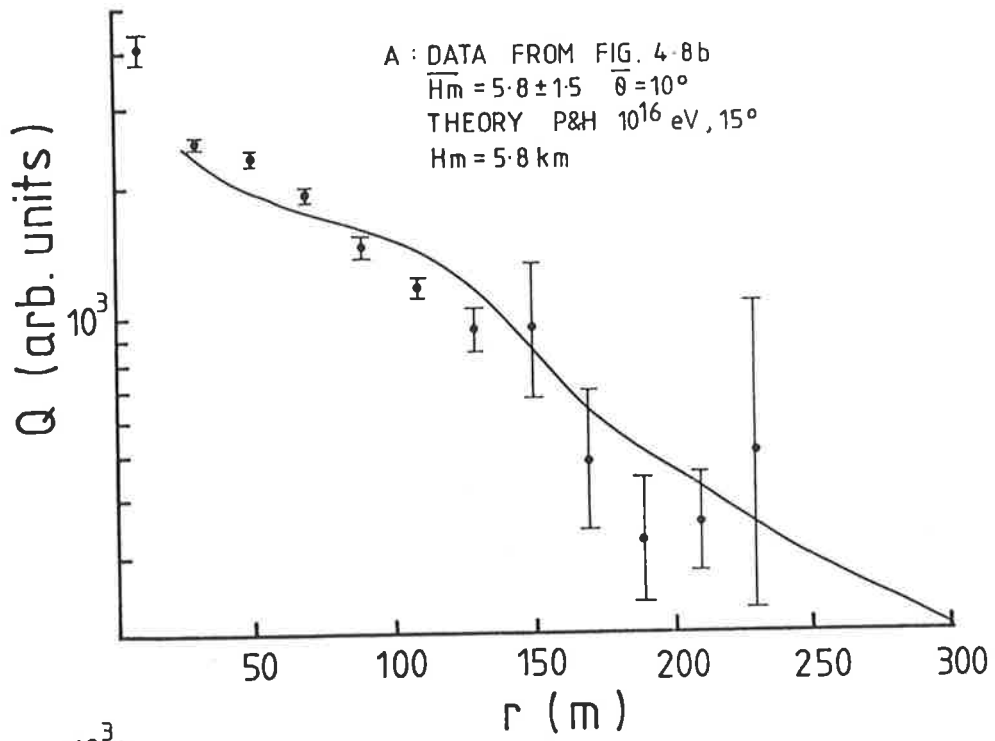


Figure 4.14(a,b): Comparison of average lateral distributions with the calculations of P&H.

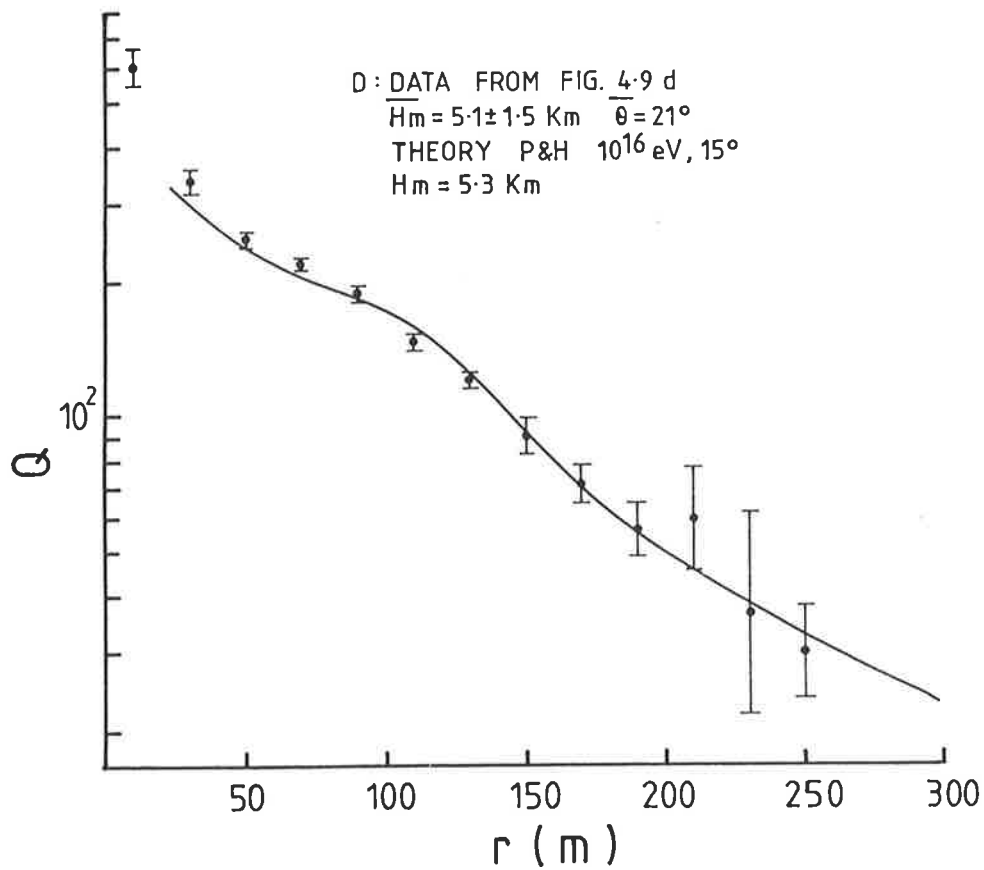
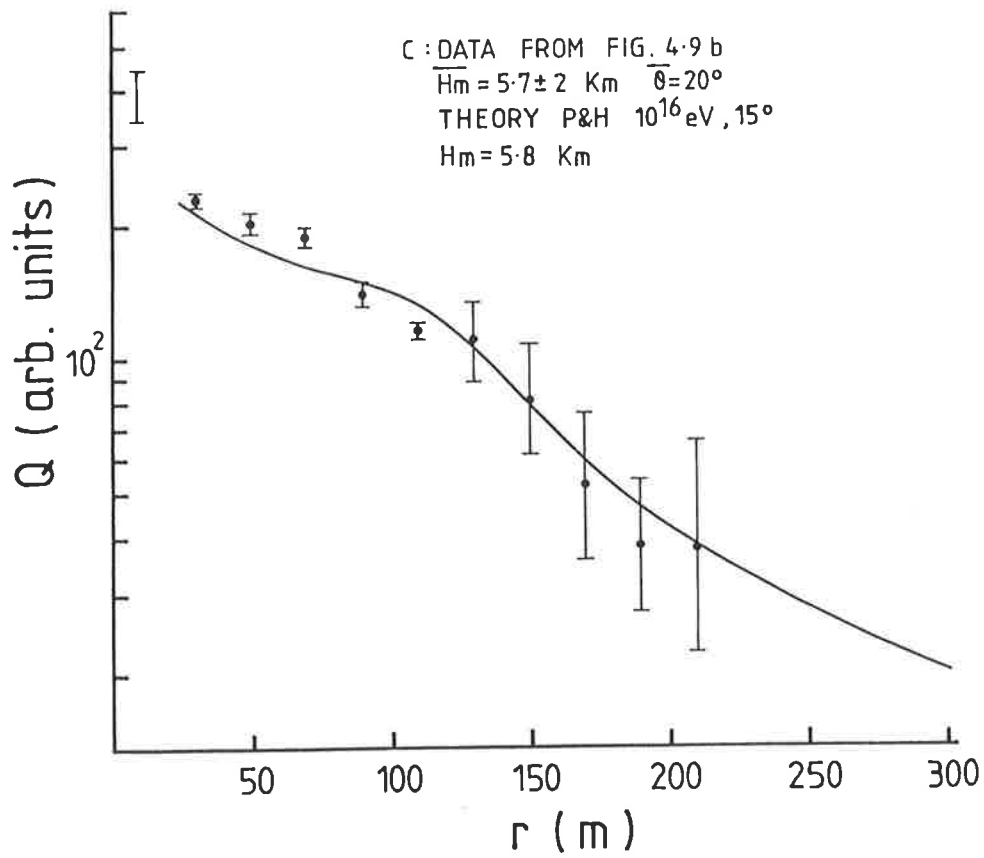


Figure 4.14(c,d): Comparison of average lateral distributions with the calculations of P&H.

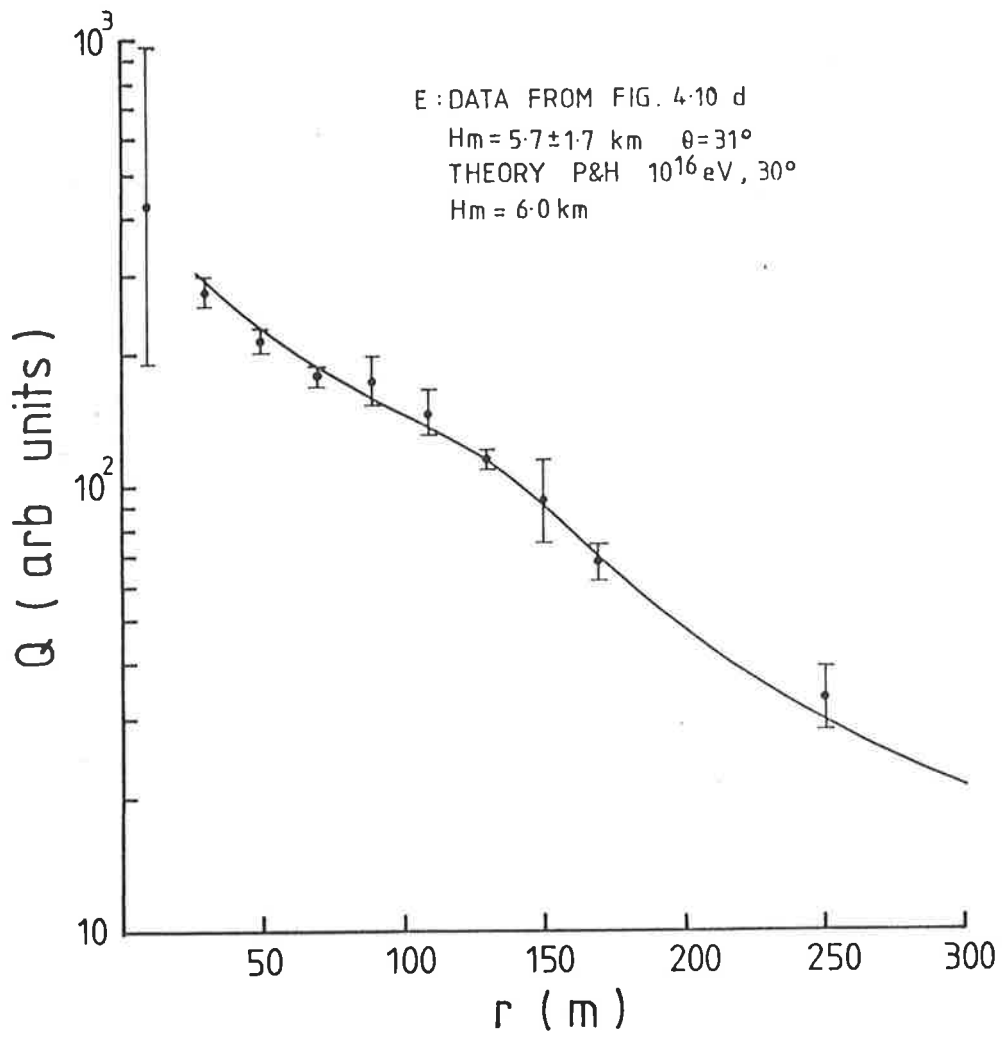


Figure 4.14e: Comparison of an average lateral distribution with the calculations of P&H.

satisfactory, given that the theoretical lateral distribution in each case is that of a single shower (not an average) and given that the experimental averages contain showers over a range of H_m .

The events from data set B have been used to produce another set of average lateral distributions (fig. 4.15). Here we have not averaged lateral distributions on the basis of shower size or zenith angle, but rather in terms of the distance to maximum, H_m , determined in the analysis of each event. (H_m was determined again from the flux ratio inferred from an exponential fit to the data in the core distance range 25-150m). Thus fig. 4.15a includes all showers with a H_m between 2 and 4km, 4.15b includes all showers with a H_m between 4 and 6km etc. The means and standard deviations of the distances to maximum included in each average lateral distribution are shown in the figures. Of interest here is not the shape between 25m and 150m (which was used to select the showers for each average) but rather the shape inside 25m and outside 150m. We have again overlaid examples of the calculations of Patterson and Hillas (Patterson, private communication) for comparison. The distances to maximum for the theoretical curves are shown. The agreement here is considered good. The features of the shape outside 150m and inside 25m expected on the basis of the calculations are evident in the experimental distributions.

It has been pointed out earlier in this section that while the exponential fit in the core distance range 25-150m is a convenient and accurate method of determining the flux ratio $Q(50)/Q(150)$ in the majority of cases, a problem of

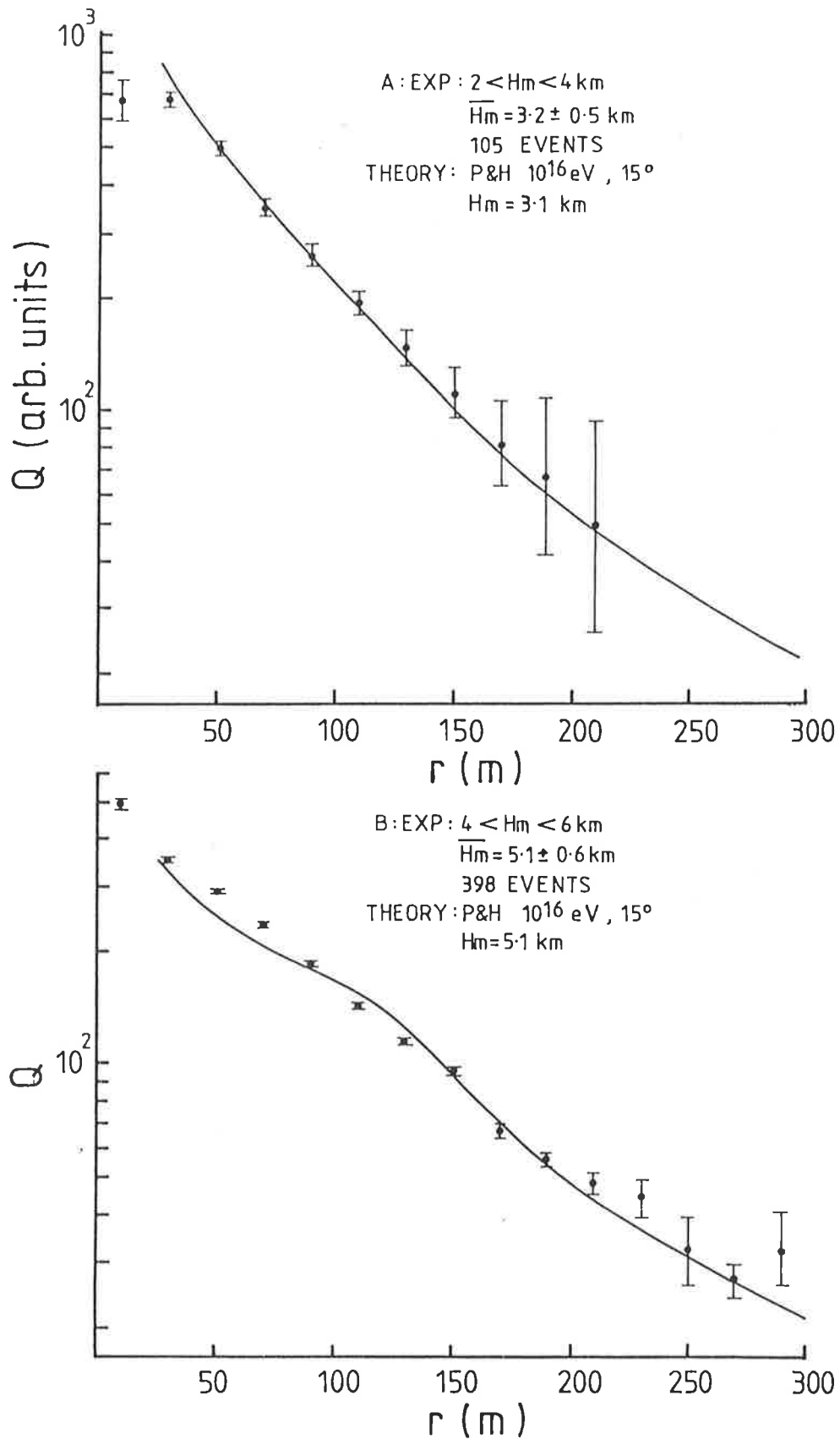


Figure 4.15(a,b): Comparison of lateral distributions, averaged in terms of H_m , with calculations of Patterson and Hillas.

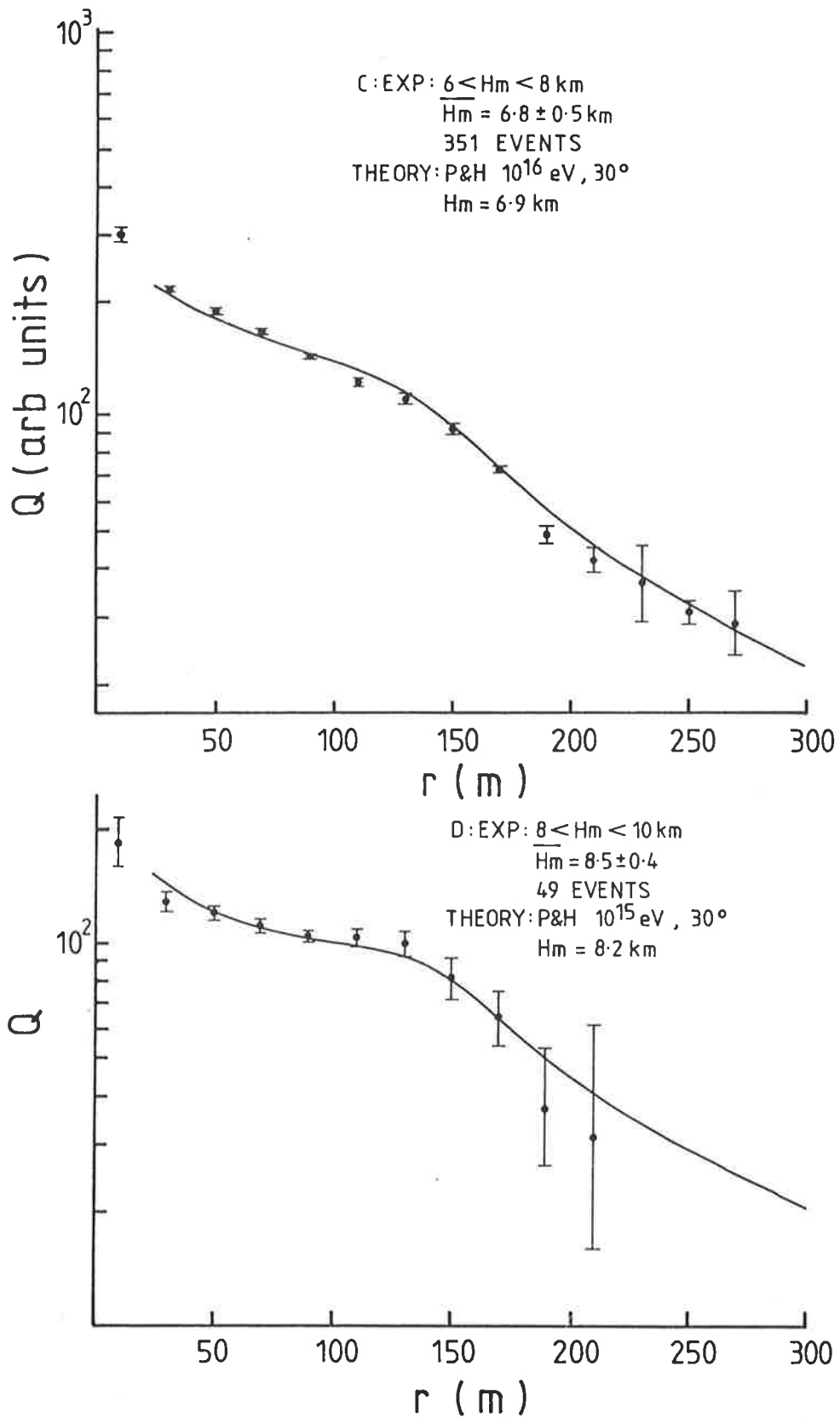


Figure 4.15(c,d): Comparison of lateral distributions, averaged in terms of H_m , with calculations of Patterson and Hillas.

overestimating $Q(150)$ arises in some flatter showers. An alternative method for determining H_m is to fit an exponential function over an even smaller radial range, 25-130m, and to relate the b slope parameter directly to H_m using the results of P & H shown in figure 4.5. Of course this implies the use of a smaller data set, but it should avoid problems associated with the curvature in the lateral distribution outside 130m for showers developing high in the atmosphere. We have taken the 863 events of data set C and have fitted exponential functions between 25 and 130m. The distance to maximum for each shower was calculated directly from the b slope parameter using the following expressions (derived from figure 4.5)

$$\begin{array}{ll}
 \theta < 10^\circ & H_m = - 0.023 b + 7.3 \text{ km} \\
 10^\circ < \theta < 20^\circ & H_m = - 0.024 b + 7.1 \text{ km} \\
 20^\circ < \theta < 35^\circ & H_m = - 0.031 b + 8.4 \text{ km}
 \end{array}
 \tag{Eq. 4.14}$$

The same data set has also been analysed in the previously described way i.e., an exponential fit in the range 25-150m has been used to calculate the flux ratio $Q(50)/Q(150)$ which is used to infer H_m . We have taken a subset of the data for which $5 \times 10^5 < N_e(1000) < 2 \times 10^6$ particles and plotted histograms of H_m determined by each method. The results are shown in figure 4.16. The new method of analysis produces figures for the distance to shower maximum which are, on average, 0.6km smaller. This was expected, although the size of the shift may be a little surprising. At an average

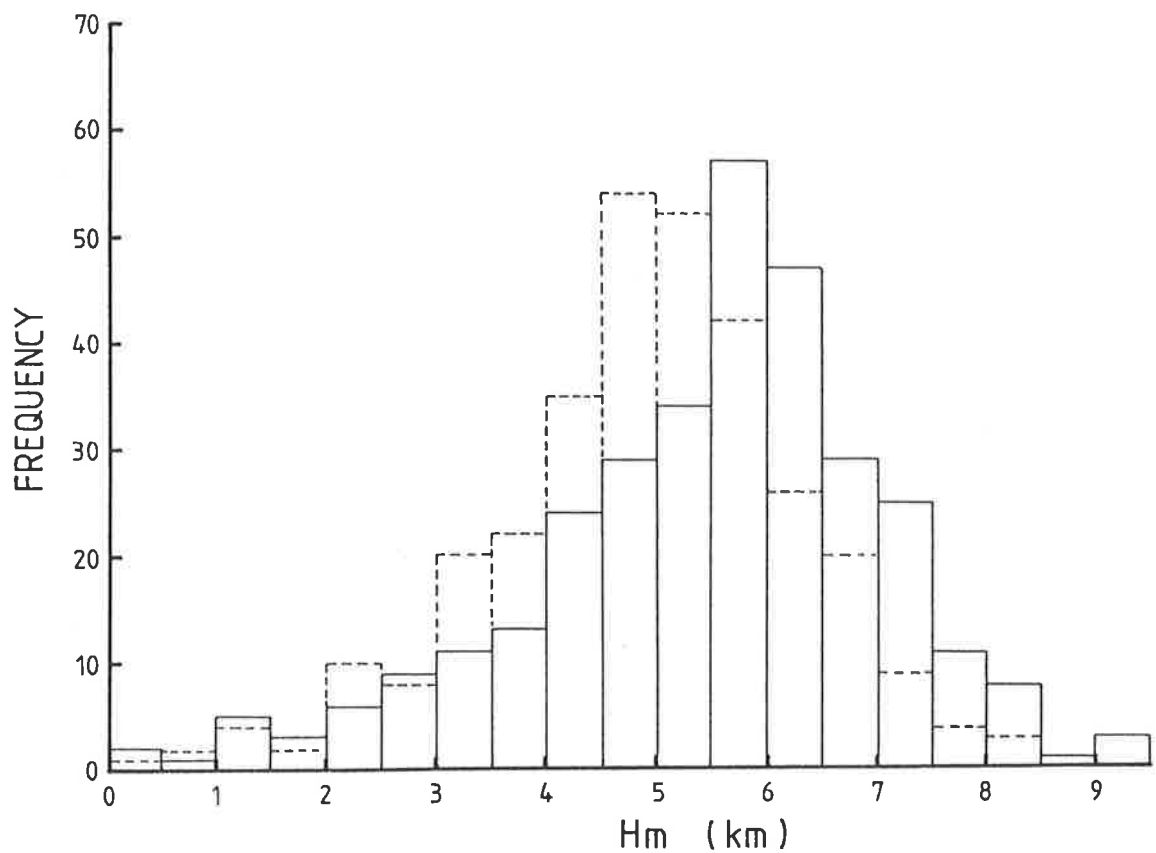


Figure 4.16: Histogram of values of distance to maximum derived using the flux ratio (solid line) and directly from the slope parameter (dashed line).

zenith angle of 20° , this difference in H_m corresponds to a shift in mean depth of maximum of $\sim 40 \text{gcm}^{-2}$. The uncertainty introduced into the conclusions of this study by differences of this sort will be discussed in the following chapter.

In conclusion, we have shown that an exponential function of the form

$$Q(r) = Ae^{-br/10^4}$$

is a good fit to the majority of the experimental lateral distributions in the core distance range 25-150m. However, there is evidence of departures from this behaviour in showers which develop at large distances from the detectors. These features are in agreement with the calculations of Patterson and Hillas (1983b). The shapes of the experimental lateral distributions inside 25m and outside 150m also show the features expected from the calculations.

C H A P T E R F I V E

INTERPRETATION OF DEPTH OF MAXIMUM DATA

5.1 Introduction.

This chapter describes the interpretation of depth of shower maximum distributions derived from measurements of the shape of the Cerenkov lateral distribution. The interpretation is aided by a comprehensive simulation of the selection effects associated with the Buckland Park particle array, the source of a trigger in the experiment. The simulation makes use of a current model of longitudinal air shower development, involving conventional particle physics ideas, to estimate the cosmic ray nuclear composition around 10^{16} eV.

5.2 Experimental Depth of Maximum Distributions.

The simulations of Patterson and Hillas (1983b) were used to assign a distance to shower maximum, H_m , to each event in the data set. The corresponding depths of maximum were calculated knowing the shower zenith angle and by assuming an exponential atmosphere with a scale height of 8.0km (S. Young, private communication). The reader will recall from section 4.4.2 that two methods were used for assigning a H_m to an event using the calculations of Patterson and Hillas. In this chapter we shall present distributions derived using each of these methods, which are set out again below for clarity.

Method 1: The 945 events of data set B (sect. 4.4) were fitted with exponentials of the form

$$Q(r) = Ae^{-br/10^4} \quad \text{Eq. 5.1}$$

in the core distance range 25-150m. On the basis of this fit, the flux ratio $Q(50)/Q(150)$ was calculated and this was used to infer the distance to maximum using the relationships shown in figure 4.4. It was pointed out in Chapter Four that this method sometimes overestimated H_m for those showers which developed at a large distance from the ground.

Method 2: The 863 events of data set C were fitted with exponentials of the same form, but over the smaller core distance range 25-130m to avoid any departures from the exponential form outside 130m. The distance to maximum was calculated directly from the slope parameter b obtained in the fit, using the relationships shown in figure 4.5.

To begin with we shall consider distributions of depth of shower maximum, DOM, versus the shower size at a depth of shower 1000gcm^{-2} , $N_e(1000)$. In figure 5.1, the distributions derived using each of the methods above are shown. The distributions are obviously different, especially in the region between 10^5 and 10^6 particles where Method 2

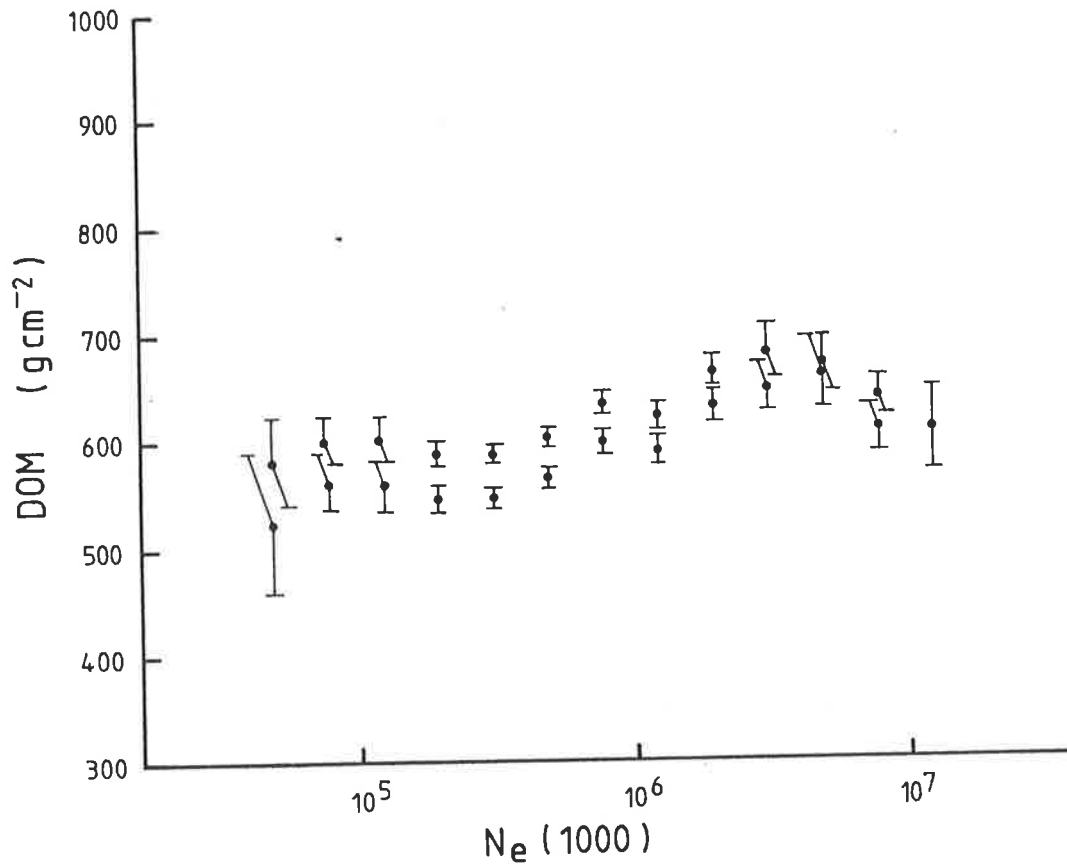


Figure 5.1: Distributions of DOM vs shower size at $1000gcm^{-2}$ derived using Method One (smaller DOM points), and Method Two (larger DOM points).

predicts depths of maximum about 40gcm^{-2} larger than those predicted by Method 1. (This is consistent with Method 1 overestimating the distance to maximum for some showers). An interesting feature of both distributions is the apparent flattening around 10^5 particles. The reason for this feature will become clear in the following section.

The results of a number of calculations discussed in Chapter Four indicate that the Cerenkov flux at a large core distance ($\geq 150\text{m}$) will be a measure of the energy of the primary particle. Fluctuations in this flux due to development fluctuations are smallest at the larger core distances. However, when low energy showers are being investigated it is often impossible to measure accurately fluxes outside $\sim 150\text{m}$. In these cases a compromise must be made. A convenient energy estimator for the data analysed using Method 1 was the flux at 150m , $Q(150)$, calculated using the exponential fit. In the case of Method 2, a convenient estimator was the flux at 130m , $Q(130)$, again calculated using the exponential fit. Figure 5.2a shows a plot of DOM vs $Q(150)$ for the data analysed using Method 1. Figure 5.2b shows a similar distribution for the data analysed using Method 2. A curious feature is evident in both of these figures - a rapid increase in DOM at low energies. The high energy ends of the distributions are also rather flat.

The number of particles in a shower at maximum is also known to be a good measure of the energy of the primary particle (e.g. Hillas 1983). Unfortunately, this number cannot be inferred from the sea level shower size without a measurement of the DOM and a complete knowledge of the shape of

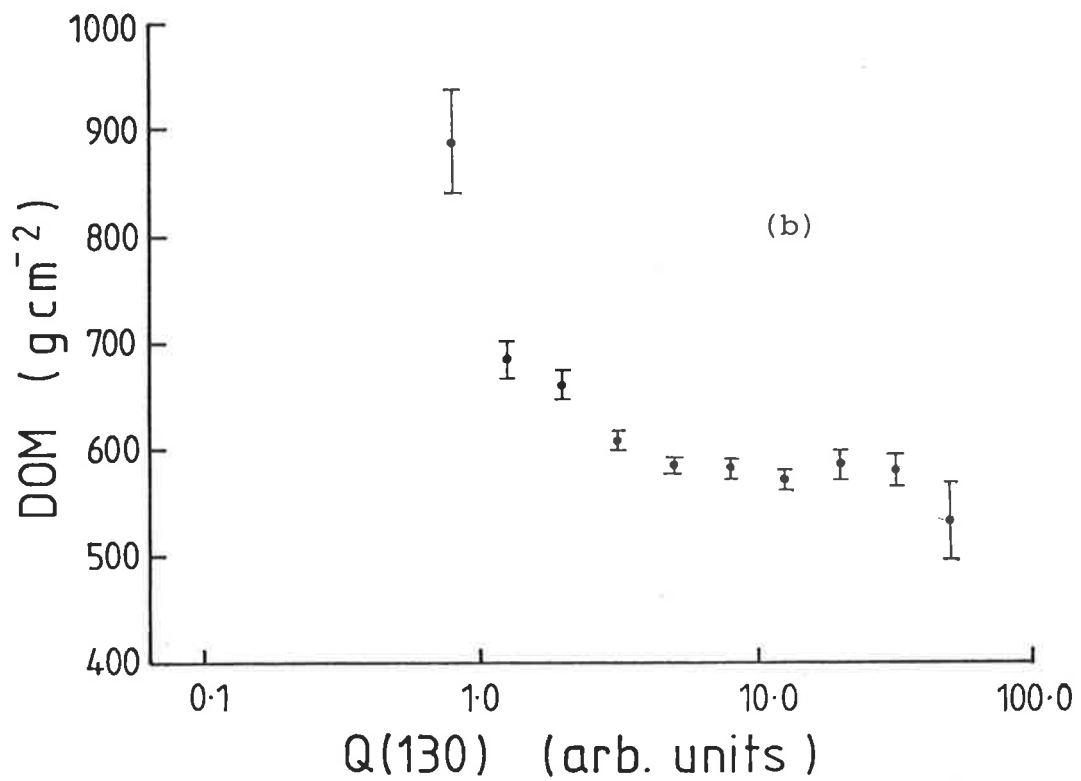
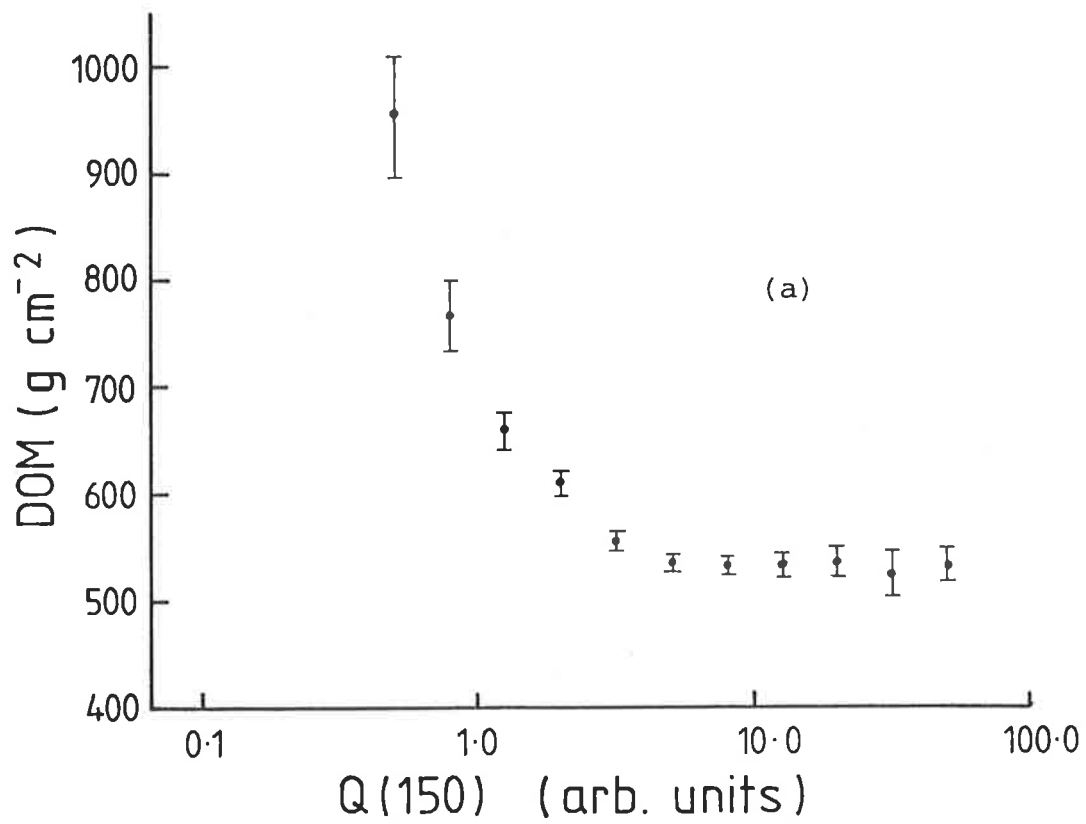


Figure 5.2: Distributions of DOM vs an energy estimator.
 a: DOM vs Q(150), Method One.
 b: DOM vs Q(130), Method Two.

the cascade development curve. However, the shower size at a fixed depth past maximum is also expected to be a measure of primary energy, albeit not such a good one. This size can be calculated from the sea level size using the DOM and an estimate of the shower attenuation length. We have used the shower size at a depth of 550gcm^{-2} past maximum, $N_e(\text{DOM}+550)$, as another estimator of primary energy (as used by Thornton 1984). This parameter was calculated using an attenuation length of 185gcm^{-2} (Clay and Gerhardy 1982). Figures 5.3(a,b) show the distributions of DOM vs $N_e(\text{DOM}+550)$ derived using Methods 1 and 2. These figures exhibit the same feature seen in figure 5.2 - a trend towards large DOM at small "energies". A comparison of figures 5.2 and 5.3 confirms that the parameters $Q(150)$ (and $Q(130)$) and $N_e(\text{DOM}+550)$ are measuring the same thing. We shall show later that they are indeed measuring primary energy.

It is noted that the unusual feature of the distributions in the energy representation does not appear in the shower size distributions of figure 5.1. However, the flattening of the distributions at small shower sizes may be a result of the same process. In the following section we investigate the cause of these unusually shaped distributions - particle array selection bias.

5.3 A Simulation of Particle Array Selection Effects.

Because of the unusual features of the depth of maximum distributions discussed in the previous section, it was decided that a simulation was required to test for selection biases in the particle array. It was known that the particle

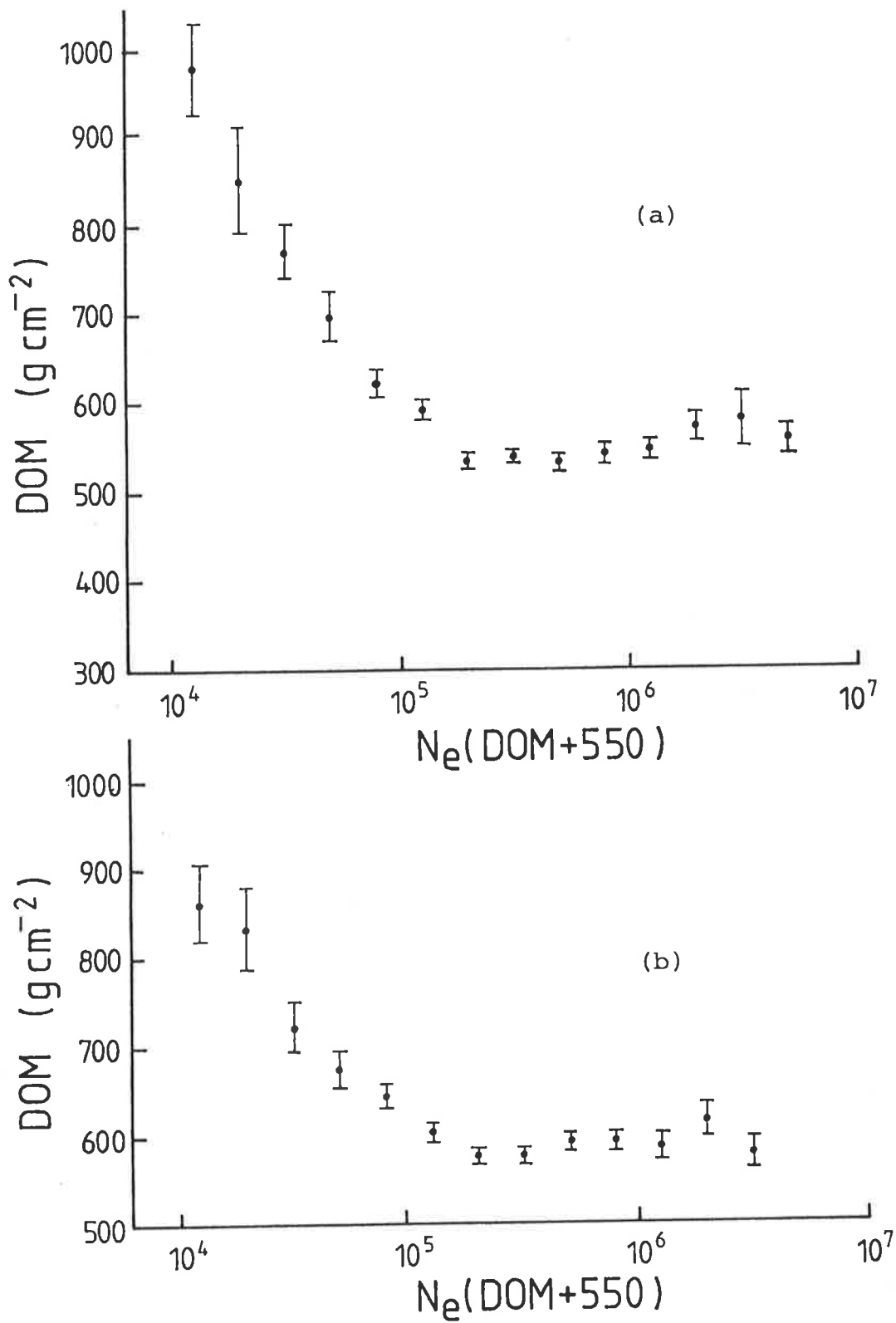


Figure 5.3: Distributions of DOM vs an energy estimator.
 a: DOM vs $N_e(\text{DOM}+550)$, Method One.
 b: DOM vs $N_e(\text{DOM}+550)$, Method Two.

array triggering requirements could produce the effect seen, since only late developing (large DOM), low energy showers would have a sea level shower size large enough to trigger the array. However, it was not known how extensive this bias would be.

Because the Cerenkov experiment relied on a particle array trigger, biases in the particle array would bias the Cerenkov study. Any selection effects associated with the Cerenkov array alone are expected to be small, because of the existence of a large and measurable Cerenkov flux at sea level down to energies at which no particle signal exists. For this reason, an experiment using a Cerenkov trigger would be preferable. However, in the case of the present experiment, which used relatively slow risetime (~ 20 ns) photomultipliers over a relatively short baseline (~ 100 m), the particle array was needed to at least provide shower direction information.

Briefly, the calculation was a Monte Carlo simulation carried out in the following way. Cosmic ray primaries were allowed to fall on the top of the atmosphere. The particle energy was assigned to each event by sampling from a broken power-law energy spectrum in the energy range $10^{13} - 10^{18}$ eV. A depth of maximum for each shower was sampled from distributions based on recent calculations of longitudinal shower development. The shower size at maximum was calculated using the primary energy, and the shower size at sea level was calculated using an appropriate shower cascade profile. The core location and arrival direction of the shower were chosen randomly, and the expected particle density in each of the particle array detectors was calculated. Showers satisfying

the array triggering conditions were re-analysed for shower size and core location using the analysis program employed in the reduction of the experimental data. In this way, any selection biases present in the array triggering and the analysis procedure were included in the simulation results.

The simulation was carried out for a flux composed entirely of protons, and again for a flux of 100% iron nuclei. In the following paragraphs a more detailed discussion of the procedure will be given.

1. Energy Assignment.

The energy of a primary particle was chosen from a broken power-law energy spectrum of the same form for both protons and iron nuclei. The energy range covered was $10^{13} - 10^{18}$ eV and the exponents of the integral spectrum used were:

$$\gamma = -1.6 \quad \text{for } 10^{13} < E < 10^{16} \text{ eV}$$

Eq. 5.2

and $\gamma = -2.1 \quad \text{for } 10^{16} < E < 10^{18} \text{ eV}$

where E is the primary energy. The simulation was organized so that a statistically significant number of primaries was selected in each of 25 equal width (on a logarithmic scale) bins between 10^{13} and 10^{18} eV. The power law spectrum was used to select the shower energies within each bin and also to assign a weighting factor to all of the data in each of the bins. The procedure (like all others in this section) was thoroughly tested to ensure that the resulting spectrum matched

the input distribution.

2. Depth of Maximum Assignment.

The depth of maximum of each shower was assigned using a procedure outlined by Protheroe and Patterson (1984). In this paper, a number of results concerning the distribution of depths of maximum as a function of energy were summarised. For example, they quote Linsley (1982) who fitted a function to the variation of mean DOM with energy for proton initiated showers, using the simulations of several authors, each of whom employed the scaling model of particle interactions. He gives

$$\bar{x}_m \sim \lambda_p + 5\text{gcm}^{-2} + (X_0 + 0.032\lambda_\pi) \ln(E/10^9 \text{ eV}) \quad \text{Eq. 5.3}$$

where \bar{x}_m is the mean DOM, X_0 is the radiation length of air (taken to be 36.1gcm^{-2}), λ_p is the mean proton interaction length in air, and λ_π is the mean pion interaction length (taken to equal $1.38\lambda_p$). Note that λ_p (and hence λ_π) is energy dependent. Protheroe and Patterson note that Gaisser et al (1983) have surveyed recent data on pion production in hadron-light nucleus collisions, and have produced a more realistic model of hadron-air nucleus collisions. The result of this model (which includes a mild scaling violation) is a reduction in the values of \bar{x}_m by $\sim 30\text{gcm}^{-2}$. Thus, Protheroe and Patterson have used Eq. 5.3 but have reduced the values of \bar{x}_m by 30gcm^{-2} . The same approach was used in the present work. That is, the expression used for proton initiated showers was

$$\bar{x}_m = \lambda_p - 25 \text{gcm}^{-2} + (X_0 + 0.032\lambda_\pi) \ln(E/10^9 \text{eV}) \quad \text{Eq. 5.4}$$

The superposition model was used to assign depths of maximum to iron initiated showers. This model states that

$$\bar{x}_m(E, A) = \bar{x}_m(E/A, 1) \quad \text{Eq. 5.5}$$

where A is the nuclear mass of the primary (for iron, A = 56).

Protheroe and Patterson took the results of simulations of shower development fluctuations performed by Ellsworth et al (1982) and Ellsworth and Yodh (1981) and parametrised the distributions in depth of maximum for showers of a given energy, E. The result is

$$P_A(x_m, E) = \begin{cases} \frac{167}{\lambda} \exp\left(\frac{x_m - \bar{x}_m}{0.3\lambda}\right) & x_m < (\bar{x}_m - 1.94\lambda) \\ \frac{0.26}{\lambda} & (\bar{x}_m - 1.94\lambda) < \bar{x}_m < x_m \\ \frac{0.26}{\lambda} \exp\left(\frac{\bar{x}_m - x_m}{1.6\lambda}\right) & x_m > \bar{x}_m \end{cases} \quad \text{Eq. 5.6}$$

where \bar{x}_m and λ (the interaction length) both depend on E and A. Using the data reproduced in Protheroe and Patterson, the mean proton interaction length was taken to be

$$\lambda_p = 67.2 (E/10^{14} \text{eV})^{-0.065} \text{gcm}^{-2} \quad \text{Eq. 5.7}$$

and that for iron was taken to be constant at $\lambda_{\text{Fe}} = 13 \text{gcm}^{-2}$.

Thus, given a shower primary energy, a mean depth of maximum was calculated using Eq. 5.4 (and Eq. 5.5 for iron)

which was in turn used to select a fluctuated depth of maximum from the parametrisation given in Eq. 5.6.

3. Shower Size Assignment.

The number of particles in the shower at maximum was calculated using the results of Hillas (1983), which relate this number to the primary energy of the shower. The following relationships were used,

$$N_e(\text{max}) = \frac{E}{1.4 \times 10^9 \text{ eV}} \quad \text{for } E \geq 4.2 \times 10^{15} \text{ eV}$$

Eq. 5.8

$$= \frac{E}{(-0.059 \log(E/10^{14} \text{ eV}) + 1.6) \times 10^9} \quad \text{for } E < 4.2 \times 10^{15} \text{ eV}.$$

These relationships are independent of the nature of the primary particle.

Given the shower size at maximum, the next task was to calculate the shower size at sea level ($\sim 1000 \text{ gcm}^{-2}$). To do this, the shower arrival direction was chosen randomly from appropriate distributions of azimuth and zenith angles. (In the case of the azimuth angle, θ , the probability distribution was flat in ϕ , while for the zenith angle, ϕ , the probability distribution was flat in $\sin\theta$). Then, a typical shower development profile from Patterson and Hillas (1983a) (figure 5.4), normalised to the calculated $N_e(\text{max})$ at maximum, was used together with the DOM and θ values to estimate the sea level shower size.

In order to simulate a more realistic electron lateral distribution, an age parameter, s , was assigned to each shower at sea level, for use in the NKG function (sect.

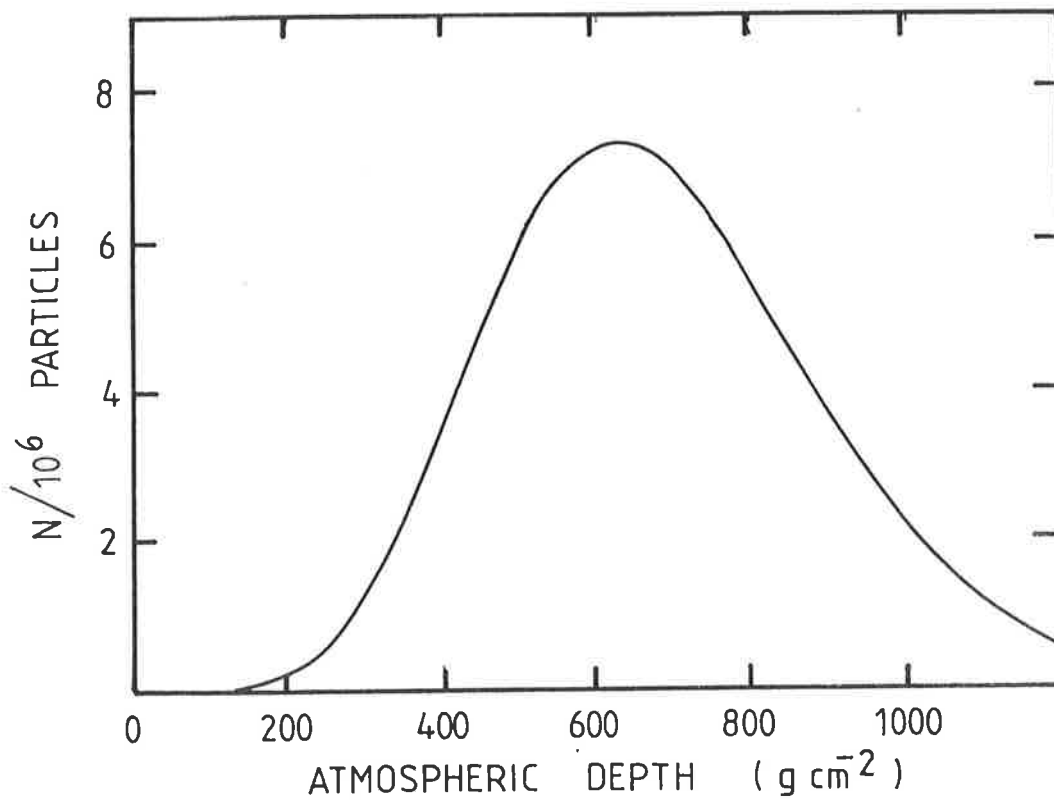


Figure 5.4: The typical shower development profile used in the simulation (after Patterson and Hillas 1983a)

2.2.3). The assignment was based on the work of Clay et al (1981), which showed that the measured age parameter increased by 0.06 for every additional 100gcm^{-2} between the observer and shower maximum. The age parameter at shower maximum was set at 1.0 (from electromagnetic cascade theory) and the depth of atmosphere between maximum and sea level was used to estimate the s parameter at the ground, viz.

$$s = 1.0 + ((1000\sec\theta - \text{DOM})/100.) \times 0.06 \quad \text{Eq. 5.9}$$

A more sophisticated treatment of the s parameter was not possible (and was probably not warranted).

4. Array Triggering.

Each simulated shower was allowed to fall on the array within an area of $500\text{m} \times 500\text{m}$ centred on detector C. The expected particle density in each of 12 the detectors was calculated with the NKG lateral distribution using the previously calculated values of sea level size and age parameter. The number of particles in each detector was then subjected to a random Poisson fluctuation to simulate the statistical fluctuations in measured densities.

The showers were recorded if they satisfied a form of the "fast trigger" described in section 3.2. The requirement was >2 particles in C detector and >2 particles in three of the four detectors ABDE.

The data sets containing proton and iron initiated showers were subsequently passed through the particle array analysis program developed to analyse the actual experimental

data. This program took showers which possessed >5 measured densities and produced an estimate of the shower size, shower age and core location on the basis of these densities. (By comparing these parameters with their original values, a test of the analysis procedure was possible; good agreement was found).

Thus, the simulation resulted in two data sets, one for proton showers and one for iron showers, containing events which should be directly comparable with those making up the experimental distributions discussed in the previous section. Any manifestations of selection biases associated with either the particle array triggering conditions or the particle analysis procedure will be present in the simulated data as well as the experimental data.

We shall now summarise the results of the simulation. Figure 5.5 shows the differential sea level shower size spectra for proton and iron initiated showers. (These showers did not necessarily trigger the array, nor were they reanalysed). Note that the form of the spectra is as expected and that an appropriate spectral index is approached at large shower sizes. The rate of iron produced showers of given size is smaller than that of proton showers due to the fact that iron showers develop, on average, higher in the atmosphere. This fact also explains the data shown in figure 5.6. Here, the relationships between shower size at 1000gcm^{-2} and primary energy, for proton and iron initiated showers, are shown. Both curves are well described by power laws, viz.

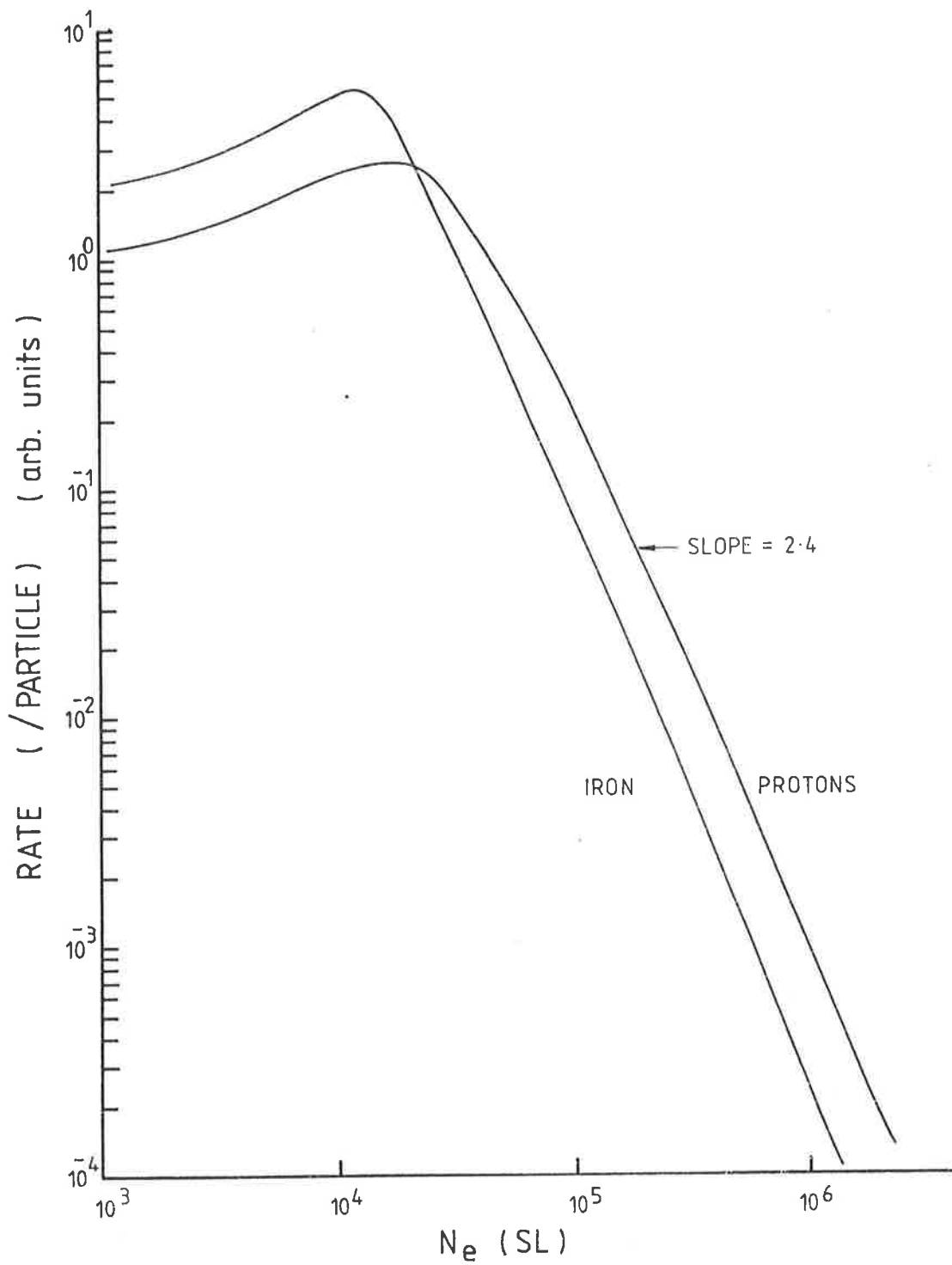


Figure 5.5: Differential sea level shower size spectra for proton and iron induced showers (with no array triggering imposed).

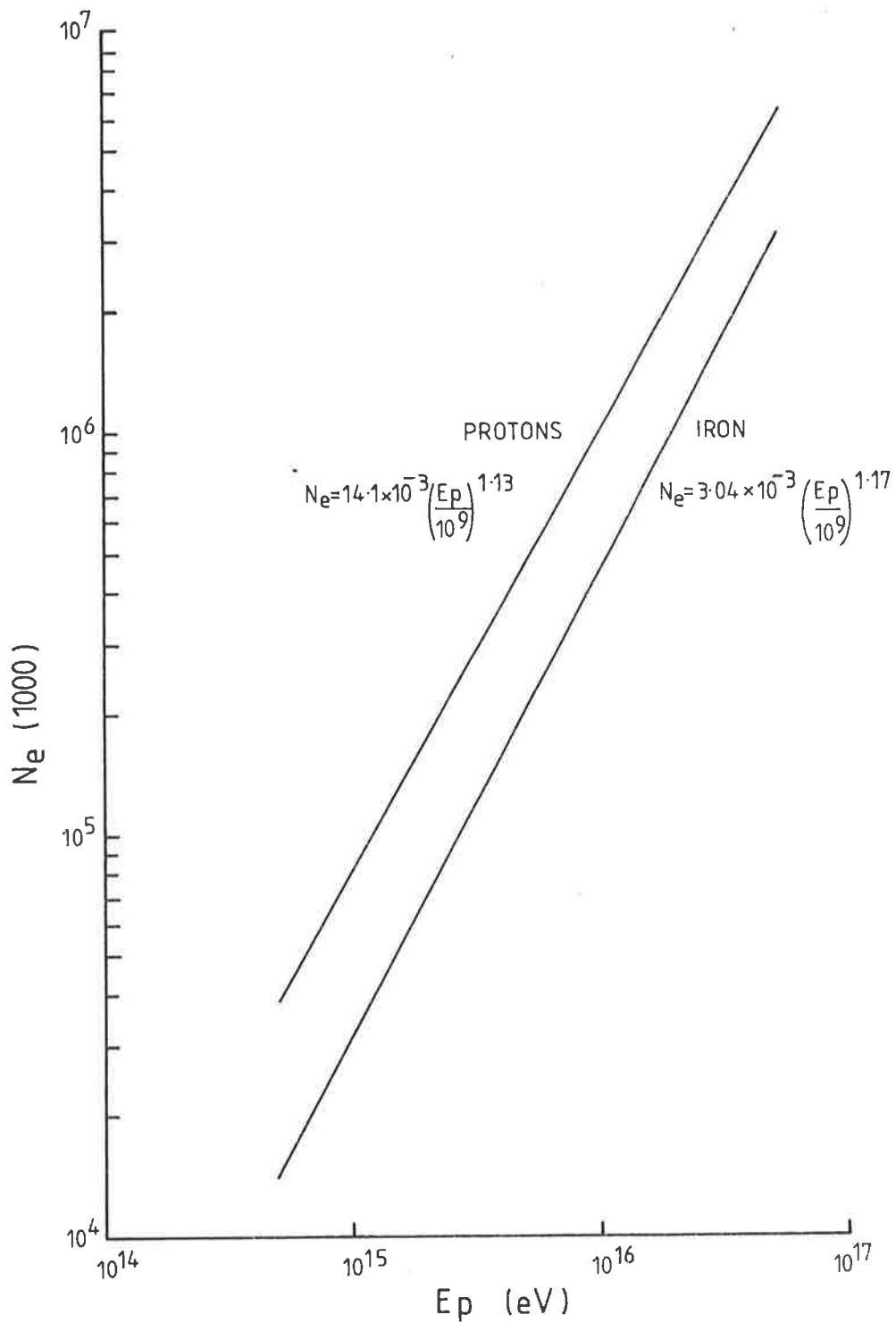


Figure 5.6: The relationship between the shower size at a depth of 1000gcm^{-2} and primary energy, for proton and iron initiated showers.

for protons, $N_e(1000) \sim 14.1 \times 10^{-3} (E/\text{GeV})^{1.13}$

Eq. 5.9

for iron, $N_e(1000) \sim 3.04 \times 10^{-3} (E/\text{GeV})^{1.17}$

As expected, iron primaries produce smaller sea level showers than proton primaries of the same energy.

Shown in figure 5.7a are some results from the simulation of proton induced showers. Here we plot the distributions of DOM vs. primary energy for

1. all showers (i.e., the "input" distribution, eq. 5.4).
2. only those showers with $>10^3$ particles at sea level.
3. only those showers which satisfy the fast trigger requirement.

The results are quite striking. They show that there is a departure in 2 and 3 from the input distribution at the lower energies. The low energy showers which reach ground level and are observed are produced by showers which develop low in the atmosphere (large DOM). Another way of stating this result is to say that there is a selection bias at low energies towards late developing showers. A similar diagram is shown in figure 5.7b for showers initiated by iron nuclei. Here the bias is not as large. This is because the fluctuations in depth of maximum for iron showers are smaller than those for proton showers (see eqs. 5.6, 5.7). Consequently, there are not as many downward fluctuated showers capable of reaching the ground and triggering the array. Iron showers also develop higher in the atmosphere than proton showers of the same energy, and it

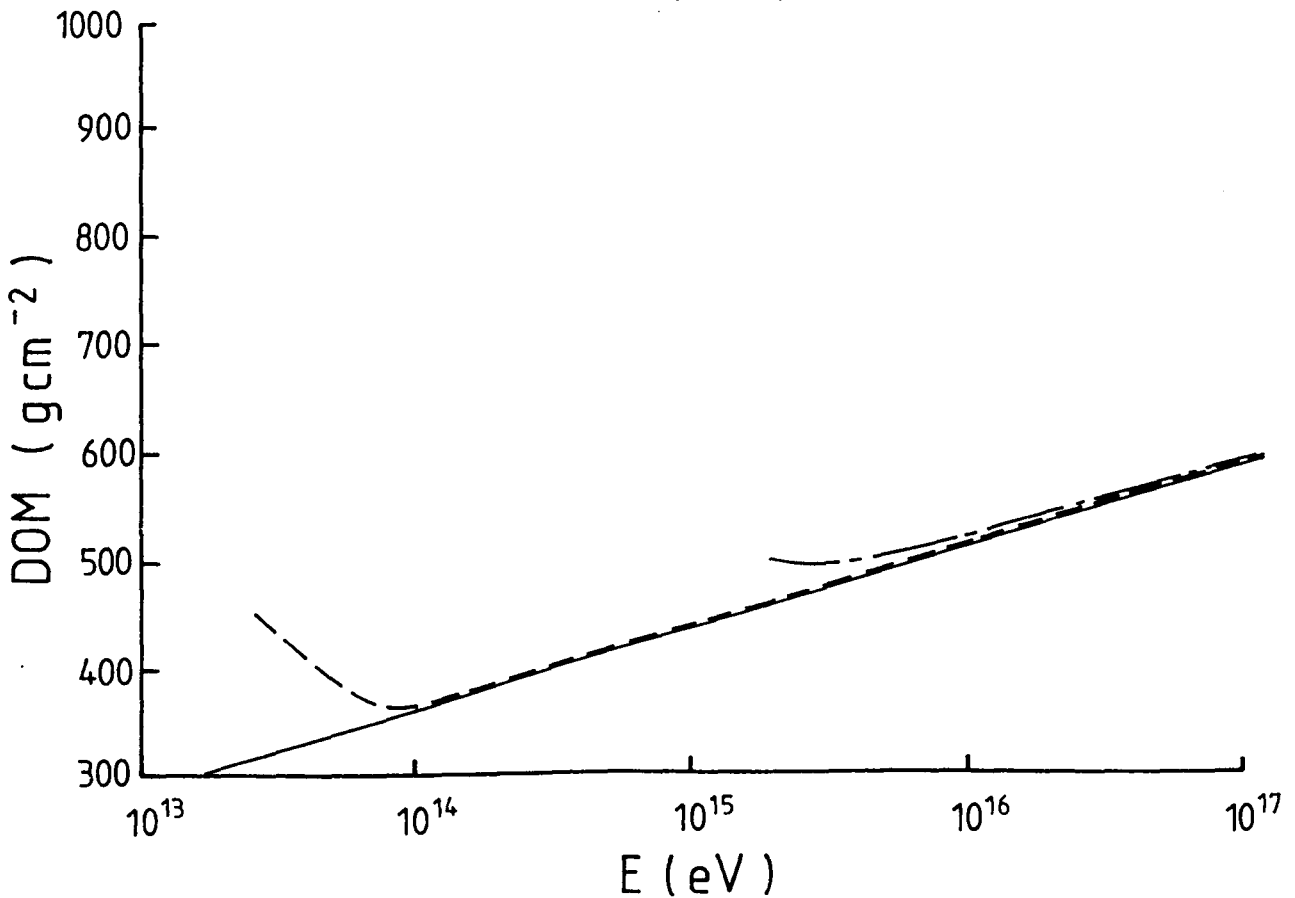
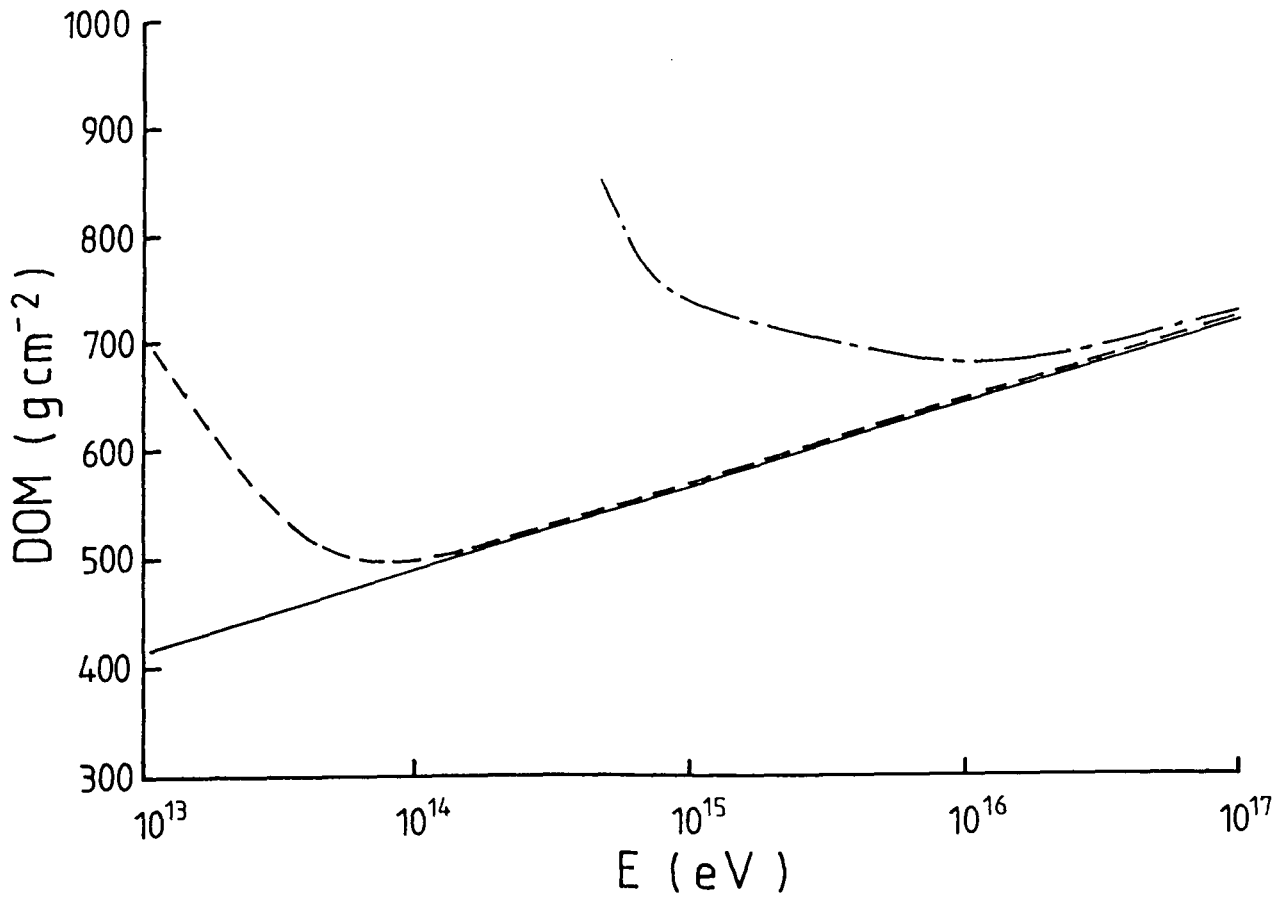


Figure 5.7: a: DOM vs primary energy for proton showers, for all showers (solid line), only showers with greater than 1000 particles at sea level (dashed line), and only showers which satisfy the fast trigger requirement (chain line).
 As above, but for iron induced showers.

is for these reasons that the fraction of iron induced showers which are analysable at sea level is low at low energies. In figure 5.8 we show the percentage of primary particles incident on the top of the atmosphere which produce showers large enough at sea level to be analysed by the array analysis procedure, as a function of primary energy. It can be seen that at 3×10^{15} eV, ~3.5% of proton showers are analysable, while the corresponding figure for iron showers is only ~0.6%.

In figure 5.9 we show the depth of maximum versus primary energy distributions for proton and iron showers which have satisfied the fast trigger and are large enough to be analysed by the array analysis routine. In this figure we have added shaded regions representing the standard deviations around the mean depth of maximum distributions. The standard deviations reflect the size of the fluctuations in depth of maximum. The larger fluctuations in development evident in the proton data again show why these showers are more susceptible to array bias effects.

An interesting result of the simulation is that while the array and analysis procedure selection effects are quite obvious when the data is plotted in this way, they do not stand out when the depth of maximum is plotted as a function of shower size instead of energy. Figures 5.10(a,b) show the same analysed data plotted as a function of $N_e(1000)$. The trend towards large DOM at small shower sizes, which may have been expected on the basis of the experience in the energy representation, is not particularly obvious in either curve, although there is an indication of a flattening in the proton distribution. It appears that the effect of the low energy,

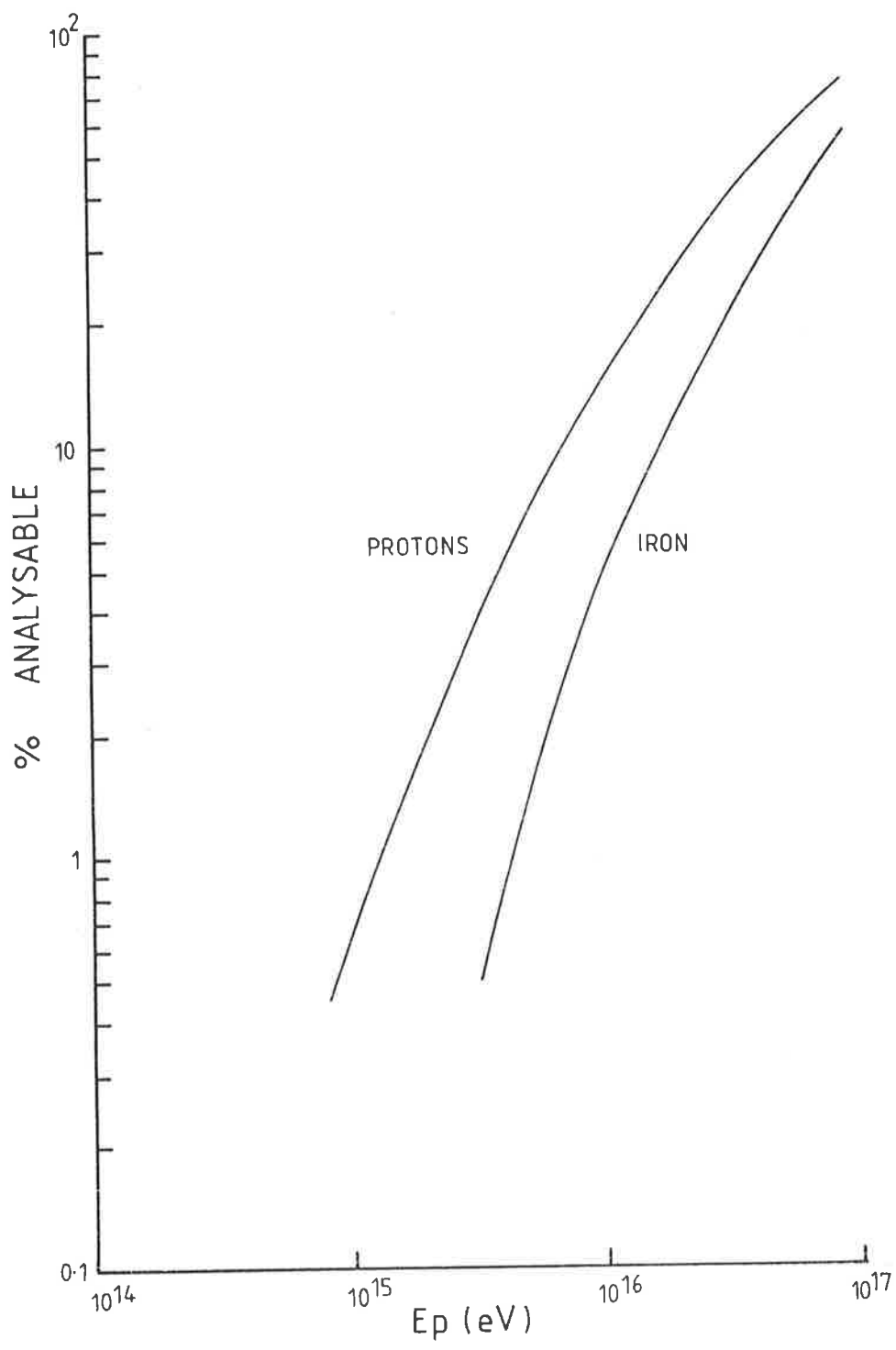


Figure 5.8: The percentage of primary particles which produce showers large enough at sea level to be analysed by the array analysis procedure.

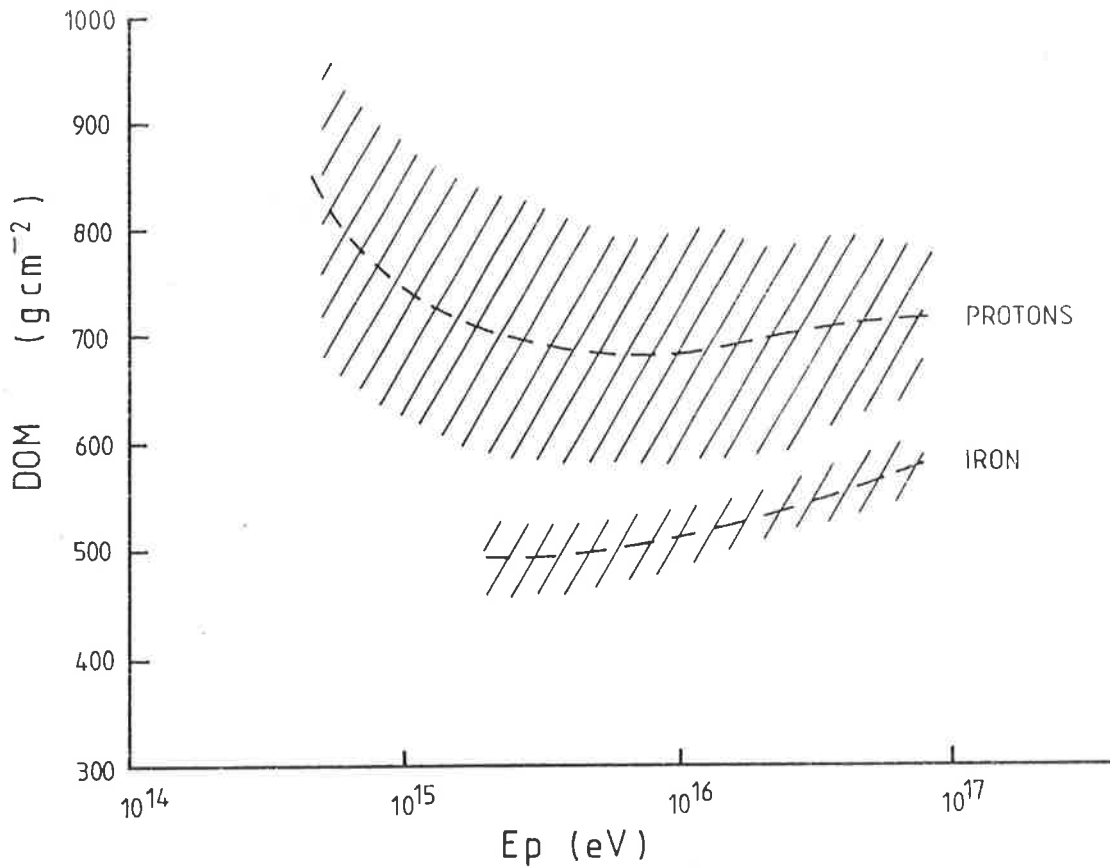


Figure 5.9: Simulated DOM vs energy distributions for proton and iron induced showers. The dashed lines represent the mean behaviour, while the shaded regions represent standard deviations.

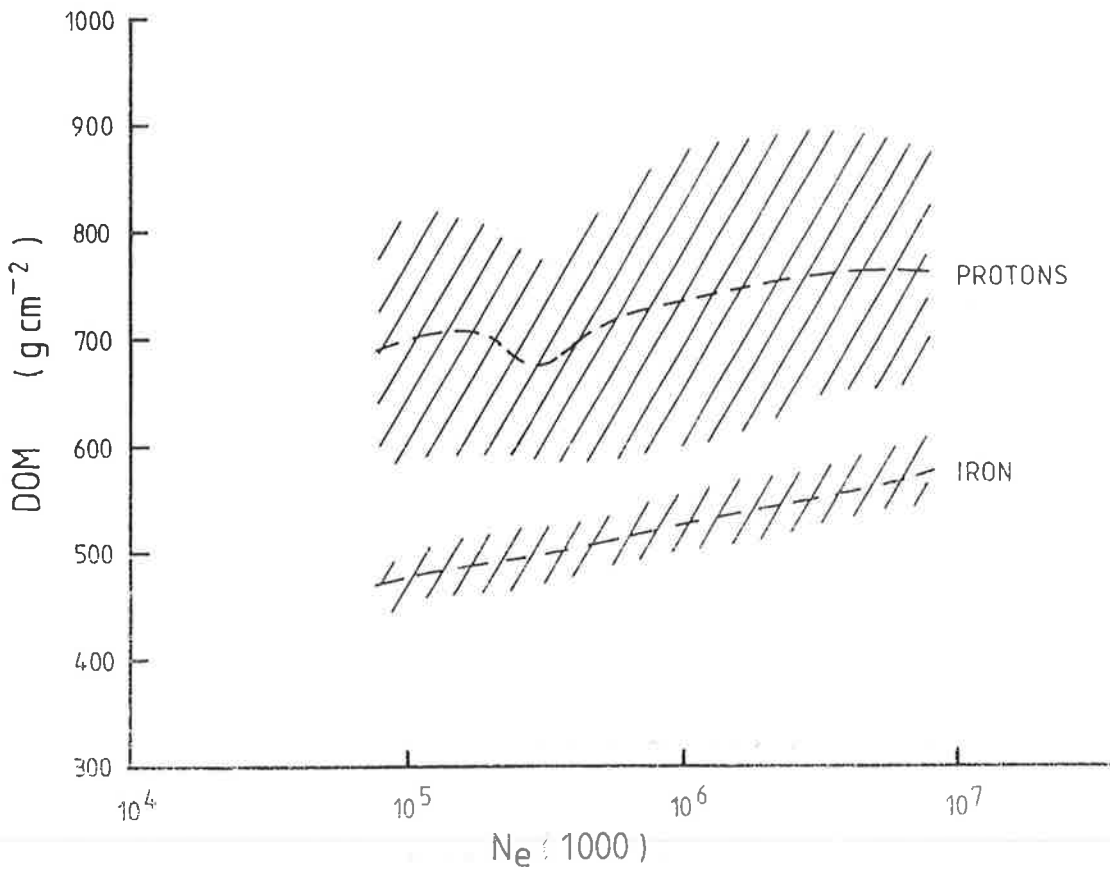


Figure 5.10: Simulated DOM vs shower size distributions for proton and iron induced showers.

late developing showers has been diluted through the mixing of showers of a given energy over a range of shower sizes.

5.4 Interpretation of the Depth of Maximum Distributions.

Armed with a set of simulations of array selection effects, it is now possible to interpret the experimental depth of maximum distributions described in section 5.2. To do this, the experimental DOM vs $N_e(1000)$ distributions were compared with distributions obtained by mixing various proportions of simulated proton and iron induced showers*. The percentages expressed in this section will refer to the fraction of the total flux at the top of the atmosphere made up of a particular type of primary particle.

In figure 5.11 we compare the DOM vs $N_e(1000)$ distribution of showers analysed using Method 1 (from figure 5.1) with the distributions for a 100% proton flux and a 100% iron flux. It can be seen that the experimental distribution lies closer to the distribution for a pure iron beam. In fact, it was found that a mixture of 95% iron and 5% protons produced a distribution which was consistent with the experimental data. The comparison can be made in figure 5.12a. The agreement between the two distributions is considered to be very good. The data are replotted in figure 5.12b. Here, the error bars on the experimental points represent standard deviations, rather than standard errors on the mean, for comparison with the shaded region representing simulated fluctuations. The experimental standard deviations are in fact larger than predicted, which is expected because of experimental uncertainties in the assignment of the depth of

* At these energies, the cosmic ray flux may well be rich in iron (see section 1.3.2). Considering this result, and the precision of the Cerenkov radiation techniques, a simulated composition containing a mixture of protons and iron nuclei was considered appropriate.

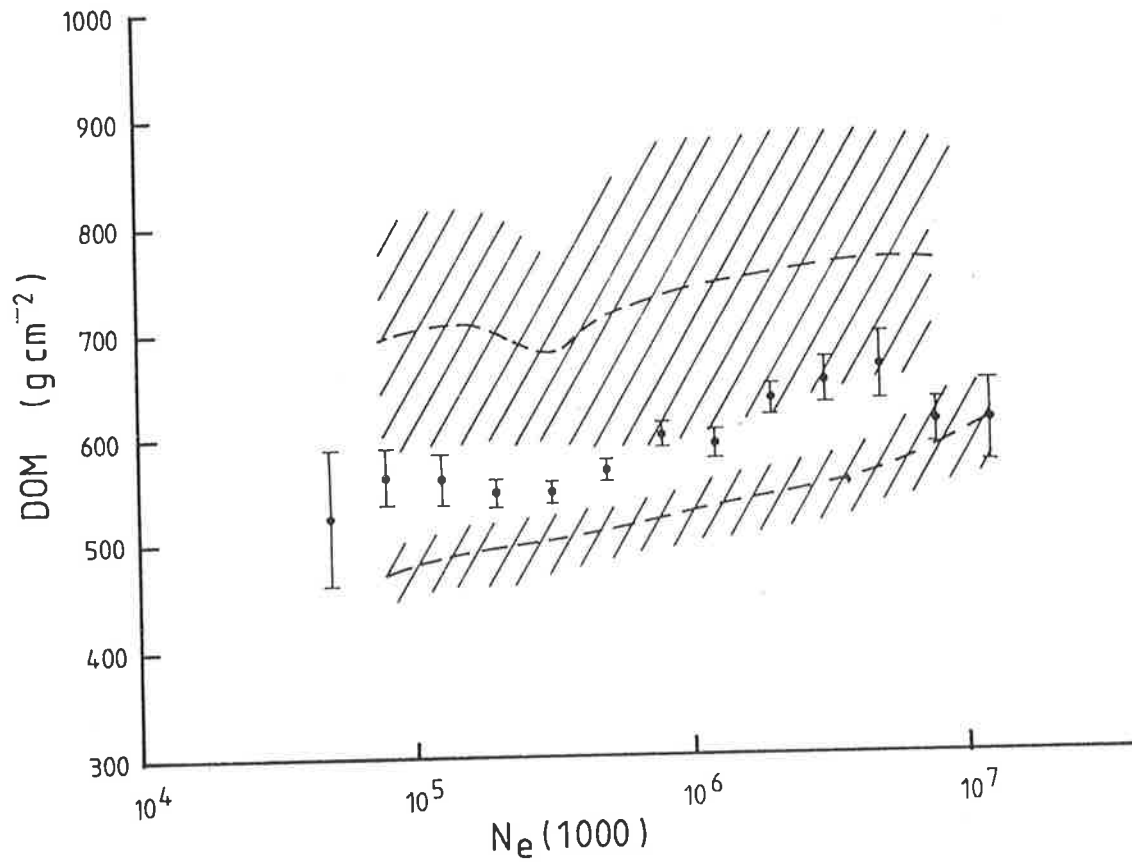


Figure 5.11: Comparison of figure 5.10 with the experimental DOM vs shower size distribution derived using Method One.

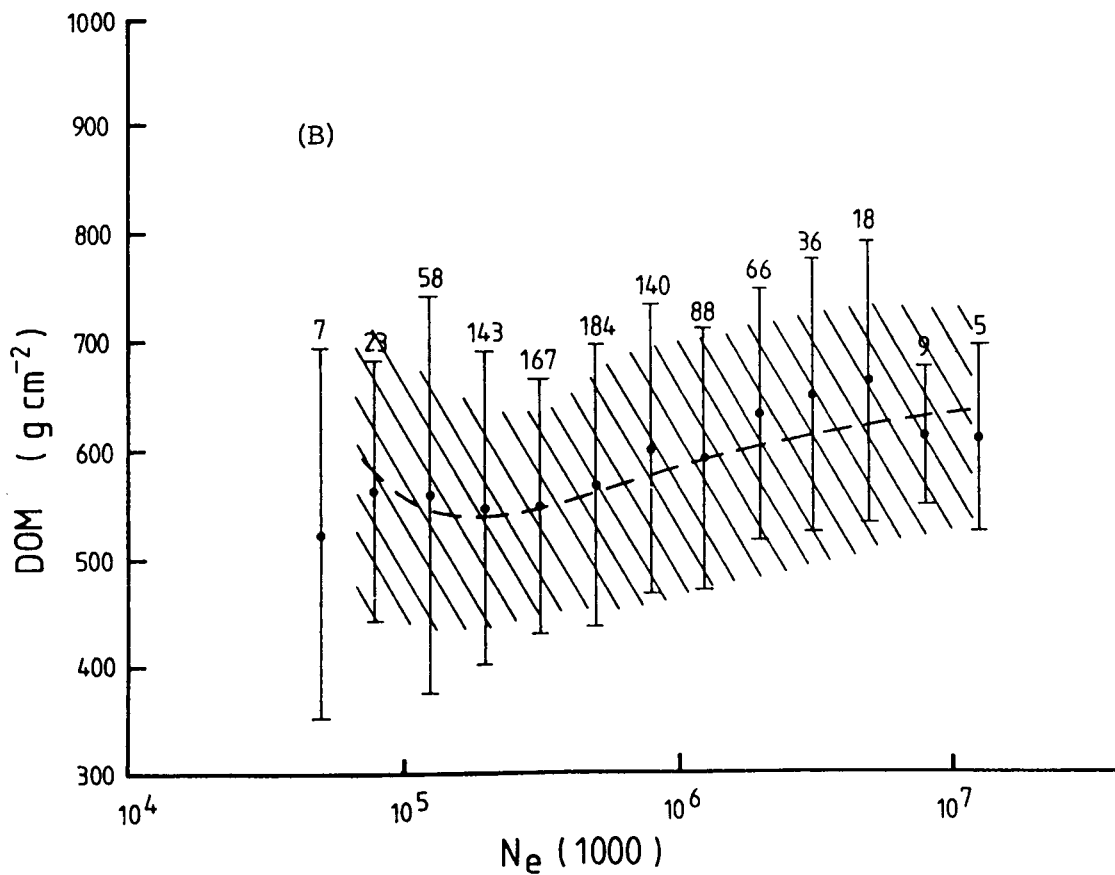
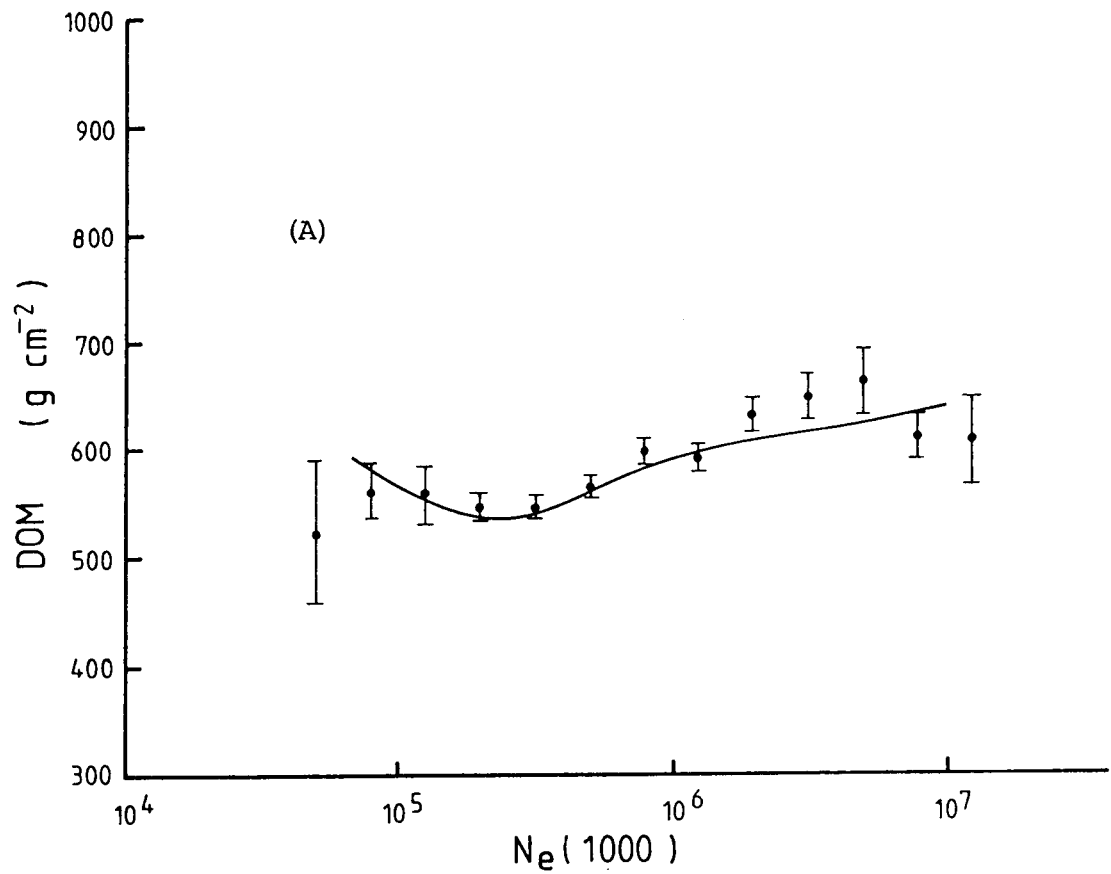


Figure 5.12: Comparison of Method One data with the distribution expected with a composition of 95% Fe and 5% p.
 A: Comparison of mean behaviour.
 B: Comparison of fluctuations (see text).

maximum.

In figure 5.13 we repeat the exercise for the data processed using Method 2. In this case, a mixture of 85% iron and 15% protons was found to fit the variation in mean DOM remarkably well (fig 5.13a). However this mixture does overestimate the fluctuations apparent in the experimental distribution (fig 5.13b). If the experimental deviations do reflect accurately the development fluctuations then they point to an even larger fraction of iron in the flux.

We now turn to the energy representations of the experimental depth of maximum data. In section 5.2 we discussed two energy estimators, the Cerenkov flux at a fixed core distance ($Q(150)$ or $Q(130)$) and the shower size at a fixed depth past maximum ($N_e(DOM+550)$). In figures 5.14(a,b) we show again the distributions of DOM vs $Q(150)$ and DOM vs $N_e(DOM+550)$ produced using Method 1. Superimposed on each figure is the simulated DOM vs primary energy distribution for a mixture of 95% iron and 5% protons, the mixture which was found to match the experimental shower size distribution. (In both cases the simulated results have been shifted arbitrarily sideways in order to get the best agreement). The agreement between the shapes of the experimental and simulated distributions is considered to be excellent. The same data are plotted in figure 5.15 showing the comparison of standard deviations.

The same procedure is followed for the distributions produced by Method 2. In the shower size representation a mixture of 85% iron and 15% protons was found to match the data. Consequently, we have used this mixture to compare with

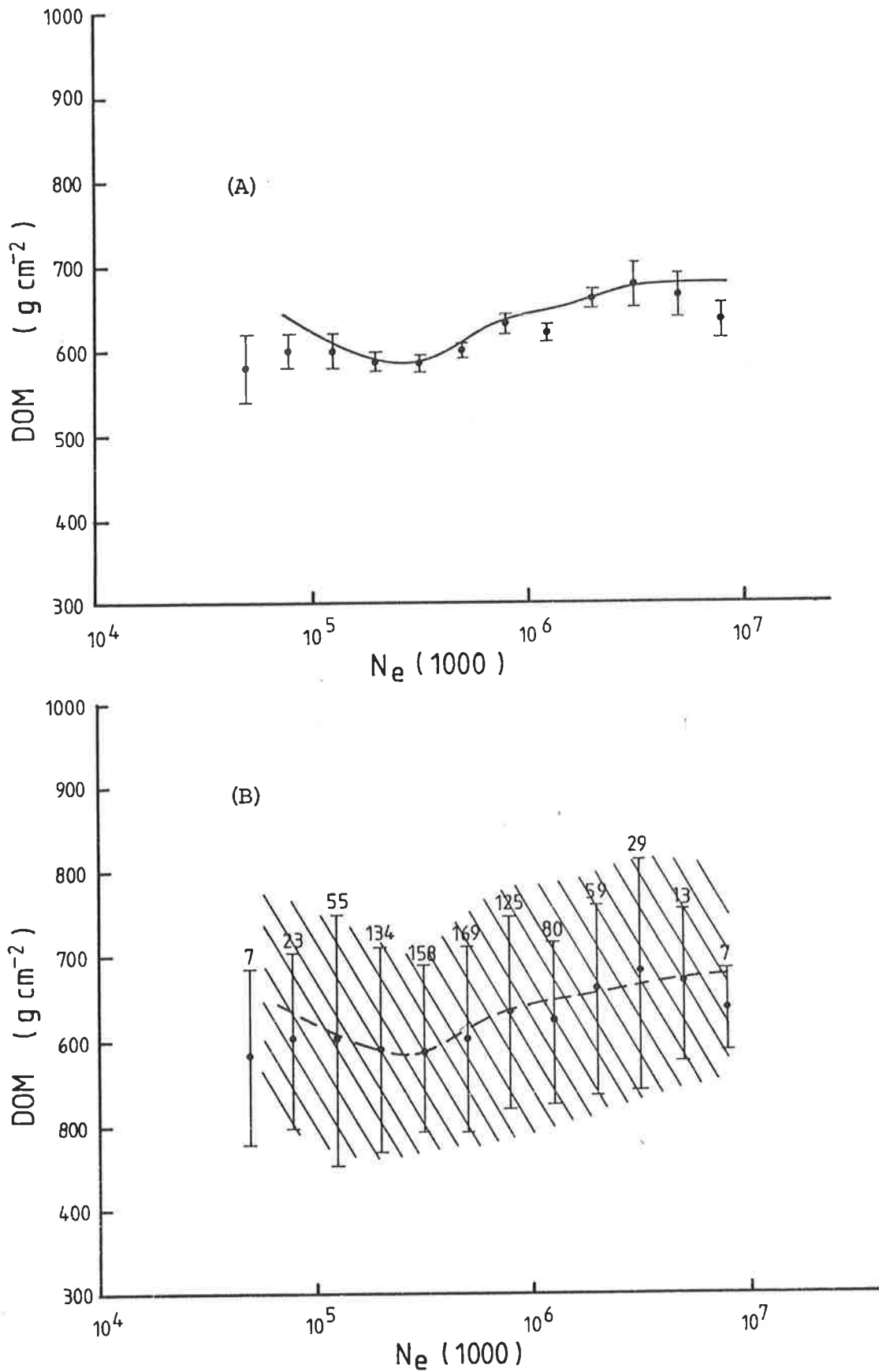


Figure 5.13: Comparison of Method Two data with the distribution expected with a composition of 85% Fe and 15% p.
 A: Comparison of mean behaviour.
 B: Comparison of fluctuations.

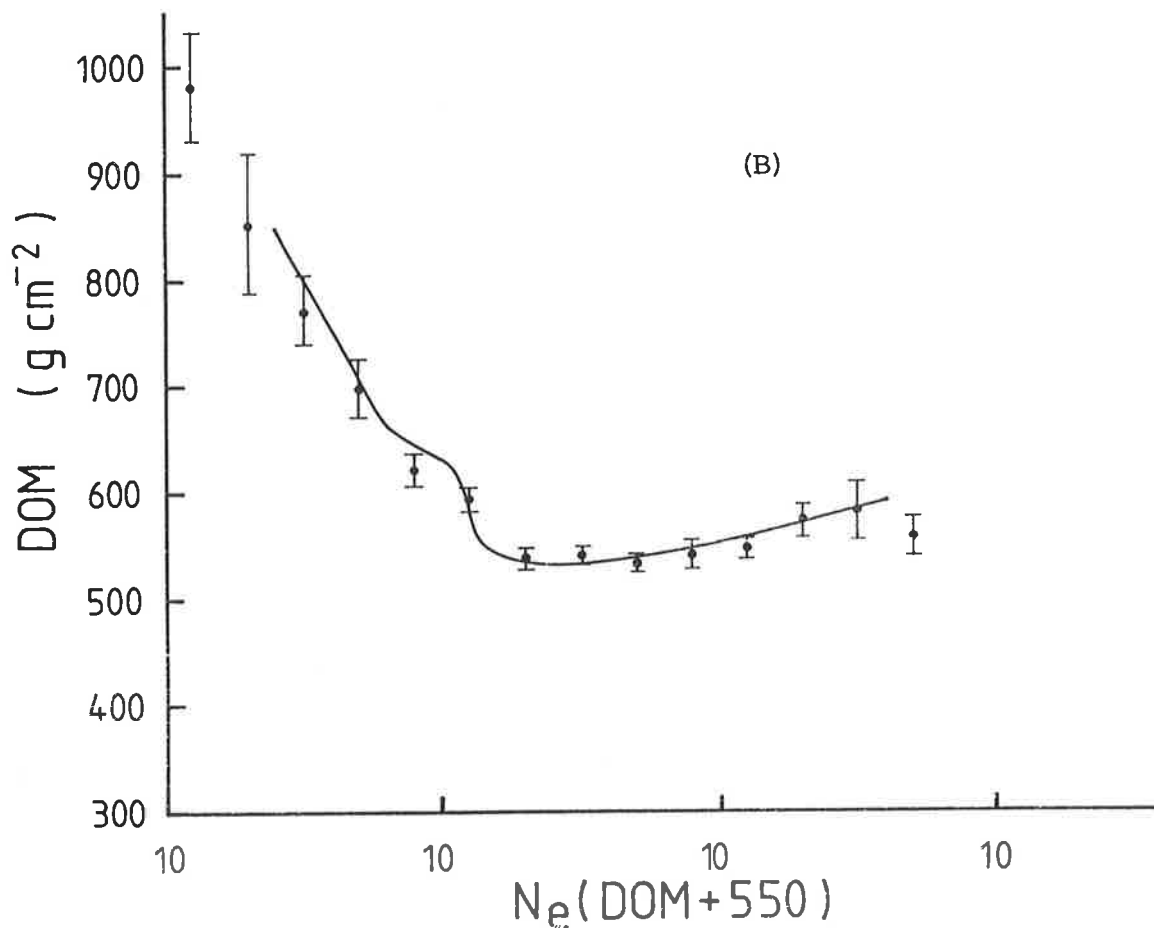
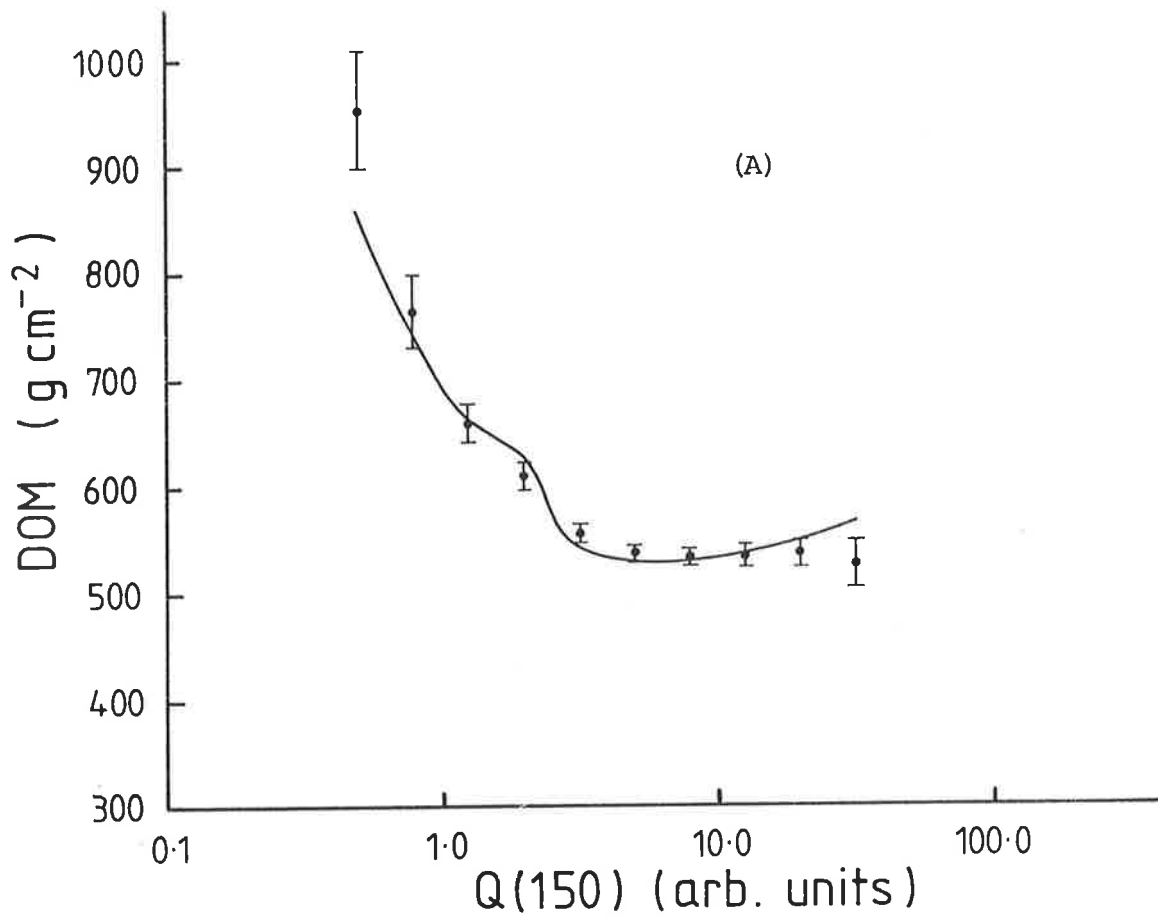


Figure 5.14: Comparison of Method One data with the distribution expected with a composition of 95% Fe and 5% p (solid line).
 A: DOM vs Q(150), comparison of mean behaviour.
 B: DOM vs $N_e(\text{DOM}+550)$, comparison of mean behaviour.

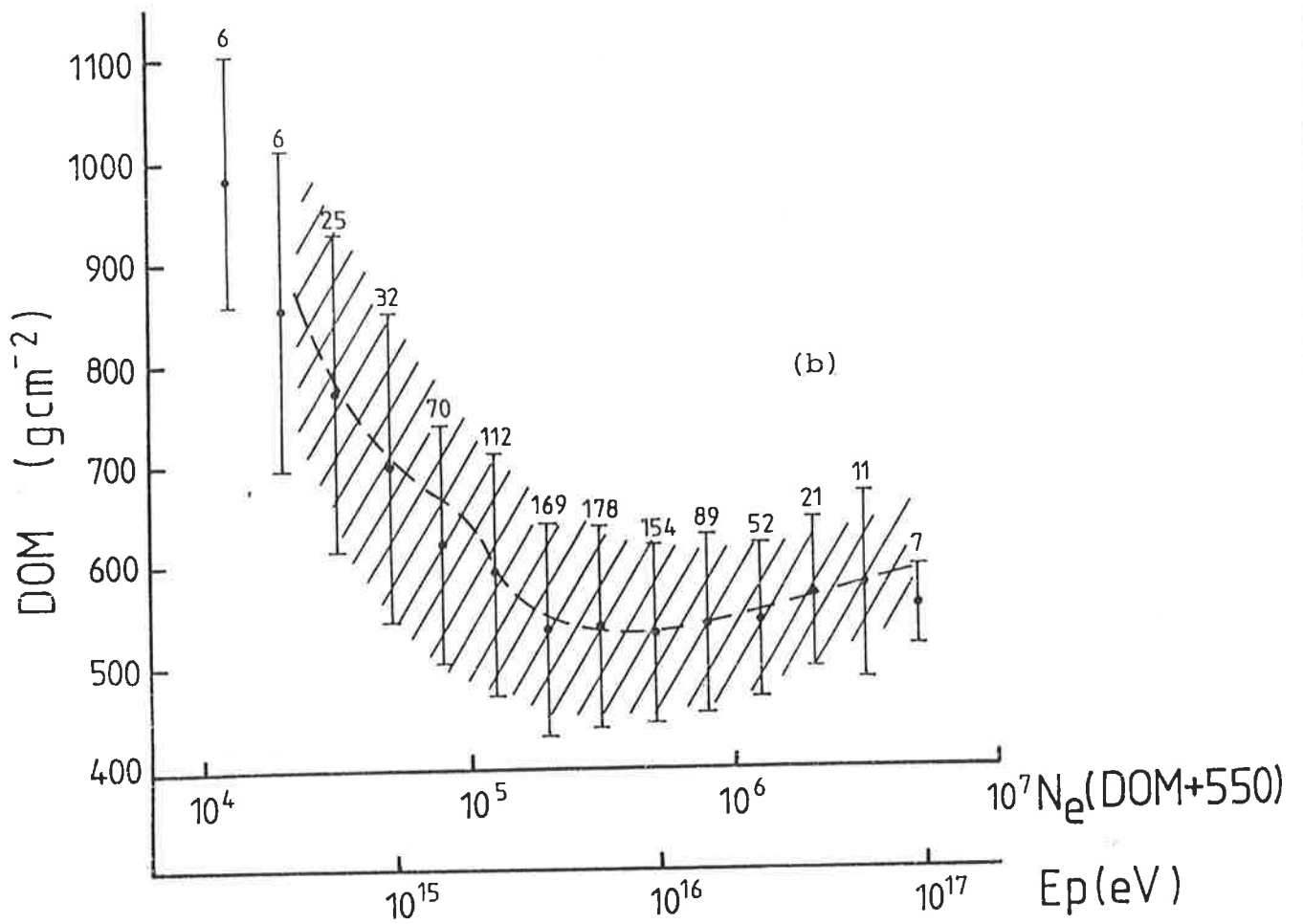
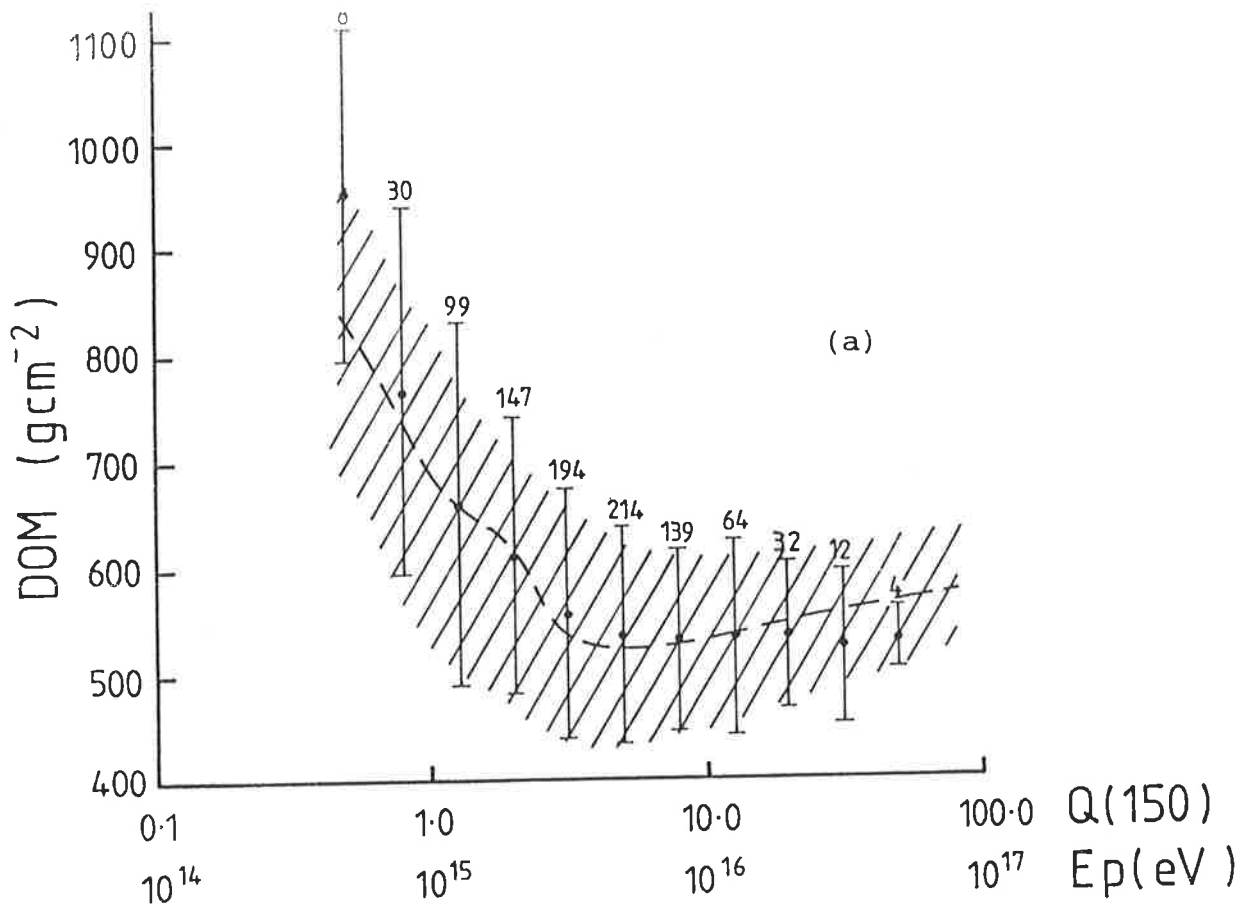


Figure 5.15(a,b): The data from figure 5.14 with standard deviations for comparison of apparent fluctuations. The simulation energy scales are shown.

the experimental energy distributions in figures 5.16 and 5.17. Again, the agreement is good.

Thus, it can be seen that the "best-fit" mixtures determined on the basis of the DOM vs shower size distributions also fit when the data is plotted against an energy estimator. It is believed that this fact should promote confidence in the validity of the simulations and the conclusions drawn from them.

It has been shown in this section that the experimental data indicate a cosmic ray composition rich in iron in the energy range studied. On the basis of the comparisons between experimental and simulated data in the energy representation, this energy range is $\sim 5 \times 10^{15} - 5 \times 10^{16}$ eV for data free of bias. Information on the composition based on data outside this range is probably less certain, although these data are consistent with the iron rich model.

As an aside, consider figure 5.18. Here are shown some simulation results expressing the fraction of all analysable sea level showers produced by iron primaries, as a function of $N_e(1000)$, for a composition of 90% iron and 10% protons. It can be seen that even though iron makes up 90% of the flux at the top of the atmosphere, it contributes a smaller fraction of showers of a given size.

5.5 Conclusion.

The reader would have noticed that Methods 1 and 2 indicate different proportions of iron and protons in the cosmic ray flux. (Method 1 predicts 95%Fe, 5%p while Method 2

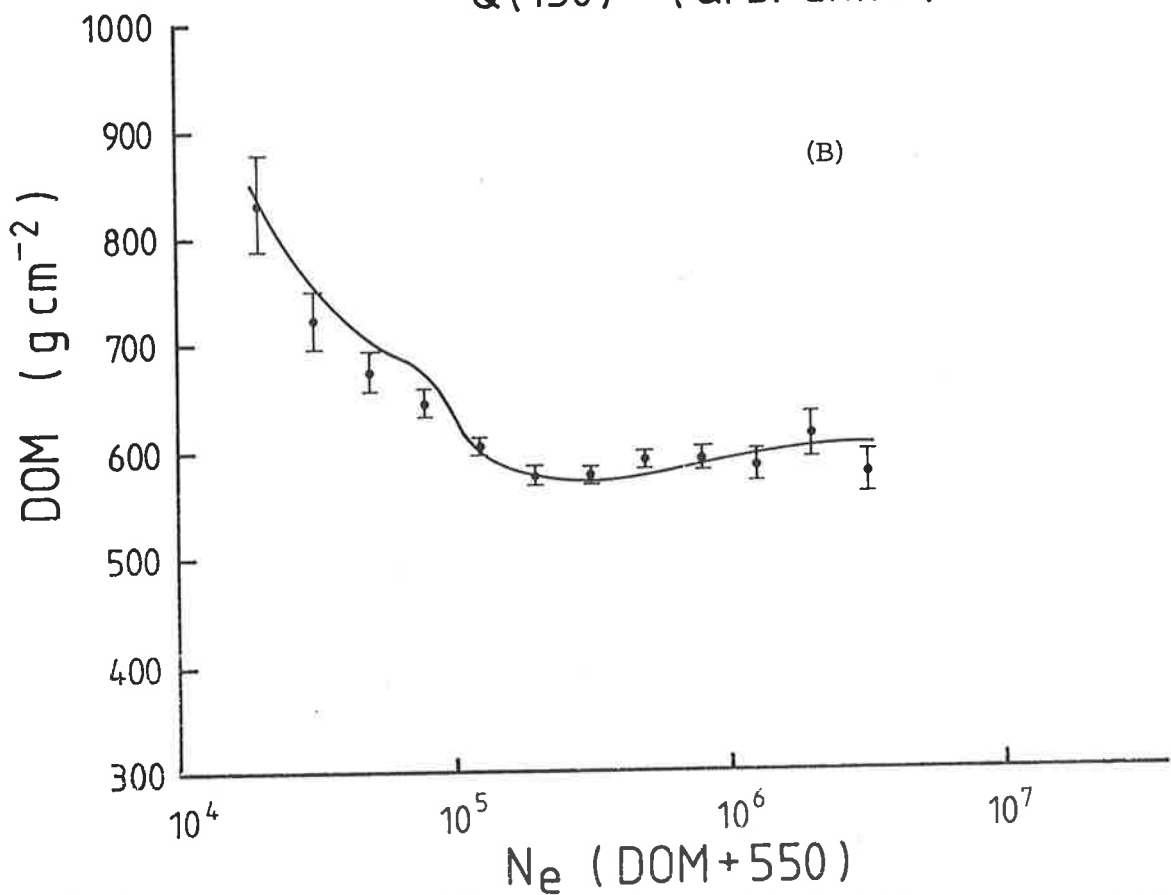
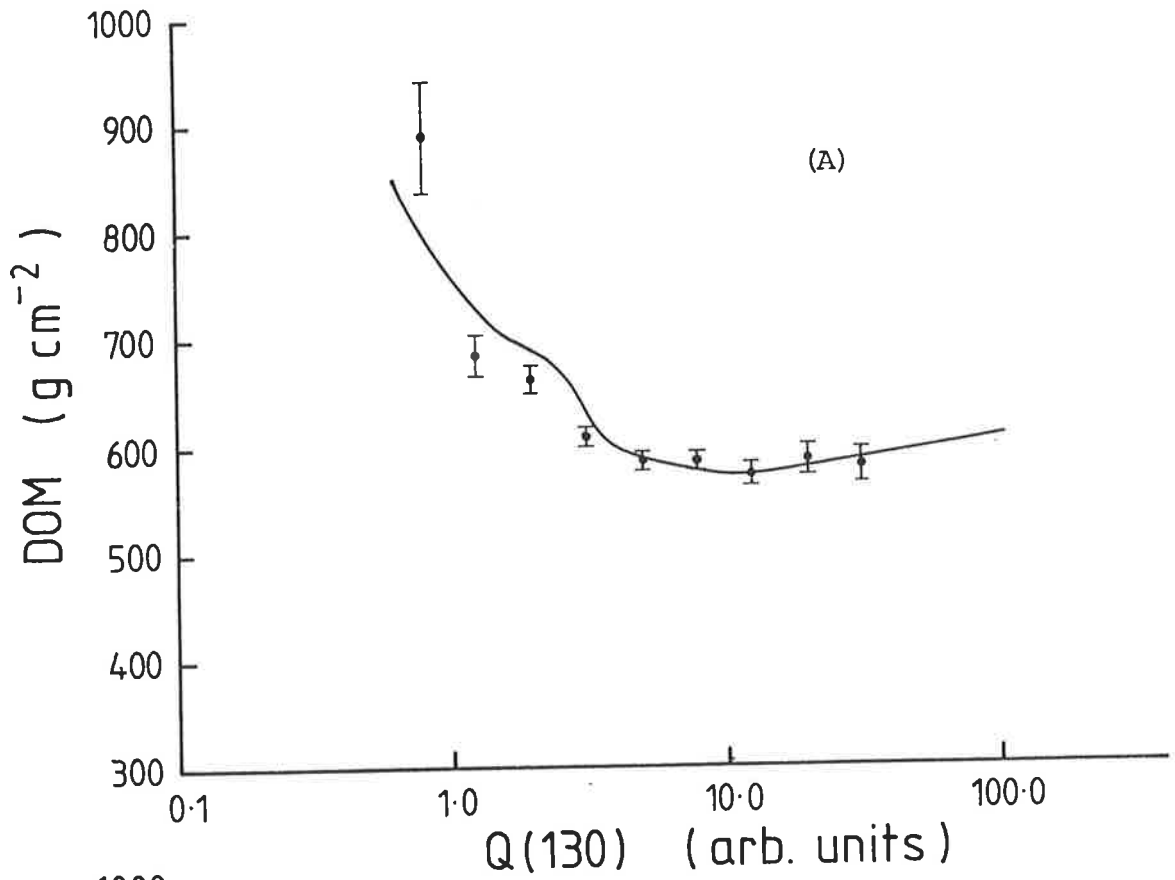


Figure 5.16: Comparison of Method Two data with the distribution expected with a composition of 85% Fe and 15% p.
 A: DOM vs Q(130), comparison of mean behaviour.
 B: DOM vs N_e(DOM+550), comparison of mean behaviour.

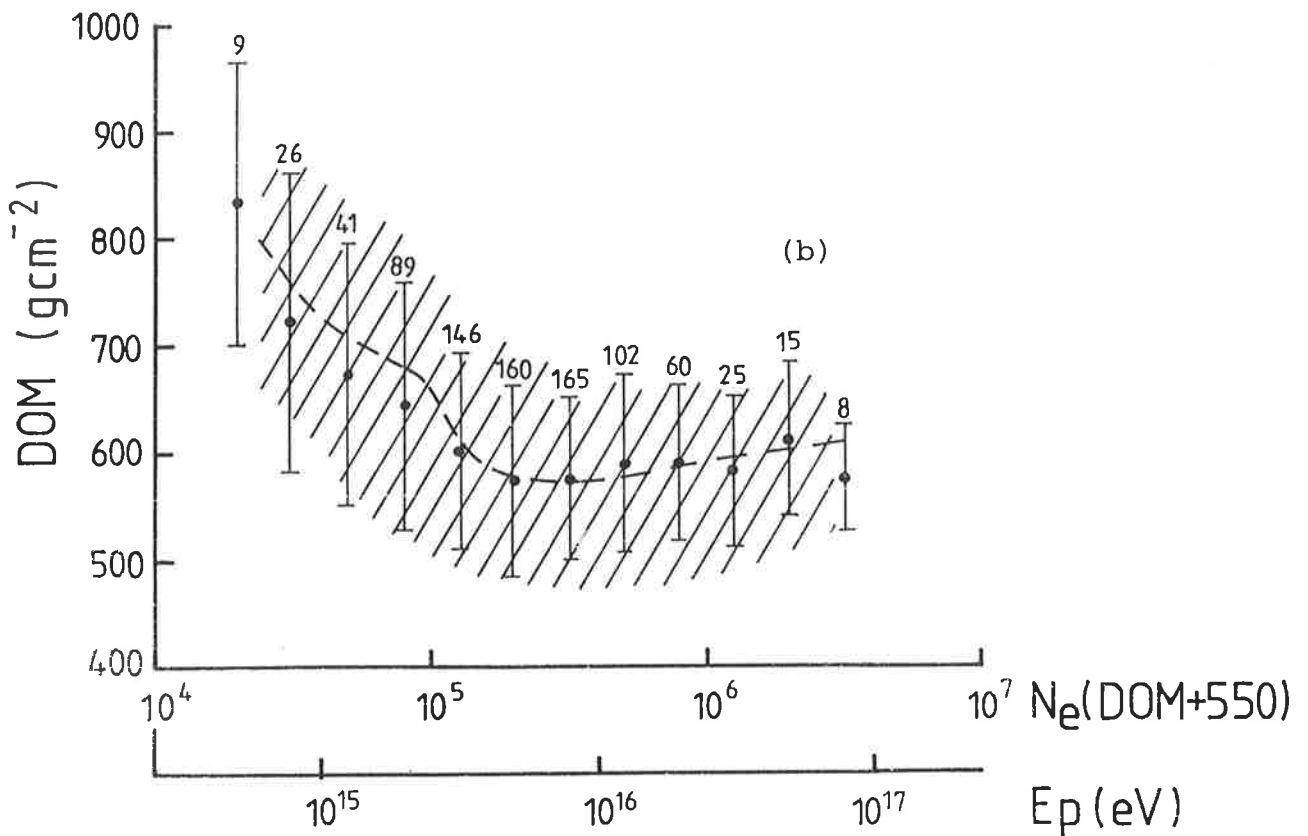
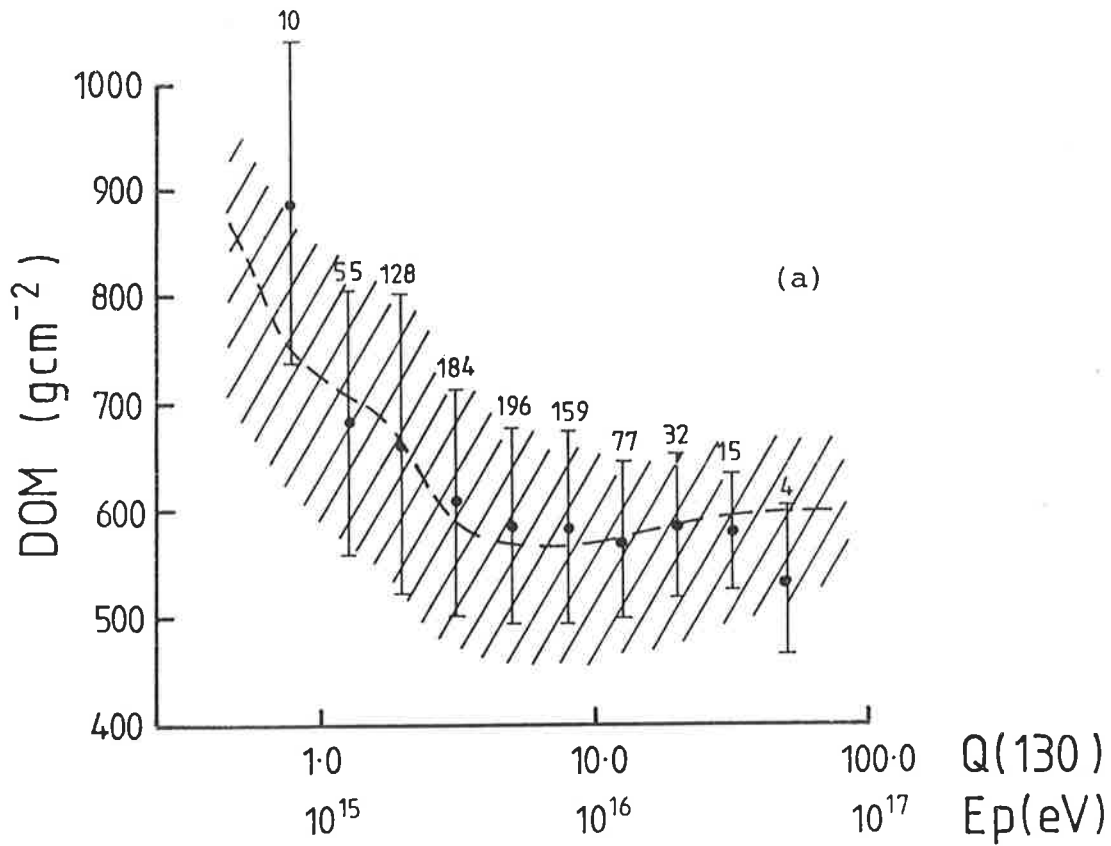


Figure 5.17(a,b): The data from figure 5.16 with standard deviations, for comparison of apparent fluctuations. The simulation energy scales are shown.

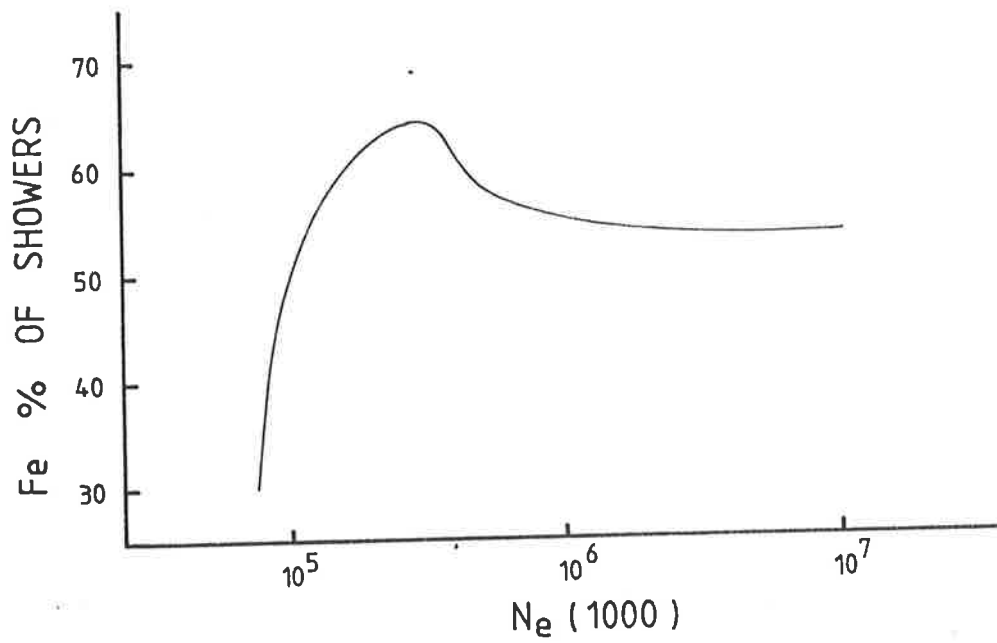


Figure 5.18: The fraction of all analysable sea level showers produced by iron primaries, as a function of $N_e(1000)$, for a composition of 90% Fe and 10% p.

predicts 85%Fe, 15%p). Both methods have been included in this section to emphasise the uncertainty involved in the assignment of DOM from the lateral distributions. However, the differences in mean DOM given by the two methods only amount to $30-40\text{gcm}^{-2}$, which is comparable with the 30gcm^{-2} subtracted from the Linsley mean DOM distribution for use in the simulations (see Eq. 5.3, 5.4). That is, the difference in the results of the two methods is comparable with uncertainties in the simulation.

Certainly, the results of Method 2 would be expected to be preferable, since it involved a very cautious treatment of the Cerenkov measurements. However the size of the standard deviations (eg fig. 5.13b) suggest that there is an inconsistency in the result; the mean behaviour suggests a composition with 85%Fe, while the standard deviations imply a composition even richer in iron. It seems probable that the true percentage of iron lies somewhere between the 85% predicted by Method 2 and the 95% predicted by Method 1.

It is generally accepted that above $\sim 10^{17}\text{eV}$, the flux of cosmic rays is dominated by protons, like the low energy composition which has been measured directly. Even though the data presented here are entirely consistent with an iron rich composition across the entire shower size range, it was decided to test for any evidence of a trend towards a proton dominated composition at large shower sizes.

To do this, data from the simulations were used. The experimental DOM vs $N_e(1000)$ distributions were compared with the following mixtures:

Method 1 Data:

- A: Composition of 95%Fe, 5%p up to 10^{16} eV, after which the percentage of iron is reduced gradually until the composition is 100%p above 4×10^{16} eV .
- B: Same as A except that the change in composition occurs between 4×10^{16} eV and 1.6×10^{17} eV.

Method 2 Data:

- A: Same as A above except that the initial composition is 85%Fe, 15%p.
- B: Same as B above except that the initial composition is 85%Fe, 15%p.

The data produced by Methods 1 and 2 are compared with the mixtures A and B in figures 5.19 and 5.20. It appears unlikely that either experimental distribution is consistent with a change in composition beginning at 10^{16} eV (figures 5.19a, 5.20a); the required change in mean DOM is too rapid, too soon. On the other hand, there is a possibility that the distributions are consistent with a change in composition beginning at 4×10^{16} eV (figures 5.19b, 5.20b). However, the uncertainties in the data at large shower sizes make it impossible to reach any firm conclusion.

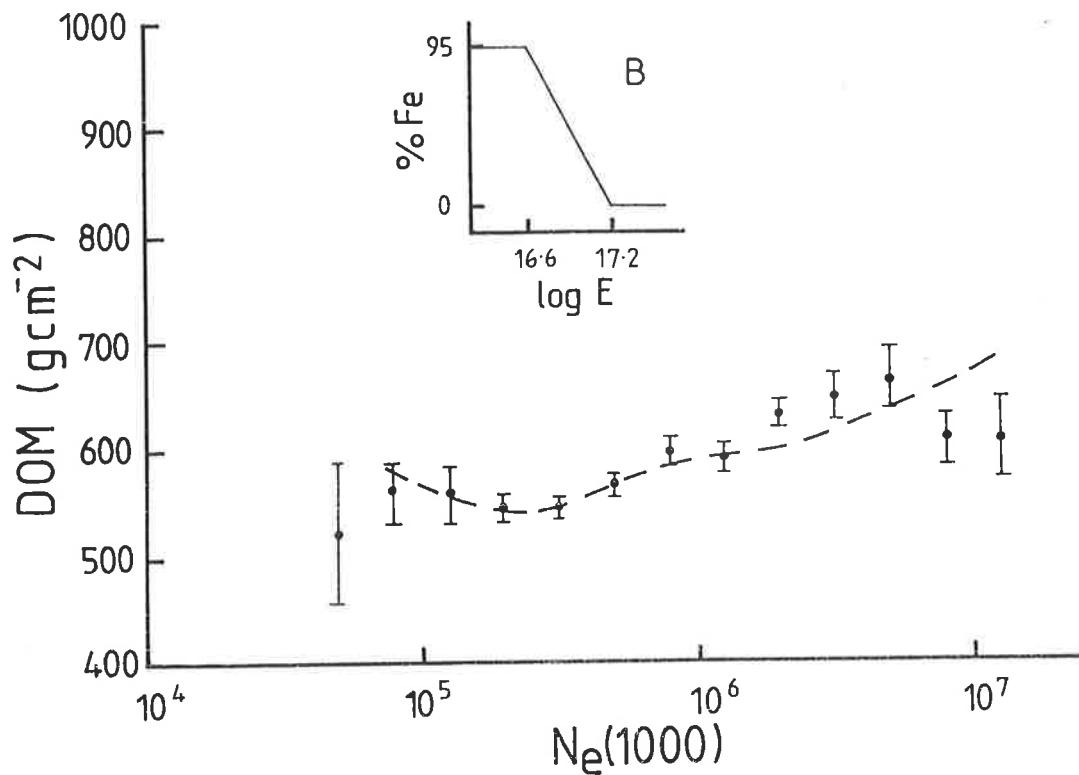
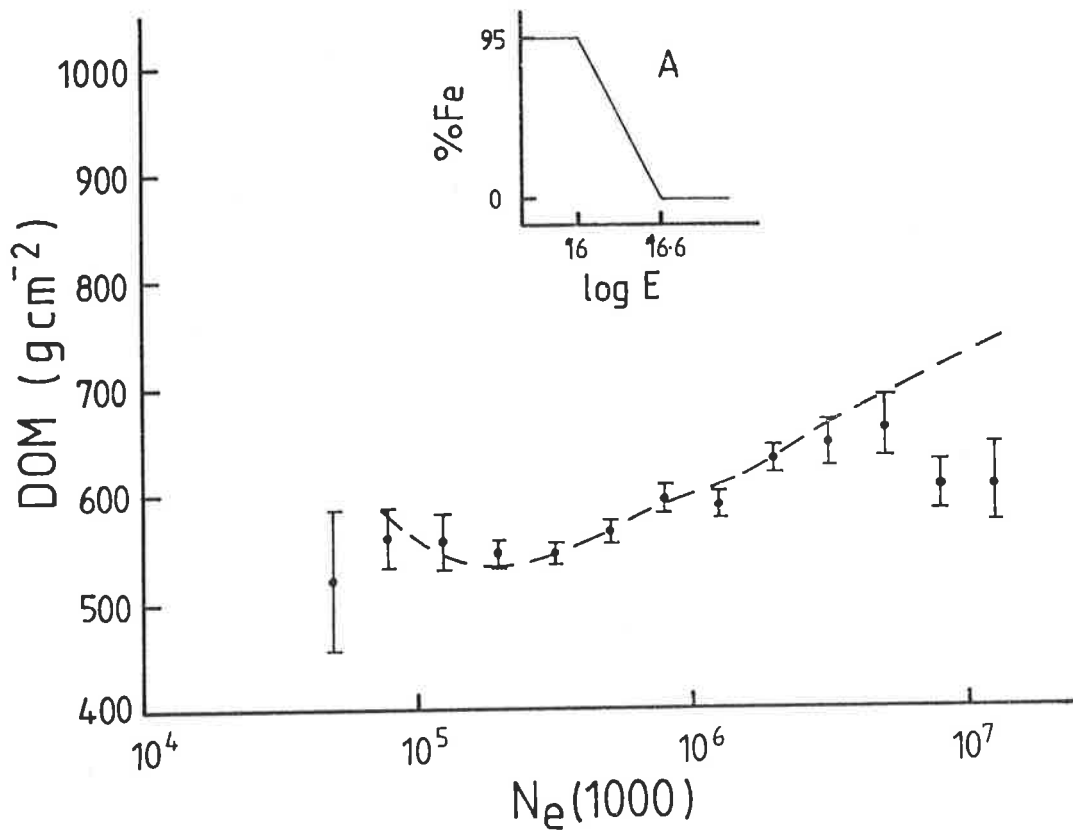


Figure 5.19: The effect of a changing composition. Method One data are compared with cases A and B described in the text (see insets).

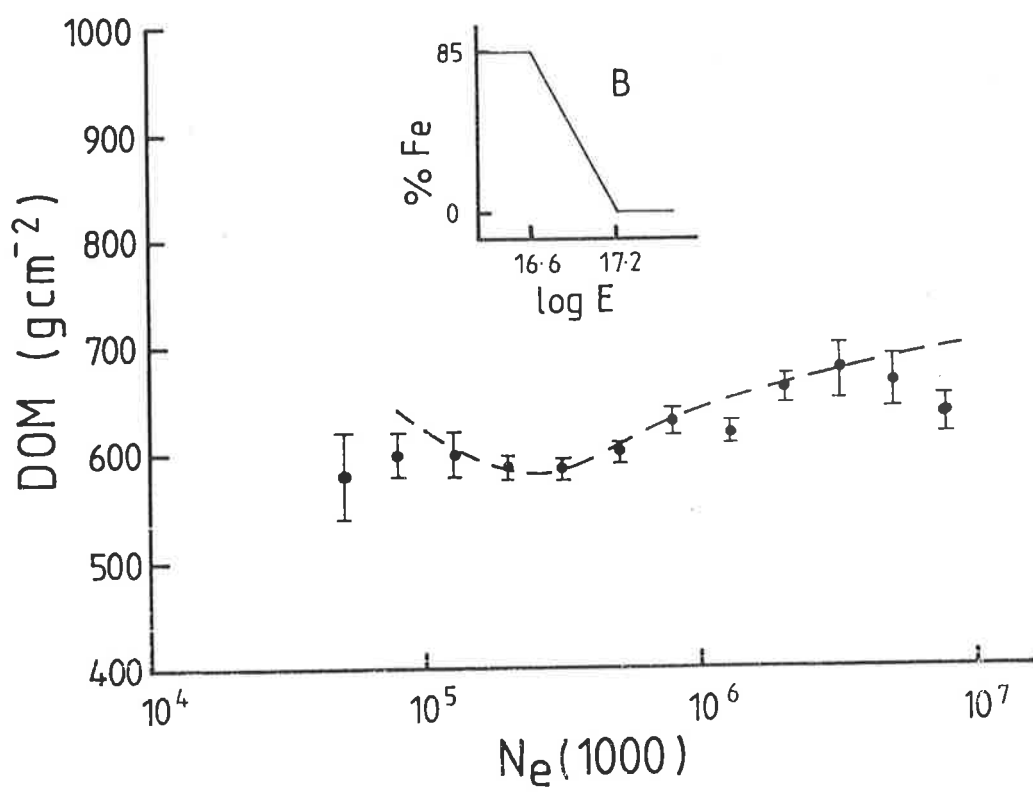
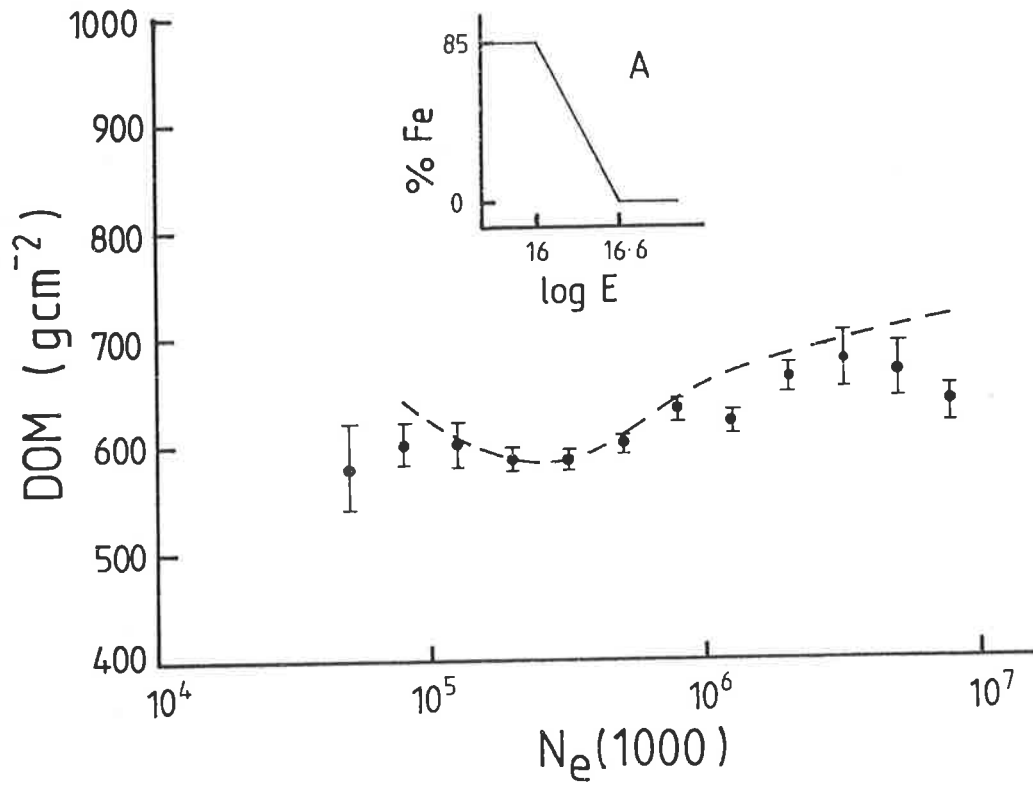


Figure 5.20: The effect of a changing composition. Method Two data are compared with cases A and B described in the text (see insets).

C H A P T E R S I X

CONCLUDING REMARKS

Figure 6.1 shows again the results from a number of experiments on the variation of depth of maximum with energy. In order to compare these with the results of the present work, we have included in the diagram our two best estimates (derived using Methods 1 and 2) of the DOM vs E variation. On the basis of the model used (Chapter 5, section 5.3) these lines correspond to compositions of 85% Fe, 15% p and 95% Fe, 5% p. It can be seen that the present data strengthen the conclusion of unusually small depths of maximum between 10^{15} eV and 3×10^{16} eV, compared with the data at low energies and above 10^{17} eV where the behaviour is consistent with a "normal" composition and "normal" particle interactions. There are, however, data in the region which support the continuation of the normal behaviour. An example of these are the points due to Alimov et al (1983) (Samarkand) who attribute the differences between their results and the Adelaide work of Thornton and Clay (1979) to particle array selection biases in the latter experiment. However, the Adelaide pulse width data presented in the figure (from Thornton 1984) have been treated in an attempt to remove any bias. And, of course, the results of the present work were arrived at via an extensive series of simulations which include the array bias.

Thus, the majority of the data in this energy region support early development. The conventional explanation for this early development (and the interpretation assumed in this work) is an increase in the proportion of heavy nuclei in the

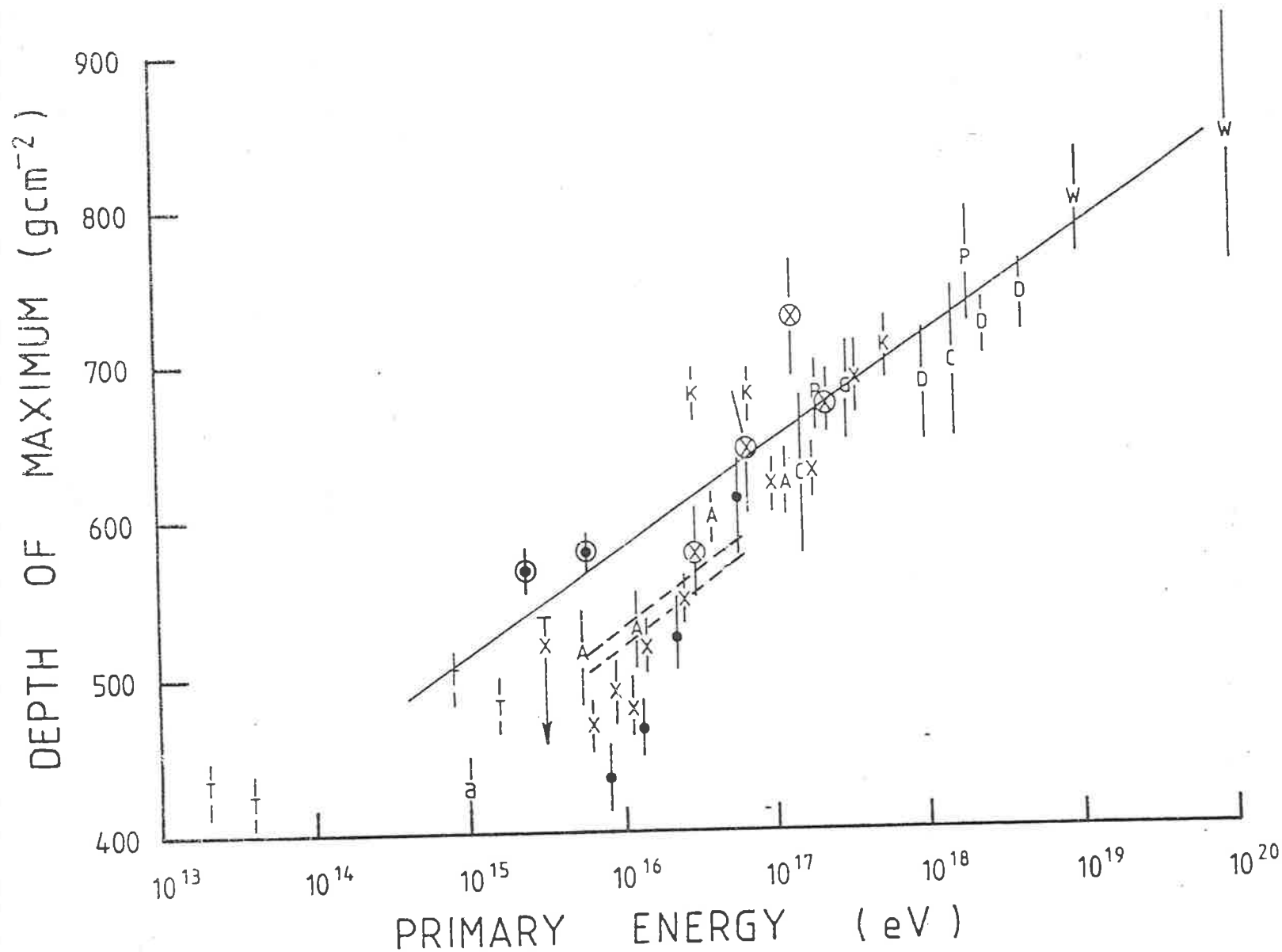


Figure 6.1: Reproduction of figure 1.5 with the addition of the dashed lines representing a composition of 95% Fe and 5% p (top line) and 85% Fe and 15% p (bottom line).

flux. This increase could be caused by a rigidity dependent confinement in either the galaxy or our local region. (see Chapter One, section 1.3.2). Such a model would require a new source of cosmic rays to become dominant above 10^{17} eV to explain the return to an apparently proton rich composition.

An alternative explanation involves departures from conventional particle interaction processes. For example, the onset of processes involving high multiplicities could cause the early development of showers. In fact, Wdowczyk and Wolfendale (1983b) have proposed that the data in the region can, to some extent, be explained with a composition not very different from the low energy one, and a fairly major scaling breakdown for which there is some evidence in the latest CERN data at energies of $\sim 2 \times 10^{14}$ eV. However, this model does not easily explain the return to "normal" behaviour above 10^{17} eV. To do this it is often necessary to resort to completely new interaction phenomena such as the possible existence of a "long flying" component of slowly attenuating hadrons, and of relatively stable massive particles (see Capdevielle et al 1982 for a summary of the evidence). Both of these phenomena could produce the necessary "late" development.

At the moment, discussion of new interaction processes is highly speculative. For this reason we have attributed the early development of showers observed in this experiment to a cosmic ray flux rich in iron in the energy range $5 \times 10^{15} - 5 \times 10^{16}$ eV.

REFERENCES

(The abbreviation Xth ICCR (or ICRC) refers to the Proceedings of the Xth International Conference on Cosmic Rays.)

- Abulova V.G., et al (1981), Proc. 17th ICRC, Paris, 2, 114.
- Acharya B.S., et al (1981), Proc. 17th ICRC, Paris, 11, 385.
- Alimov T.A., et al (1983), Proc. 18th ICRC, Bangalore, 11, 387.
- Allen H.R., (1971), Prog. Elem. Part. and Cosmic Ray Phys., 10 170.
- Allen C.W., (1955), 'Astrophysical Quantities', Second Edition, Athlone Press, London, p134.
- Alpgard, L, et al (1981), Phys. Lett. 107B, 315.
- Amaldi V., et al (1977), Phys. Lett., B66 390.
- Andam A.A., Chantler M.P., Craig M.A.B. McComb T.J.L., Orford K.J., Turver K.E., and Walley G.M., (1981), Proc. 17th ICRC, Paris, 11, 281.
- Antonov R.A., Kuzmin V.A., and Fateeva I.M., (1981), Proc. 17th ICRC, Paris, 6, 229.
- Astley, S.M., et al (1981), Proc. 17th ICRC, Paris, 2, 156.
- Astrashkevich V.B., Efimov N.N., Khristiansen G.B., and Kulikov G.V., (1983), Invited Talks, 8th European Symposium, N. Lucci et al (eds.), Bologna, p67.
- Axford W.I., (1980), I.A.U. Symposium 94, 339.
- Axford W.I., (1981), Proc. 17th ICRC, Paris, 12, 155.
- Baltrusaitis, R.M., et al (1984), Phys. Rev. Lett. 52, 1380.
- Baruch J.E.F., Brooke G., Kellerman E.W., and Walster N.D., (1979), J. Phys. G. 5, 595.
- Blandford R.D., and Ostriker J.P., (1980), Ap. J. Lett., L237, 793.
- Böhm E., Holtrup G., Bosia G., Navarra G., Saavedra O., and Cachon A., (1975), Proc. 14th ICCR, 8, 3046.
- Boley F.I., Baum J.H., Palsedge J.A., and Pereue J.H. (1961), Phys. Rev. 124, 1205.
- Bradt H., et al (1965), Proc. 9th ICRC, London, 2, 715.
- Brennan M.H., Malos J., Miller D.D., and Wallace C.S., (1958), Nature 182, 973.

- Capdevielle J.N., Gawin J., Grochalska B., and Wdowczyk J., (1982), *Nuo. Cim.*, 5C, 672.
- Cerenkov P.A. (1934), *Dokl. Akad. Nauk. S.S.S.R.*, 2, 451.
- Cerenkov P.A., (1937), *Dokl. Akad. Nauk. S.S.S.R.*, 14, 101.
- Cesarsky C.J., (1980), *Ann. Rev. Astron. Astrophys.*, 18, 289.
- Chudakov A.E., and Nesterova N.M., (1958), *Nuovo Cimento*, ser. 10, suppl. 8, 606.
- Chudakov A.E., Nesterova N.M., Zatsepin V.I., and Tuzhik E.I., (1960), *Proc. 6th ICCR, (Moscow)*, 2, 47.
- Clay R.W., Gerhardy P.R., Liebing D.F., Thornton G.J., and Patterson J.R., (1981), *Nuo. Cim.*, 4C, 668.
- Clay R.W., and Gerhardy P.R., (1982), *Aust. J. Phys.*, 35, 59.
- Colgate S.A., and Johnson H.M., (1960), *Phys. Rev. Lett.* 5, 235.
- Cowsik R., Yash Pal, Tandon S.N., and Verma R.P., (1967), *Phys. Rev.*, 158, 1238.
- Cunningham G., Lloyd-Evans J., Pollock A.M.T., Reid R.J.O., and Watson A.A., (1980), *Ap. J.*, 236, L71.
- Dwyer R.D., and Meyer P. (1981), *Proc. 17th ICRC, Paris*, 9, 222.
- Dyakonov M.N., et al (1973), *Proc. 13th ICCR (Denver)*, 4, 2389.
- Dyakonov M.N. et al (1975), *Iz. Akad. Nauk. S.S.S.R.*, 39, 1249.
- Efimov N.N., and Sokurov V.F., (1979), *Proc. 16th ICRC, Kyoto*, 8, 52.
- Egorov T.A. et al (1971a), *Proc. 12th ICCR (Hobart)*, 6 2164, (1971b), *Proc. 12th ICCR (Hobart)*, 6, 2059.
- Eichler D., and Vestrand W.T., (1984), *Nature*, 307, 613.
- Elbert J.W., (1978), *Proc. Dum and Summer Workshop, La Jolla*, A. Roberts (ed.), 2, 101.
- Elbert J.W., Gaisser T.K., and Stanev T. (1981), *Proc. 17th ICRC, Paris*, 7, 42.
- Ellsworth R.W., and Yodh G.B., (1981), *Proc. 17th ICRC, Paris*. 11, 390.
- Ellsworth R.W., Gaisser T.K., Stanev T., and Yodh G.B., (1982), *Phys. Rev. D.*, 26, 336.
- Fermi E., (1949), *Phys. Rev.*, 75, 1169.
- Fermi E., (1951), *Phys. Rev.*, 81, 683.

- Feynman R.P., (1969), Phys. Rev. Lett., 23, 1415.
- Fomin Yu. A. and Khristiansen G.B., (1972), Sov. J. Nuc. Phys., 14, 360.
- Frank I.M., and Tamm, I., (1937), Dokl. Akad. Nauk. S.S.S.R., 14, 109.
- Gaisser T.K., Protheroe R.J., Turver K.E., and McComb T.J.L., (1978).
- Gaisser T.K., McComb T.J.L., and Turver K.E., (1979), Proc. 16th ICRC, Kyoto, 9, 275.
- Gaisser T.K., and Yodh G.B., (1980), Ann. Rev. Nuc. Part. Sci., 30, 475.
- Gaisser T.K., Protheroe R.J., and Stanev T., (1983), Proc. 18th ICRC, Bangalore, 5, 174.
- Galbraith W., and Jelley J.V., (1953), Nature, 171, 350.
- Garcia - Munoz M., Simpson J.A., and Wefel J.P., (1981), Proc 17th ICRC, Paris, 2, 72.
- Gardner F.F., et al (1969), Aust. J. Phys., 22, 813.
- Gerhardy, P.R., (1983), Ph.D. Thesis, University of Adelaide.
- Gibson, A.I., McComb T.J.L., and Turver K.E., (1981), Proc. 17th ICRC, Paris, 6, 16.
- Goldanski G., and Zhdanov, G.B., (1954), Zh. Eksp. Teor. Fiz. 26, 405.
- Goodman J.A., Ellsworth R.W., Ito A.S., MacFall J.R., Siohan F., Streitmatter R.E., Tonwar S.C., Viswanath P.R., and Yodh G.B., (1982), Phys. Rev. D., 26, 1043.
- Gregory J.C., et al (1981), Proc. 17th ICRC, Paris, 9, 154.
- Greisen K.G., (1958), Prog. Cosmic Ray Phys., 3, 1.
- Greisen K., (1966), Phys. Rev. Lett., 16, 748.
- Grieder P.K.F., (1984), Nuo. Cim., 84A, 285.
- Grigorov N.L., Rapoport I.D., Savenko I.A., Nesterov V.E., and Prokhim V.L., (1971), Proc. 12th ICRC, Hobart, 5, 1746.
- Grishna N.V., et al (1981), Proc. 17th ICRC, Paris, 2, 3.
- Gunn J.E., and Ostricker J.P. (1969), Phys. Rev. Lett., 22, 728.
- Hammond R.T., Orford K.J., Shearer J.A.L., Turver K.E., Waddoup W., Welby D.W., (1977), Proc. 15th ICRC, Plovdiv, 8, 281.

- Hammond R.T., Orford K.J., Protheroe R.J., Shearer J.A.L.,
Turver K.E., Waddoup W.D., and Wellby D.W., (1978), *Nuo.
Cim.*, 1C, 315.
- Heiles, C., (1976), *Ann. Rev. Astron. Astrophys.*, 14, 1.
- Heiles C., (1979), *Ap. J.*, 229, 533.
- Hartman D.H., Fan C.Y., Googh P.G., Turver K.E., and Weekes
T.C., (1977), *Proc. 15th ICRC, Plovdiv*, 8, 233.
- Hillas A.M., (1979), *Proc. 16th ICRC, Kyoto*, 8, 7.
- Hillas A.M., (1981), *Proc. 17th ICRC, Paris*, 13, 69.
- Hillas A.M., (1982), in "Composition and Origin of Cosmic Rays"
M.M. Shapiro (ed.), D. Reidel Publishing Co. Dordrecht, pp
125-148.
- Hillas A.M., (1982a), *J. Phys. G.* 8, 1461.
- Hillas A.M., (1982b), *J. Phys. G.* 8, 1475.
- Hillas A.M., (1983), *Proc. Cosmic Ray Workshop, Univ. Utah, T.
Geisser (ed.)*, p16.
- Hillas A.M., (1984), *Nature*, 312, 50.
- Horton L., McCusker C.B.A., Peak L.S., Ulrichs J., and Winn
M.M., (1983), *Proc. 18th ICRC, Bangalore*, 2, 128.
- Inoue N., Sugawa S., Tamura T., Enoki T., Mujazaki Y., Kakimoto
F., Suga K., and Nishi K., (1981), *Proc. 17th ICCR*, 11,
270.
- Israel M.H., (1981), *Proc. 17th ICRC, Paris*, 12, 53.
- Jelley J.V., (1958), *Nuo. Cim.*, 8, Suppl. 578.
- Jelley J.V., (1967), *Prog. in Elem. Part. and Cosmic Ray Phys.*,
9, 41.
- Jelley J.V., and Galbraith W., (1955), *J. Atmos. Terr. Phys.*,
6, 250.
- Kakimoto F. et al (1983), *J. Phys. G.*, 9, 339.
- Kalmus P. (1982), *Workshop on Very High Energy Cosmic Ray
Interactions, Univ. of Pennsylvania, (M.L. Cherry et al
eds.)*, 1.
- Kalmykov N.N., et al (1977), *Proc. 15th ICCR*, 8, 244.
- Kalmykov N.N., et al (1979), *Proc. 16th ICRC, Kyoto*, 9, 73.
- Kalmykov N.N. and Nishimura J., (1958), *Prog. Theor. Phys., Suppl.*

- Kiraly P., and Kota J., (1979), *Revista del Nuovo Cimento*, 2, 1.
- Koch-Miramond L., (1981), *Proc. 17th ICRC, Paris*, 12, 31.
- Krieger, A.S. and Bradt, H.V., (1968), *Can. J. Phys.*, 46, 587, (1969), *Phys. Rev.* 85, 1629.
- Kuhlmann J.D., Clay R.W., Crouch P.C., Gerhardy P.R., Gregory A.G., Patterson J.R., Prescott J.R., and Thornton G.J., (1977), *Proc. 15th ICRC, Plovdiv*, 8, 239.
- Kuhlman J.D., and Clay R.W., (1981), *Proc. 17th ICRC, Paris*, EA2-9.
- Lagage P.O., and Cesarsky C.J., (1983), *Astron. Astrophys.*, 125, 249.
- Landau L.D., (1953), *Izv. Akad. Nauk S.S.S.R.*, 17, 51.
- La Pointe M., et al (1968), *Can. J. Phys.*, 46, S68.
- Liebing D.F., Clay R.W., Patterson J.R., and Gregory A.G., (1983), *Proc. 18th Bangalore*, 6, 214.
- Linsley J., (1981), *Proc 17th ICRC, Paris*, 11, 246.
- Linsley J., (1982), *Proc. Paris Workshop on Cascade Simulations*, Linsley J., and Hillas A.M., (eds.), p23.
- Linsley J., (1983), *Proc. 18th ICRC, Bangalore*, 12, 135.
- Linsley J., and Watson A.A., (1981), *Phys. Rev. Lett.*, 46, 459.
- Lloyd-Evans J. and Watson A.A., (1982), *Review paper presented at 8th European Cosmic Ray Symposium*, Iucci et al (eds), Bologna, p81.
- Lloyd-Evans J., Coy R.N., Lambert A., Lapikens J., Patel M., Reid R.J.O., and Watson A.A., (1983), *Nature*, 305, 784.
- McCubbin N.A., (1981), *Rep. Prog. Phys.*, 44, 1027.
- Mason G.W., et al (1975), *Proc. 14th ICRC, Munich*, 8, 2943.
- Mewaldt R.A., (1981), *Proc. 17th ICRC, Paris*, 13, 49.
- Müller D., (1982), *Workshop on Very High Energy Cosmic Ray Interactions*, University of Pennsylvania, M.L., Cherry et al (eds.), p448.
- Nesterova N.M., and Dubovy A.G., (1979), *Proc. 16th ICRC, Kyoto*, 8, 345.
- Nikolsky S.I., et al (1981), *Proc. 17th ICRC, Paris, 1981*, 2, 129.
- Orford K.J. and Turver K.E., (1976), *Nature*, 26, 727.

- Ormes J.F., and Protheroe R.J., (1983), *Ap. J.*, 272, 756.
- Patterson J.R., and Hillas A.M., (1983a), *J. Phys. G.*, 9, 323.
- Patterson J.R., and Hillas A.M., (1983b), *J. Phys. G.*, 9, 1433.
- Peters B., (1961), *Il Nuovo Cimento*, 22, 800.
- Prescott J.R., Clay R.W., Corani C.L., Dawson B.R., Gregory A.G., and Patterson J.R., (1983), *Proc. 18th ICRC, Bangalore*, 1, 135.
- Protheroe R.J., (1977), Ph.D. Thesis, University of Durham.
- Protheroe R.J., (1984), *J. Phys. G.*, 10, L99.
- Protheroe R.J., and Turver K.E., (1979), *Nuo. Cim.*, 51A, 277.
- Protheroe R.J., Clay R.W., and Gerhardy P.R., (1984), *Ap. J.*, 280, L47.
- Protheroe R.J., and Patterson J.R., (1984), *J. Phys. G.*, 10, 841.
- Protheroe R.J., and Clay R.W., (1985), *Nature*, 315, 205.
- Roberg J., and Nordheim L.W., (1949), *Phys. Rev.*, 75, 444.
- Rossi B., and Greisen K.G., (1941), *Rev. Mod. Phys.*, 13, 240.
- Samorski M., and Stamm W., (1983), *Ap. J.*, 268, L17.
- Simon M., Spiegelhauer H., Schmidt W.K.H., Siohan F., Ormers J.R., Balasubrahmanyam V.K., and Arens J.F., (1980), *Ap. J.*, 239, 712.
- Sitte K., (1962), *Nuovo Cimento, ser. 10*, 25, 86.
- Sood R., (1983), *Nature*, 301, 44.
- Stephens S.A., (1981), *Proc. 17th ICRC, Paris*, 13, 89.
- Streitmatter R.E., Balasubrahmanyam V.K., Ormes J.F., and Protheroe R.J., (1983), *Proc. 18th ICRC, Bangalore*, 2, 183.
- Thornton G.J., (1984), Ph.D. Thesis, University of Adelaide.
- Thornton G.J., and Clay R.W., (1979), *Phys. Rev. Lett.*, 43, 1622, (and Erratum, 45, 1463).
- Thornton G.J., and Clay R.W., (1981), *Phys. Rev. D.*, 23, 2090.
- Tornabene H. (1979), *Proc. 16th ICRC, Kyoto*, 9, 99.
- Walker R., and Watson A.A., (1981), *J. Phys. G.*, 7, 1297.

- Watson, A.A., (1981), Proc. 16th Recontre de Moriond
Astrophysic Meeting, "Cosmology and Particles", J. Audouze
et al (eds.)
- Wdowczyk J., and Wolfendale A.W., (1983a), Nature, 305, 609.
- Wdowczyk J., and Wolfendale A.W., (1983b), Nature, 306, 347.
- Webber, W.R., (1982), in "Composition and Origin of Cosmic
Rays", M.M. Shapiro (ed.), D. Reidel Publishing Co.,
Dordrecht pp25-46.
- Westfall G.D., Wilson L.W., Lindstrom P.J., Crawford H.J.,
Greiner D.E., and Heckman H.H., (1979), Phys. Rev. C., 19,
1309.
- Wiedenbeck M.E., (1982), in "Composition and Origin of Cosmic
Rays, M.M. Shapiro (ed.), D. Reidel Publishing Co.,
Dordrecht, pp65-82.
- Wiedenbeck M.E., and Greiner D.E., (1981), Proc. 17th ICRC,
Paris, 2, 76.
- Yodh, G.B., Yash Pal and Trefil J.S., (1972), Phys. Rev. Lett.,
28, 1005.
- Yodh G.B., Tonwar S.C., Goodman J.A., and Ellsworth R.W.,
(1982), Proc. "Workshop on VHE Cosmic Ray Interactions",
Cherry, M.L., et al (eds.), University of Pennsylvania.
- Yodh G.B., Goodman J.A., Tonwar S.C., and Ellsworth R.W.,
(1984), Phys. Rev. D., 29, 892.
- Zatsepin, V.I., and Chudakov A.E., (1962), Sov. Phys. JETP, 15,
1126.